The Interaction of Coherent Acoustic Phonons with Electrons in Semiconductor Superlattices

Caroline Louise Poyser, MPhys

Thesis submitted to the University of Nottingham,

for the degree of Doctor of Philosophy,

December 2015.

Abstract

This thesis presents a study of the electron-phonon interaction in an *n*-doped weakly coupled semiconductor superlattice (SL). Two experiments were performed which studied different aspects of this interaction. Firstly, a coherent phonon optics chip was designed. This was used in an experiment where a phonon beam was passed through the SL while an electrical bias was applied to it. The experiment provided a sensitive measurement of the effects caused by bias in the SL on the phonon beam. Secondly, a train of strain pulses was passed through the SL and the charge transferred in the device due to the strain was investigated.

A coherent phonon optics chip was formed using a semiconductor superlattice as a transducer structure and a *p-i-n* photodiode as a coherent phonon detector on the opposite side of the substrate. The doped weakly coupled superlattice structure, which is the main subject of investigation in this thesis was grown between the transducer and detector structures. Optical access mesas were processed on both sides of the substrate to allow the application of bias to both the doped superlattice and the *p-i-n* structures. A photocurrent *pump-probe* experiment was then performed using a femtosecond laser to excite the transducer structure and activate the detection mechanism.

The application of bias to the weakly coupled SL was found to cause a small attenuation to the 378 GHz phonon beam passing through it. An investigation of the possible causes of this attenuation ruled out several trivial explanations, suggesting that it was caused by the interaction between electrons and phonons in the structure. The active control of phonon amplitude by electrical means has not previously been demonstrated and may offer exciting new prospectives

for phonon devices and experiments. The coherent phonon optics technique was shown to be very sensitive and it will be a useful technique to increase our understanding of future acousto-electric devices.

The electrical signal that acoustic excitation caused in the SL device was investigated using a pulse shaping technique in combination with an amplified femtosecond laser. A Fabry-Pérot cavity was used in the laser path to create a train of equally spaced laser pulses with an adjustable pulse spacing. Focussing these pulses on an aluminium film transducer creates a train of equally spaced acoustic pulses simulating a monochromatic acoustic wave packet. The SL was processed and electrically contacted so that the charge transferred through it due to the acoustic pulse train could be monitored using a 12.5 GHz-bandwidth digital oscilloscope.

The variation in charge transfer seen as a function of the DC bias applied to the device and as a function of the total energy of the acoustic pulse train was investigated. The behaviour was compared to a theoretical model developed in the style of previous theories of electrical conversion in SLs excited by electromagnetic waves. The dependencies of the charge transfer on the bias and energy of the pulse train were well reproduced in the theory. The theory predicted that magnitude of the signal in the superlattice was independent of the frequency of the acoustic pulse train. This was verified by measuring the frequency dependence of the signal seen for a variety of transducer films. The frequency dependences seen were well explained through simulations presuming the device response was independent of train frequency. This confirms the predictions of the theory.

Both the experiments detailed in this thesis have helped increase our understanding of the nature of electron-phonon interactions in superlattices. It is hoped that a fuller understanding of these interactions may be instrumental in the creation of exciting new acousto-electrical devices.

Publications and Presentations

C. L. Poyser, A. V. Akimov, R. P. Campion and A. J. Kent. Coherent phonon optics in a chip with an electrically controlled active device. *Scientific Reports*, 5:8279, February 2015.

C. L. Poyser, A. V. Akimov, A. G. Balanov, R. P. Campion and A. J. Kent. A weakly coupled semiconductor superlattice as a harmonic hypersonic-electrical transducer. *New Journal of Physics - submitted.*

The work detailed in chapter 4 was presented at the following conferences and meetings:

E-MRS 2014 Spring meeting, *May 2014*, Lille, France.

Optics and Ultrasound II, Meeting of the IOP Optical and Physical acoustics groups, *May 2014*, Nottingham, England.

Optics and Ultrasound I, Meeting of the IOP Optical and Physical acoustics groups, *May 2013*, Nottingham, England.

Acknowledgements

There are many people I would like to thank for their help during my PhD. My supervisor Tony Kent for his guidance and optimism throughout my PhD. Andrey Akimov for his encouragement and patience in the lab.

Richard Campion for the hard work he put into the challenging structures we asked him to grow. Dave Taylor and Jas Chauhan for their advice and assistance with my various processing dilemmas. Chris Pallender and Dave Holt for cheerfully arranging helium, sometimes at short notice.

My friends in the tea room for making times in physics enjoyable. All the students from the THz acoustics group I have met, past and present for your help and sympathy, especially Sarah Heywood.

My family for their support. Most of all Lozz, for your unceasing support and confidence in my ability, and for understanding all those times I've been late home.

Contents

List of Figures

List of Tables

Chapter 1

Introduction

In the same way that light may be treated as both an electromagnetic wave and a particle, so too can sound be treated as both an acoustic wave and a particle. In the case of light the particle is referred to as a photon while its acoustic analogue is known as the phonon. The phonon is responsible for the transmission of heat and sound and, as such, considerable effort has been dedicated to the control of phonons as a means to control thermal losses and create effects such as acoustic cloaking [1].

The focus of this work is phonons in the sub-THz range, here defined as frequencies between 0.01 THz to 0.5 THz. Acoustic phonons in this frequency range have wavelengths of nanometers. This makes them useful tools for the study of thin films [2–4], multi-layered structures [5, 6] and the imaging of buried nanostructures, [7–9]. Another interesting area of application is the control and manipulations of electrons in nanostructures. Here the nanometer wavelength of the high frequency phonons, means they provide modulations of device properties on the scale of the electron confinement lengths, while their high frequencies opens the possibility of coupling to high frequency electronics.

This chapter will provide a background in previous work with sub-THz phonons and their interaction with electrons. The work detailed in this thesis particularly focusses on the interaction of electrons and phonons in a doped semiconductor superlattice, so a particular focus of this chapter will be to review earlier work with semiconductor superlattices. Finally this chapter will explain the motivation for the work described in this thesis and give an outline of the content of later chapters.

1.1 Picosecond Acoustics

Picosecond acoustics was developed as a technique in the 1980's [3] and has seen extensive use since then. The technique represents an extension of the traditional ultrasonic techniques to giga and even terahertz. Since the 1980's there has been extensive application of this technique to a variety of samples, a brief overview of some of these will be given here.

The absorption of light from a pico or femtosecond pulsed laser in an opaque material leads to the rapid heating of the material and its emission of a bipolar strain pulse consisting of high frequency acoustic waves, further details of the mechanism behind this emission will be given in subsequent chapters [10]. In the picosecond ultrasonic experiment, a second pulse of laser light is then used to detect the interaction of this acoustic pulse with a material. The detection occurs through changes of the optical reflectivity caused by presence of the acoustic wave at the sample surface [3]. The alteration of the timing between the two laser pulses enables the measurement of high frequency phenomena without the need for fast electronics. This type of experiment is referred to as a *pump-probe* experiment and will be further discussed in subsequent chapters. In initial experiments, the technique was used to measure the attenuation and velocity in different materials by measuring the magnitude and spacing between successive echoes of acoustic pulses within a thin film of the material [3].

An extension of the technique was also developed for use in the case of samples which are transparent to probe light [11]: further information may be obtained in the *pump-probe* configuration by an interaction of the probe light with the propagating strain pulse known as Brillouin oscillations. These are oscillations seen in the probe beam due to interference of light reflecting off the strain pulse with light reflected off the sample interfaces. As the strain pulse propagates through the sample the phase difference between the two reflected beams changes resulting in oscillations of the intensity of the reflection seen. This can be used to give information about the elastic, optical and mechanical properties of a sample [12].

A biomedical application of picosecond acoustics is in the study of biological cells [13]. In these experiments a cell which is of interest is placed on a metal plate. A pump laser beam is directed at this plate through the cell generating a strain wave, at the interface between the cell and the metal. This wave is able to propagate into the cell due to its adhesion on the plate. A probe beam is then directed at the cell, and Brillouin oscillations are recorded. This was further developed by the creation of a special opto-acoustic transducer for biological purposes which uses a thin metal film on a transparent substrate. This allows the excitation of the cell-metal interface from underside of the structure without the pump pulse travelling through the cell. Focussing the probe beam on the transducer from the cell side in this configuration enables a mapping of the cell acoustic impedance and the interfacial stiffness of the film-cell interface. [13].

A further recent extension of picosecond acoustics has been the creation of a scanning acoustic microscope [14]. The microscope relies on a *pump-probe* technique to generate and detect an acoustic pulse. The instrument includes a structure designed to generate the acoustic pulses when excited by the laser and then direct these pulses to the sample to be studied. The time it takes these pulses to return to the microscope structure can be used to measure their distance from the source. The signal to noise of the instrument is improved by the inclusion of an optical cavity. The optical cavity improves

the generation of the acoustic pulse by increasing the absorption of the light. When the acoustic pulses returns to the cavity the change in reflectivity seen is increased by the change in the cavity spacing leading to an improved detection. An acoustic lens was designed to allow focussing of the pulses to the sample surface and the structure was mounted on a translation stage to allow scanning. To minimise attenuation of the strain pulse before it reaches the sample water was used as a coupling medium. The experiments presented in [14] represent a proof of concept demonstrating 100 nm resolution, the authors believe this resolution may be improved by improving the signal to noise ratio of the experiment.

The picosecond acoustic technique has also been applied in multilayer structures, here the reflection of the acoustic wave from the multiple layers in the sample leads can lead to interesting effects such as the creation of phononic stop bands [5]. The scattering of the light of the multiple layers also adds complexity to the detection mechanism [15]. A structure which has excited a particular interest in this respect is semiconductor superlattices.

1.1.1 Acoustic Experiments on Semiconductor Superlattices

Superlattices are structures which incorporate periodic layers of different materials, repeated in sequence 10s or even 100s of times. It is possible to create superlattices from different materials such as metals [16] and polymers [17], however since all superlattices used in this work were made from semiconductors, this particular form of superlattice will be the subject of this section. An example of a GaAs/AlAs SL is shown in figure 1.1, in a semiconductor superlattice (SL) such as shown in figure 1.1 the different bandgaps of the constituent materials, result in the formation of a series of quantum wells and barriers. The period of the SL is defined as the sum of the well and barrier widths, $d_b + d_w$. The different bandgaps of the constituent materials also result in the possibility of preferential absorption of the laser

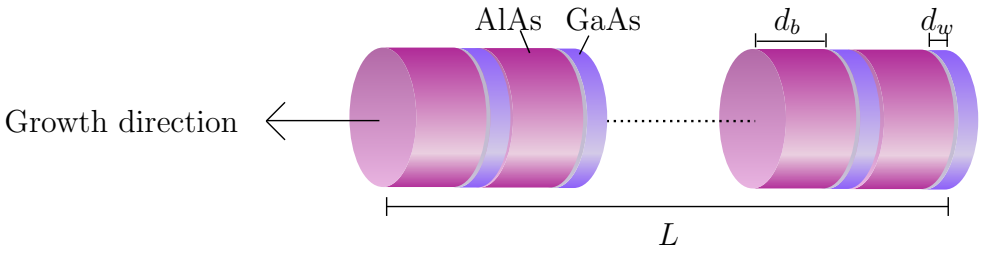

Figure 1.1: Schematic of GaAs/AlAs superlattice, the widths of the wells d_w and the barriers, d_b are shown. L indicates the length of the entire superlattice structure.

light in one material over another, creating a periodically varying stress field. This enables semiconductor SLs, with nanometer periods, to act as effective transducers of quasi-monochromatic acoustic waves with frequencies, defined by the SL period, which can be in the sub-terahertz and THz ranges. Further details about the acoustic properties of semiconductor superlattices will be given in chapter 2. The potential benefits for acoustic microscopy and phonon spectroscopy which may be gained from a high frequency monochromatic source have led to extensive studies of their interaction with light in a variety of experiments.

The generation of acoustic phonons in a superlattice was first investigated in a *pump-probe* experiment by Yasumto et al. [18]. In this experiment the pump and probe beam are both incident on the same superlattice, this means both the generation and detection are influenced by the superlattice structure [19]. Observations of the output of a SL on the opposite side of a substrate, demonstrating the propagation of the generated acoustic waves, were first performed using superconducting bolometers for detection [20, 21]. Superconducting bolometers detect a phonon flux through a change in the resistance of a thin superconducting film as it is heated by the phonons.

The bolometer is a sensitive energy detector due to the high sensitivity of a superconducting film to temperature change when it is held at the temperature which corresponds to its superconducting transition. However, it alone will not give information about the spectrum or frequency of the output of the superlattice structure.

A series of investigations have been performed using *pump-probe* experiments with the pump and probe aligned on different sides of the sample to investigate both generation and detection in superlattice samples these are summarised in the review article by A. Huynh et al. [22]. Pumping and probing on different sides of the sample allows a separation of generation and detection processes in the superlattice structure. This has led to the formation of a detailed theory of both processes [23]. From this analysis and other theortical and experimental works on these structures it is found that *pump-probe* processes in superlattices feature an inherent lack of sensitivity in the reflection geometry normally used. This is caused by selection rules which mean that for an infinite SL the allowed wavevectors for generation and detection do not overlap [24]. Detection is found to be most efficient at frequencies corresponding to the electromagnetic wavevector in the structure while generation is most efficient at zero wavevector, this is shown in figure 1.2. Further discussion of the *pump-probe* experiment in the SL can be found in section 2.2.2. The lack of sensitivity for optical detection in SL has led to a series of experiments investigating ways to enhance the generation and detection of acoustic waves in these structures.

One method used is a version of the experiments described earlier, where generation is in a SL on one side of the substrate and detection in a superlattice on the other. If one of these superlattices is grown with a thickness which varies across the sample, it is possible to enhance the detection condition by moving the sample, this is shown in figure 1.3. This moves the laser spot to an area of the sample featuring a different SL thickness; as the detection selection rules are dependent on the SL thickness it is therefore possible to tune the signal by finding the area where the detection and generation selection rules

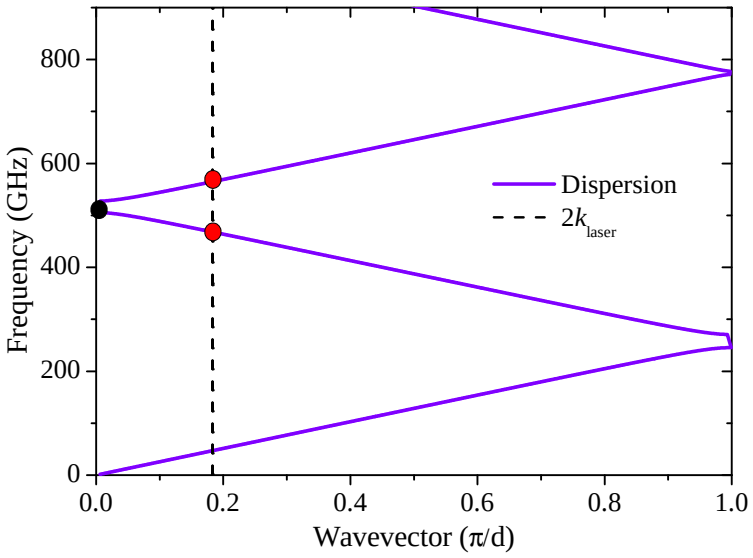

Figure 1.2: Phonon dispersion with the wavevector corresponding to $2k_{laser}$ highlighted. The black circles indicate where generation is efficient, while the red circles indicate where detection is efficient. The dispersion shown is calculated for a SL with 5.9 nm GaAs wells and 3.9 nm AlAs barriers. $2k_{laser}$ is shown for a wavelength of 750 nm.

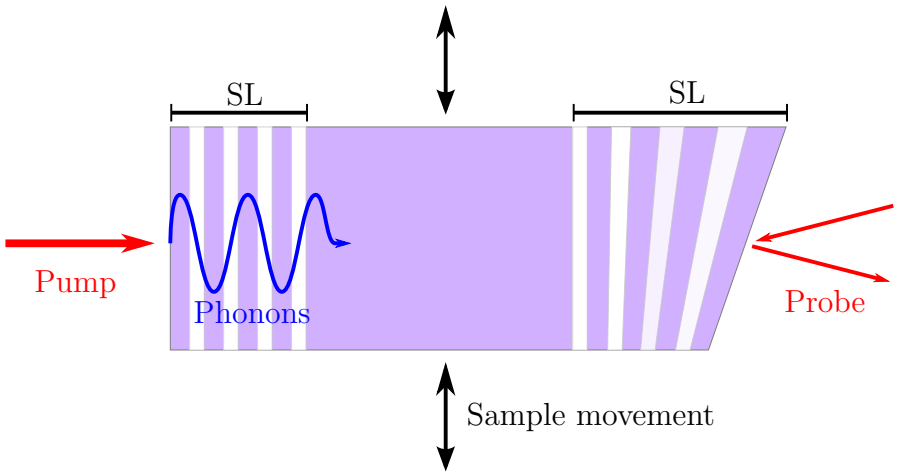

Figure 1.3: Schematic of a *pump-probe* experiment using 2 superlattices, one of which is grown with a thickness gradient to enhance detection.

feature the greatest overlap [19].

It has been shown to be possible to enhance the acoustic generation and detection in a superlattice by including the acoustic structure in an optical microcavity [25]. This causes similar effects to those mentioned earlier in reference to the acoustic microscope. An optical microcavity can be created using semiconductor superlattices. Superlattices incorporate a periodic variation of refractive index as well as of acoustic impedance meaning they can act as optical Distributed Bragg reflectors (DBRs). The use of two DBRs with an appropriately sized spacer in the centre can create an optical microcavity [24]. The presence of the microcavity alters the detection and generation selection rules, leading an enhancement of both processes [26].

The possibility of controlling the acoustic output of a semiconductor SL by using an additional pumping pulse has also been investigated using a method known as coherent control [27]. It was found to be possible to increase or decrease the generation of a specific mode by adjusting the timing between the first and second pumping pulse. Both pulses will produce phonon waves of the same frequency and the timing between the two waves can be tuned such that they are in or out of phase leading to either constructive or destructive

interference.

In this thesis the subject of control of the phonon emission in SLs will be investigated. To achieve this an experimental *pump-probe* scheme was used, which avoids the limitation of SL detection rules through the employment of the electron-phonon interaction in a semiconductor heterostructure. The possibility for control of the amplitude of the phonon beam through an active method using an electrical signal will be investigated. This method has the advantages of ease of use compared to multiple laser pulse techniques. Also it has the advantage, compared to the gradient thickness method or cavity method of enhancing generation, that there is the option of changing the phonon properties within the same experiment without the need for the growth of a new structure.

1.2 Electron-Phonon Interaction in Semiconductor Nanostructures

1.2.1 Electron-Phonon Coupling Mechanisms

In this section a brief review of electron-phonon coupling mechanisms which may potentially effect the devices investigated in this thesis will be detailed. This will be used to identify which mechanisms will be important for consideration in later sections of this work. A more detailed review of electron-phonon coupling mechanisms from the point of view of the generation of acoustic phonons can be found in [28]. The devices discussed in this work were all created from GaAs/AlAs or GaAs/AlGaAs heterostructures and the main ones were grown on the (100) face of GaAs substrates, so this structure will be the main subject of this discussion.

Deformation Potential

The main source of interaction between longitudinal strain waves and the electrons in a structure such as the ones used in this work has been shown to be through the deformation potential mechanism [29]. This describes the effect where strain in a crystal causes a change of interatomic spacing and therefore leads to shift of its energy bands [30]. The magnitude of the shift in energy, ΔE, caused by the strain, ε is defined by a constant known as the deformation potential constant [31], at small values of strain this is linear and can be represented in equation 1.1.

$$\delta E = \Xi_d \varepsilon \tag{1.1}$$

In equation 1.1, the deformation potential constant is represented by Ξ_d.

The value of the deformation potential in GaAs is an important quantity and significant effort has been expended in determining it. This is complicated by the fact that the application of strain to the crystal causes changes to all the energy bands within it, with different bands moving different amounts. Which means a simple measurement of the change in bandgap when a stress is applied to the crystal does not directly give a value of the deformation potential. The devices used for the investigations of this thesis all feature n-doping meaning the value of the conduction band deformation potential is most relevant. A variety of methods have been used to try and measure the value of the conduction band deformation potential. These are mostly related to using transport measurements which can give estimates of the deformation potential through electron-phonon scattering theory. Values proposed for the conduction band deformation potential of GaAs vary between $-6.3\,\mathrm{eV}$ to $-13.5\,\mathrm{eV}$ according to the review of band parameters of III-V semiconductors and their alloys by Vurgaftman *et. al* [32]. These authors suggest the use of the value $-7.17\,\mathrm{eV}$ as derived from theoretical calculations of Chris G. Van de Wall [33]. The minus sign here denotes that the band gap of GaAs expands when the crystal is compressed, different sign conventions may be used in

different works. All of these values will give energy band shifts through the deformation potential mechanism which are much larger than those seen through other mechanisms, confirming that it is the dominant mechanism in these devices.

Piezoelectric Mechanism

In crystals which lack inversion symmetry such as GaAs a piezoelectric effect is present [30]. This is where a strain in the crystal produces an electric field. The inverse effect is also possible where an electric field produces a strain. In some crystallographic directions this effect can lead to a coupling between electrons and phonons. For small values of strain the electromagnetic field produced by the strain is proportional to its magnitude and the proportionality can be expressed through a third-rank tensor [30]. In zincblende structures, symmetry considerations mean that only one component of the piezoelectric tensor is non-zero [34], this component couples to transverse phonons. In the experiments detailed in this work the focus of the laser spot is significantly larger than the absorption length of light in the substrate. In this case coherent transverse phonons are not generated in the (100) substrates that the main experiments detailed in this work are performed on.

Pekar Mechanism

The Pekar mechanism is a mechanism which provides a coupling between electrons and phonons in a crystal in the presence of an external field [35]. The coupling is caused by changes caused to the dielectric permittivity of the crystal by the strain. This dependence of the dielectric permittivity on strain results in the phonons inducing an effective AC-electric field component, causing an additional electron-phonon coupling. This effect has been investigated for nanostructures [36], and was found to be an important effect in silicon inversion layers. It was, however, calculated to not have a significant effect

on a structure similar to the ones used in this thesis [29].

Ripple Mechanism

For semiconductor nanostructures a possible cause of electron-phonon coupling is through the phonon modulating the spatial dimensions of the structure. This results in a change of the confined energy levels within that structure, thorugh the ripple mechanism [37].

The direct consequence of the strain on a quantum well due to this mechanism can be approximately calculated relatively simply. The ground energy level in an infinite quantum well is as shown in equation 1.2 [38].

$$E_g = \frac{\hbar^2 \pi^2}{2 d_w^2 m_{eff}} \tag{1.2}$$

In equation 1.2 d_w is the width of the well and m_{eff} is the effective mass of the electrons within the well. Taking the derivative of this ground state energy with respect to the width of the well, d_w, leads to equation 1.3.

$$\mathrm{d}E_g = \frac{-\hbar^2 \pi^2}{d_w^3 m_{eff}} \mathrm{d}d_w \tag{1.3}$$

We can equate the change in well width $\mathrm{d}d_w$ to the change caused by the strain which is equal to εd_w, where ε is the magnitude of the strain, to give the formula 1.4, for the shift in the energy level caused by the strain.

$$\mathrm{d}E_g = \frac{-\hbar^2 \pi^2}{d_w^2 m_{eff}} \varepsilon \tag{1.4}$$

Evaluating equation 1.4 for the case of a 5 nm QW subjected to a strain of 10^{-3} results in a shift of energy of 0.5 meV, significantly smaller than is expected through the deformation potential mechanism. Here the effective mass used for the conduction band electrons in GaAs was $0.067 m_e$ [39].

In real structures this effect may be complicated by other consequences of the change in the nanostructures dimensions, such as a change in the effective mass of the carriers in the structure [40]. However this effect was again calculated to be insignificant for a structure similar to the ones investigated in this work [29].

1.2.2 Devices which use the Electron-Phonon Interaction in Nanostructures

The interaction of the high frequency coherent acoustic waves described earlier with electrons in semiconductor nanostructures creates the opportunity for coherent control of the electronic properties of semiconductor devices on picosecond timescales [41]. This has already been used to create sensitive detectors of acoustic strain leading to the demonstration of new physics relating to the formation of strain pulses in semiconductors [42]. It is hoped these effects may also lead to the development of a new generation of high-frequency acousto-electric devices. There are two forms of interaction between the coherent strain pulses and the electrons in the nanostructures which have been demonstrated. The application of strain to device which features an electron resonance, such as a device incorporating a quantum well, is known to induce shifts in this resonance in an effect known as the piezospectroscopic effect [43]. Strain has also been shown to have a strong influence on carriers within the depletion region of heterostructure junctions in an effect known as the piezojunction effect [44].

To explain the piezojunction effect an understanding of the band structure of semiconductor devices is necessary. This will be briefly mentioned here, for a more detailed account numerous textbooks are available [38, 45, 46]. When two semiconductor materials featuring different doping types are combined a device known as a *p*-*n* diode is formed [45]. The aligning of the Fermi levels in the device results in a bending of the conduction and valence band in the structure. The band structure of a *p*-*n* diode in the case of zero applied bias

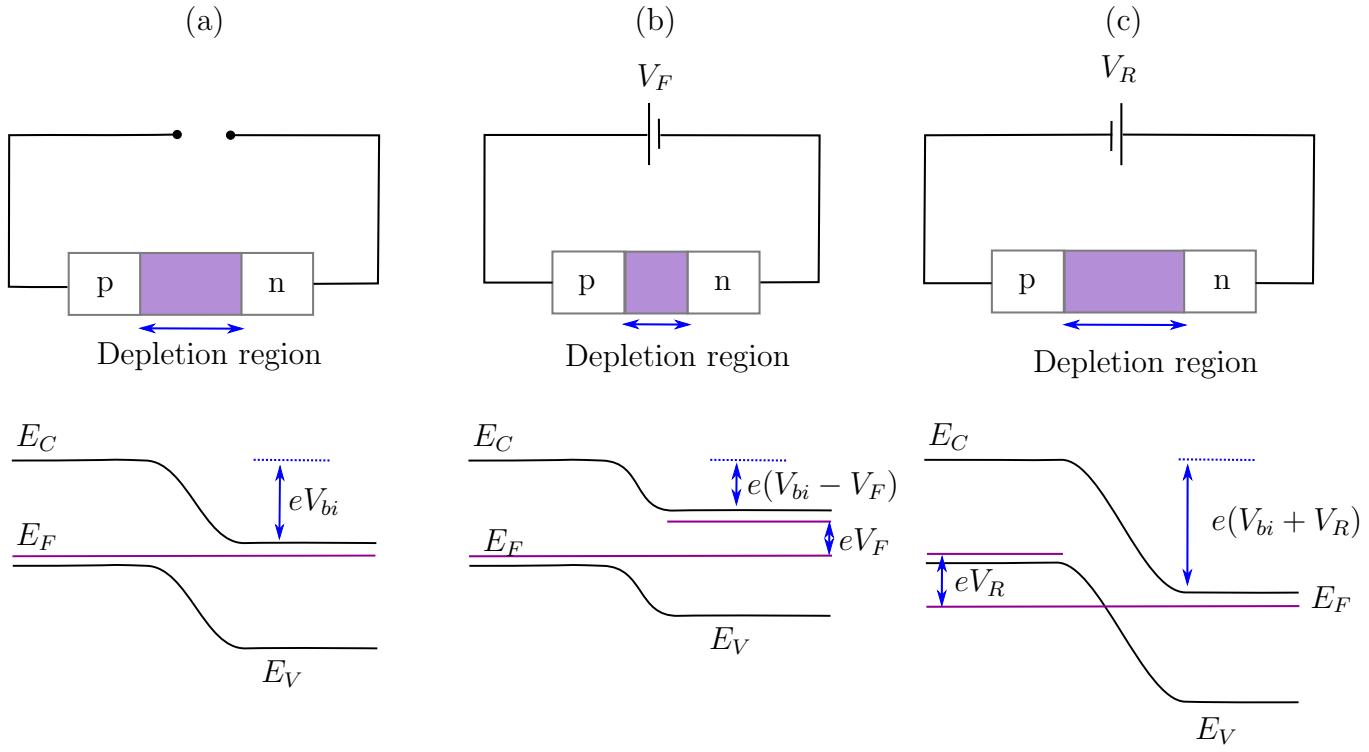

Figure 1.4: Schematic of *p*-*n* junction band diagram. E_F is the Fermi energy, E_V is the valence band energy, E_C is the conduction band energy and V_{bi} is the inbuilt potential. (a) shows the unbiased junction, (b) shows the junction when a forward bias V_F is applied and (c) shows the junction when reverse bias V_R is applied.

is shown in figure 1.4 (a) [45]. When an n type material is placed next to a p type material some of the electrons will diffuse between the two due to the concentration gradient between the more electron rich n material and the p material. Between the p material and the n there will be a flow of holes for the same reason. This leads to an area becoming depleted of charge near the junction, this area is known as the depletion region. The uncompensated donors and acceptors left after this diffusion lead to the formation of an electric field which will limit this diffusion. In figure 1.4 (a) It can be seen how this creates to an inbuilt potential in the device, V_{bi}. This results in an area known as the depletion region, where the structure is depleted of carriers because they are swept out by the field. An important property of the p-n junction diode is its ability to produce rectification. Figure 1.4 shows how this device achieves this. In figure 1.4 part (b) the band diagram for a p-n diode under forward bias is shown. Here the potential barrier in the device is decreased making it is easier for the current to flow. Figure 1.4 part (c) shows the device with a reverse bias applied, in which case the potential in the device is increased preventing the flow of current. The piezojunction effect is when the conductivity of a semiconductor junction is altered by the presence of strain [44]. Considering the band diagrams shown in figure 1.4 it may be seen how shifting the energy levels within the device by strain would result in this effect.

In [47] it was shown that the excitation of a p-n junction with a coherent acoustic strain wave leads to the creation of current in the device. This is attributed to the piezojunction effect. The response of the device was modelled as a parallel plate capacitor, with the depletion region acting as the insulating region between the plates. The strain pulse can then be thought of as causing a redistribution of charge between the plates. Good agreement was found between this model and the experimental results. This device demonstrates the detection of strain using a purely electrical detection mechanism. Electrical detection may prove a useful addition to the previously discussed picosecond acoustic techniques, negating some of the need for complex optical arrangements. Two other devices have been shown to demonstrate the

potential for electrical detection of strain

The Schottky diode, was also found to detect strain through the piezo-junction effect [48]. A Schottky diode is a device formed by junction between a metal and a semiconductor. The junction of these two materials causes a band bending which creates an inbuilt potential, in a similar way as was previously discussed for the *p-n* diode. In this device the mechanism for the measured current when the device was excited by an acoustic wave was the movement of charge to screen the effect of the acoustic wave on the band structure of the device in the depletion region.

A further device shown to provide electrical detection of strain is the double barrier resonant tunnelling diode [49]. This is a device which incorporates an active region where two barriers are utilised to form an effective QW. The device *I-V* then features a resonant peak at voltages when the energy level of this quantum well is shifted to a position which facilitates increased tunnelling in the diode. If the device is initially biased just below the resonant peak the passage of the strain through the device can move the device closer to the resonance increasing the tunnelling current through it. If the device is biased on the resonant peak the opposite is possible with a decrease in tunnelling current being seen. This device exhibits high sensitivity to strain and sub-nanosecond resolution. This makes it a sensitive hypersonic detector featuring a purely electrical detection mechanism and also suggests the possibility of further applications of charge and current control in the devices.

In Chapter 4 the requirements for high sensitivity detection lead to the use of a *p-i-n* photodiode detection method. A *p-i-n* diode is similar to the p-n diode described earlier only with the depletion region extended by the growth of an undoped intrinsic region between the p and n regions of the device. Strain detection through the piezospectroscopic effect is facilitated by the growth of a quantum well in the intrinsic region of the device. The modulation of the photocurrent generated in the QW by a strain wave can be utilised in a *pump-probe* experiment to provide a highly sensitive detector of

coherent strain waves [50] [29]. Further details of the detection mechanisms in this structure will be given in chapter 3.

This thesis focusses on the electron-phonon interaction in GaAs/AlAs semiconductor superlattices. The interaction between electrons and phonons in these structures is primarily through the deformation potential as in the devices above. However, in semiconductor superlattices additional effects have been shown to be present due to the effects of the superlattice periodicity on the electron and phonon behaviour. Previous work on this topic will now be discussed.

1.2.3 Investigations of the Electron-Phonon Interaction in Semiconductor Superlattices

The semiconductor superlattice structure introduced earlier not only has interesting acoustic properties but also distinct electronic properties. The confinement of the electrons in the wells of the periodic structure means that transport within the structure should be considered quite differently to in a bulk structure. Further details of specific transport regimes and their ranges of applicability will be discussed in chapter 2. Detailed accounts of these transport properties can be found in the reviews [51] and [52]. Previous studies of semiconductor superlattices have found interesting effects due to the interaction of the electrons in the structure with photons, such as quantum cascade lasing [53], and parametric oscillations [54]. However, less attention has been paid to the potentially interesting effects of the interaction of phonons with electron in the structures, which will be the focus of this work.

In some superlattices, the interaction between electrons in neighbouring wells is strong enough to lead to the creation of an artificial band structure within the device with a width defined by the SL period. These are known as strongly coupled SLs. It has been shown theoretically that phonons can

induce current oscillations in a strongly coupled SL [55]. This is caused by the acoustic wave dragging the electrons through the superlattice, which at large acoustic amplitudes causes the formation of charge domains. As the acoustic wave travels through the SL these charge regions are dragged along and experience oscillations due to their confinement within the band structure of the SL.

One interesting consequence of electron-phonon interactions in semiconductor superlattices is the potential for acoustic gain within the structure. This could be used for Sound Amplification by Stimulated Emission of Radiation, through the creation of a SASER device. It was shown theoretically in 1999 [56] that phonon gain was possible in a biased semiconductor superlattice. This gain occurs due to phonon assisted electron transitions between the different quantum wells of the superlattice, further details about the mechanism will be given in chapter 2.

Following the initial theory, experimental evidence for the bias dependent increase in phonon emission was given [57]. In this work the phonon emission from a superlattice was measured using a bolometer, and found to show a resonance at bias values corresponding to phonon transitions for the phonons which are trapped in the superlattice due Bragg reflections from the periodic interfaces. In the case of these phonons, it is possible for the superlattice to act as its own cavity providing the feedback requirements for gain. A further experiment was used to make an estimate of the level of this gain by measuring the amplification seen when a phonon beam makes a single pass through the SASER medium [58]. For this experiment, a sample incorporating two SLs was used. The upper one was used as a phonon transducer to emit phonons when excited by the femtosecond laser pulse, while the lower one was used to provide gain. A phonon gain of 20 % was seen in this configuration, this was measured using a bolometer. The bolometer is an incoherent energy detector, as was mentioned earlier, so does not give information about the coherence of the output of the device.

The *pump-probe* technique introduced in the previous section was used, to gain evidence of the coherence of the emission. The pump and probe laser beams were both focussed on a biased superlattice designed with saser specifications, the amplitude of the signal was then recorded as the bias was altered. Again an increase in the signal was seen at the bias which corresponded to a gain for phonons confined in the superlattice structure. The decay of the phonon signal after the optical excitation was also measured when this bias was applied and evidence of an increase in decay time consistent with amplification was seen [59].

The most recent investigation of acoustic gain in a semiconductor superlattice involved including the gain medium in a cavity to allow the creation of a full SASER structure. The cavity was created using two superlattices with the same period. Evidence of a build up of the phonons in this structure analogous to that for photons in a laser structure was shown [60].

This work will detail a study of a possible SASER gain medium using a coherent remote detection mechanism. The coherent detection used previously involved detecting within the superlattice structure complicating the interpretation due to the possibility that the detection mechanism as well as the generation mechanism is affected by the application of bias. It is hoped that detecting remotely will give more information. Remote detection has only previously been performed using incoherent detection mechanisms, limiting the information which can be obtained.

1.3 Motivation for Work and Thesis Outline

Picosecond ultrasonic techniques have already been developed into a wealth of applications for studying the mechanical properties of a variety of materials. The study of phonon processes in semiconductor heterostructures has already led to the realisation of new high sensitivity detectors in this field.

Further studies of this interaction are hoped to produce new acousto-electric devices and new applications of the technique. This work focusses on the electron-phonon interaction in semiconductor superlattices. These devices have previously been shown to exhibit many interesting effects both acoustically and electrically and evidence of interesting consequences of electron-phonon interactions within them has already been seen. This thesis details experiments designed to further investigate electron-phonon interactions in superlattices. It is hoped this work will increase the understanding of these processes and their potential for device applications.

Two different experimental approaches are used to study the superlattices. Chapter 4 details an investigation of the possibility of electrical control of the amplitude of a propagating phonon beam as it travels through a superlattice, using a novel coherent optics experiment. While chapter 5 investigates the possibility of acoustic control of the current within a superlattice using a optical pulse shaping technique to create an acoustic pulse train with tunable frequencies.

Chapter 2 details the theoretical background necessary for understanding these experiments including: theoretical details of the acoustic and electrical properties of semiconductor superlattice, theories of electron-phonon interactions in superlattices relevant to the experimental investigations and the mechanism of strain generation in an aluminium film. The strain generation in an acoustic transducer film is important of an understanding of generation of the acoustic pulse train used in chapter 5. Chapter 3 outlines the device fabrication procedures necessary for creation of the devices used in this thesis and the experimental procedures required for their investigation. Finally chapter 6 summarises the conclusions of the investigations presented and makes suggestions for further work in this field.

Chapter 2

Background Theory

2.1 Introduction

This chapter will briefly detail some of the background theory necessary for an understanding of the experimental results presented in later chapters. The main body of the investigation presented in this thesis concentrates on electron-phonon interactions in semiconductor superlattices (SLs), their acoustical and electrical properties will therefore be outlined. Two specific theories of electron-phonon interactions within semiconductor superlattices which apply to the different investigations in this thesis will be detailed.

This chapter also features a discussion of the use of an aluminium film as an acoustic transducer. Aluminium film transducers are used as a source of coherent strain waves in this work, and are important for an understanding of the results presented in chapter 5.

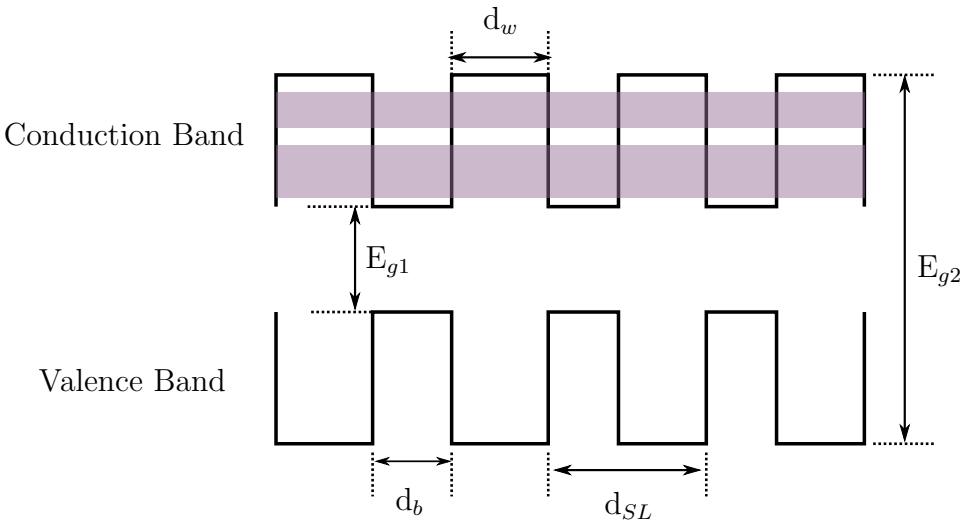

Figure 2.1: Schematic of superlattice bandstructure with shaded areas representing the first two minibands in the conduction band. The period of the superlattice is labelled d_{SL} and the widths of the wells (d_w) and barriers (d_b) as well as the corresponding energy gaps of the two materials present are shown.

2.2 Semiconductor Superlattices

The semiconductor SL forms an additional lattice within the bulk crystal lattice with a period corresponding to the period of the SL given by equation 2.1, a schematic of the energy band structure in the SL is shown in figure 2.1.

$$d_{SL} = d_w + d_b \tag{2.1}$$

In equation 2.1 d_{SL} is the period of the superlattice, d_w is the width of the SL GaAs wells and d_b is the width of the AlAs barriers. The superlattice period is of the order of 10's of nanometres as opposed to the lattice periodicity tenths of nanometers seen in bulk crystals. This additional periodicity leads to the interesting electronic and acoustic effects as will be further discussed here.

2.2.1 Electronic Properties of the Semiconductor Superlattice

The SL was initially developed by Esaki and Tsu in 1970 [61]. They hoped that by creating an artificial crystal with an increased period and hence reduced band structure they could observe Bloch oscillations. This is an effect where electrons within a band perform periodic oscillations in an applied electric field. The effect is possible if the electrons can accelerate to the edge of the band without being affected by scattering, at which point the dispersion of the band causes them to decelerate. In the initial work on SLs this effect was not seen because the SLs studied did not feature strong enough coupling between the quantum wells. SLs only display the property of conduction in a band defined by the SL period when the coupling between the quantum wells in the structure is strong enough that the electrons can be described by extended states incorporating many of the quantum wells of the structure. For many SLs the coupling between the quantum wells is not this strong, and the transport properties are best described using discrete equations where the electrons are isolated in separate wells [51].

A lot of work both experimentally and theoretically was undertaken using semiconductor SLs before the distinction between weakly and strongly coupled SLs was fully defined. The 2005 review of non-linear dynamics of semiconductor superlattices by Bonilla and Grahn [51] claims to be the first work to fully address this issue, dealing with both theoretical descriptions and experimental observations in the case of weakly and strongly coupled SLs. Although the previous theoretical review of nonlinear transport in superlattices by Wacker [52] also includes a description of the validity of the different transport models. The need for a different approach when considering weakly coupled SLs compared to strongly coupled is emphasised by both these reports. A brief description of the appropriate transport regimes for both strongly and weakly coupled SLs will be included here to highlight the differences. Detailed descriptions of the different transport regimes are not

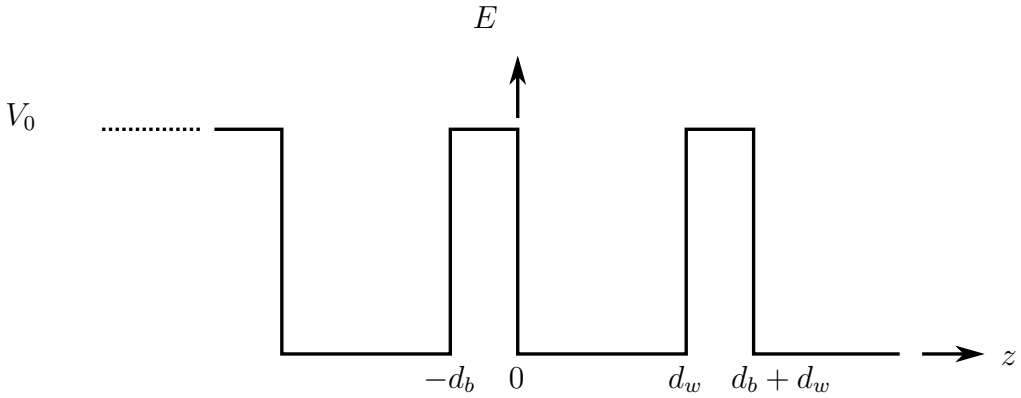

Figure 2.2: Potential used in Kronig-Penny model. d_b is the width of the barrier, d_w is the width of the well and V_0 is the height of the potential. In the case of the SL this is the proportion of the difference in the energy bands of the bulk constituents of the structure which appears in the conduction bands. The growth direction of the superlattice is labelled as z

included because this is a large topic within itself and not relevant to this thesis which focusses on phonon specific transport properties.

When a SL with strongly coupled quantum wells is considered, miniband transport and Wannier-Stark hopping are applicable. When the electric field applied to the device is small transport happens via the mini-bands, but at higher fields the tilting of the bands leads to localisation of the electrons within the wells, causing the creation of a Wannier-Stark ladder of states [62]. One criteria for the SL leaving the miniband transport regime is the splitting between wells exceeding the miniband width.

The width of the miniband can be obtained directly from the crystal band-structure of its constituent atoms, or using a full **k.p** model. However, an estimate can be obtained using the Kronig-Penny model [63]. In the Kronig-Penny model a square well potential is used [64]; this can represent the SL when it is defined in terms of constituent materials of the superlattice, as is shown in figure 2.2. The 1 dimensional Schrödinger equation is then solved for this system. In the region $0 < x < a$, the well region, the eigenfunction is

as given in equation 2.2.

$$\psi = Ae^{ik_w z} + Be^{-ik_w z} \tag{2.2}$$

In equation 2.2 k_w is the electron wavevector in the well, with z being the SL growth direction as shown in figure 2.2. The energy in this case is

$$E = \frac{\hbar^2 k_w^2}{2m^*}, \tag{2.3}$$

where m^* is an average effective mass of the system, as will be further explained later. In a similar manner in the barrier region, $-b < x < 0$, the eigenvalue is defined as in equation 2.4.

$$\psi = Ce^{k_b z} + Be^{-k_b z} \tag{2.4}$$

In equation 2.4, k_b is the electron wavevector in the well. Equation 2.4 is written for the case when $E < V_0$. The energy in this case is

$$E - V_0 = \frac{\hbar^2 k_b^2}{2m^*}, \tag{2.5}$$

The boundary conditions that both ψ and $\mathrm{d}\psi/\mathrm{d}z$ must be continuous at the boundaries $z = a$ and $z = 0$, are then applied. The eigenfunction for the region under the barrier at $z = a$ is formed by application of the Bloch function shown in equation 2.6.

$$\psi(a < z < a + b) = \psi(-b < z < 0)e^{ik_{SL}(d_b + d_w)} \tag{2.6}$$

Equation 2.6 defines the wavevector of the SL, k_{SL}. The solution of the set of 4 equations formed by the application of equation 2.6 and the boundary conditions can then be solved to give equation 2.7.

$$\cos(k_{SL} d_{SL}) = \cos(k_w d_w)\cosh(k_b d_b) - \frac{k_w^2 - k_b^2}{2k_w k_b}\sin(k_w d_w)\sinh(k_b d_b) \tag{2.7}$$

The miniband width can then be found by solving equation 2.7 in a numerical

manner, using some trial energies in equations 2.3 and 2.5 then substituting these in the right hand side of equation 2.7. The values where minibands can exist are the values that correspond to propagating states i.e. those where the magnitude of $\cos kd_{SL}$ is less than 1. When this is not true there are band gaps. This model has problems when used for a SL formed of different material such as used in this work, because the application of the boundary conditions described above require a single effective mass be used for the whole material. A solution to this problem is to use a weighted average of the effective mass in the two materials as the effective mass in the structure. It is possible to define different boundary conditions which allow the use of the different effective masses in the different materials [65], however comparison with the **k.p** model did not find this model to be more accurate for the estimation of mini-band widths [63] so it will not be used here. Transport within the miniband was first described by Esaki and Tsu in 1970 [61] using a semiclassical equation of motion in 1D. There have since been many variations in the models for conduction within the miniband [63].

At high fields electrons can no longer act as extended states and the miniband model becomes invalid, at these fields the Wannier-Stark model is often used to describe the transport in the structure [51]. The electrons no longer act as extended states due to the tilting of the miniband caused by high electric fields. The eigenstates of the electrons in each energy level are confined to the miniband, so will become localised upon tilting. The distance they become localised to is known as the localisation length and is described in equation 2.8.

$$\xi \approx \frac{\Delta}{eF} \tag{2.8}$$

Where ξ is the localisation length and Δ is the miniband width which was discussed above. The energy separation between subsequent wells, known as the Stark splitting, is given by equation 2.9.

$$\Delta_S = eFd_{sl} \tag{2.9}$$

F being the applied field [63, 66], and other symbols as before. When energy

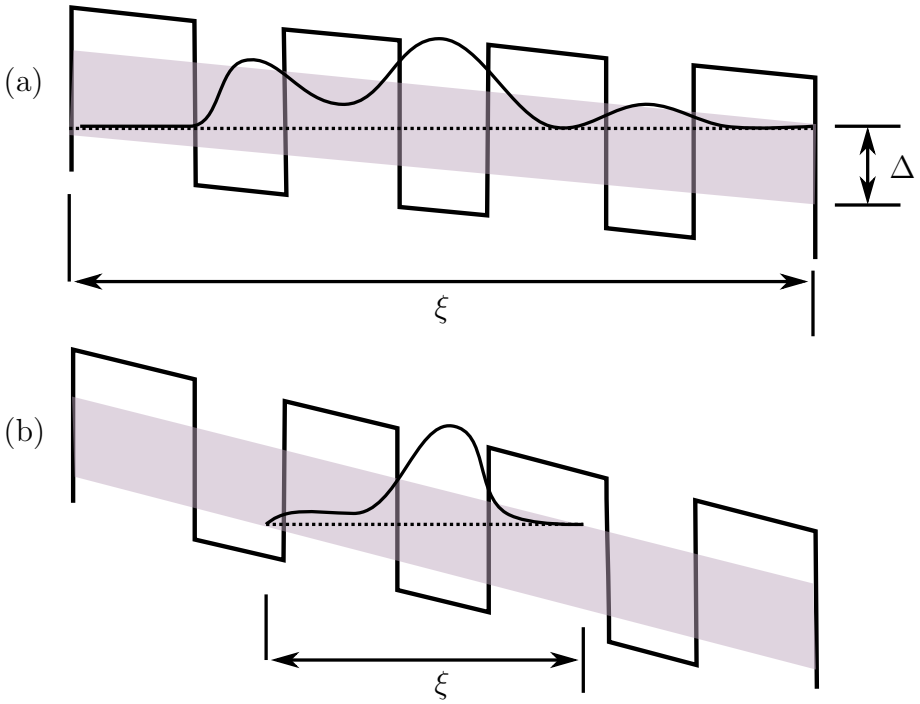

Figure 2.3: Schematic of stark localisation in a SL. The SL profile is shown by the narrow lines, the shaded area is used to represent the miniband width, the bold line represents an electron eigenstate state and the dashed line represents the localisation length, ξ. (a) depicts a lower field than (b) and the localisation length is correspondingly larger.

separation is of equal magnitude to the miniband width, the localisation length will be one period of the SL, leading to the carriers being localised within a single well; conduction then occurs through hopping between wells. This localisation is illustrated in figure 2.3.

For a full description electron scattering should also be included. Electron scattering induces a broadening in the quantum well energy levels and stabilises the minibands. This prevents full localisation of the minibands to a Stark ladder, but transport through the miniband is disrupted by the field and the Esaki-Tsu band model is no longer valid; as explained in the work of R. Tsu and L. Esaki [67] with an erratum [68]. The criterion for a SL moving between the miniband regime and the Wannier Stark regime is as defined in

equation 2.10, when scattering is considered.

$$eFd_{SL} > \Gamma \tag{2.10}$$

In equation 2.10, Γ is the scattering induced broadening defined by $\frac{\hbar}{\tau}$, where τ is the scattering time, and all other symbols are as before. Equation 2.10, defines when the field induced interwell separation is greater than the broadening of levels. Once the criterion for hopping is fulfilled, the regime will then be valid until the interwell energy separation is large enough for the levels which have been localised in the first miniband to interact with the second, at which point electric field domains can start to form as will be discussed later.

If the coupling between wells in a SL is weak, the sequential tunnelling model should be used. This model assumes the electrons are centred in separate wells even at zero applied electric field. In this case no miniband transport can occur and transport between the wells occurs via a combination of tunnelling and scattering. As the electric field is applied the current exhibits a series of peaks and plateaus as the Fermi levels of the energy states in successive wells align, leading to resonant tunnelling between them [69]. This is demonstrated in figure 2.4. There is also a background non-resonant current seen which is caused by scattering of electrons between wells [52].

In a sequential tunnelling model of SL transport, the device I-V exhibits a series of peaks due to the alignment of different energy levels in the the quantum wells. This can be explained by considering the tunnelling between two wells with multiple energy levels, as demonstrated in figure 2.4. When a low electric field is applied, tunnelling will be strong between the lowest energy levels of the quantum wells. This corresponds to an approximately ohmic region at low biases. At higher biases the energy gap between the levels will increase, eventually leading to a decrease in the current seen, until the lower energy level in the first well is aligned with a higher energy level in the second. When this happens there will be an increase in the tunnelling

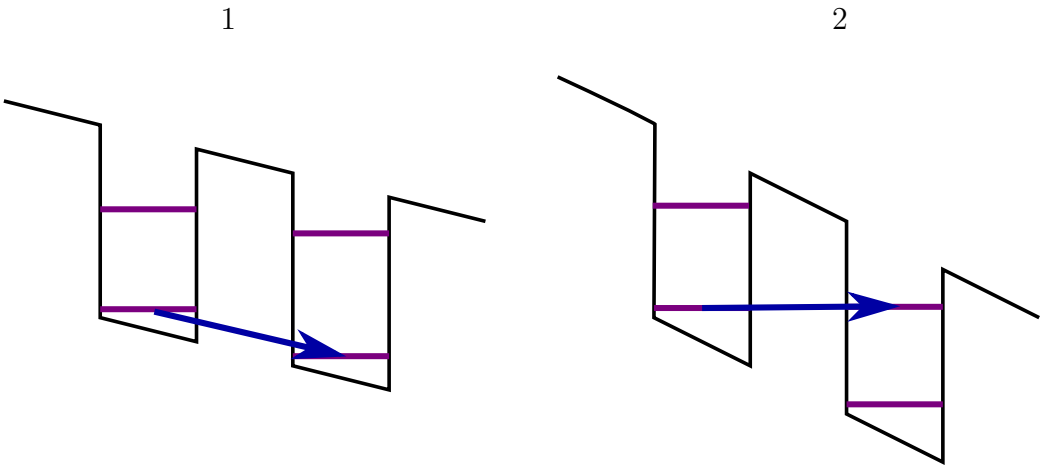

Figure 2.4: Schematic demonstrating a resonant tunnelling process. Case one represents a low electric field situation. Here the dominant tunnelling is between the lowest energy levels in the quantum wells, as represented by the blue arrow in the figure. Case two represents a case with increased electric field where the dominant tunnelling mechanism has become tunnelling to the second energy level, again represented by a blue arrow.

probability and consequently an increase in current will be seen [69]. This results in the formation of electric field domains in the device as will be further discussed later in this section.

In both the Wannier-Stark hopping case and in the sequential tunnelling case the localisation of the electrons to one well means the wavefunctions of the electrons are best described by Wannier functions. Wannier functions are the Fourier transform of Bloch functions and are indexed by lattice vectors in real space, making them more appropriate for use in the case of localised states than Bloch functions [30]. When converting from Bloch functions to Wannier functions the shape of the Wannier function is determined by a complex phase factor which multiplies the Bloch function [70]. It is this phase factor which leads to the differences between Wannier-Stark hopping and sequential tunnelling [69]. When the wells are coupled the phases of the different wells in the SL are coherent, but in the case of weak coupling this coherence is broken. Scattering plays a large role in determining the coherence between wells; with large scattering probability potentially leading

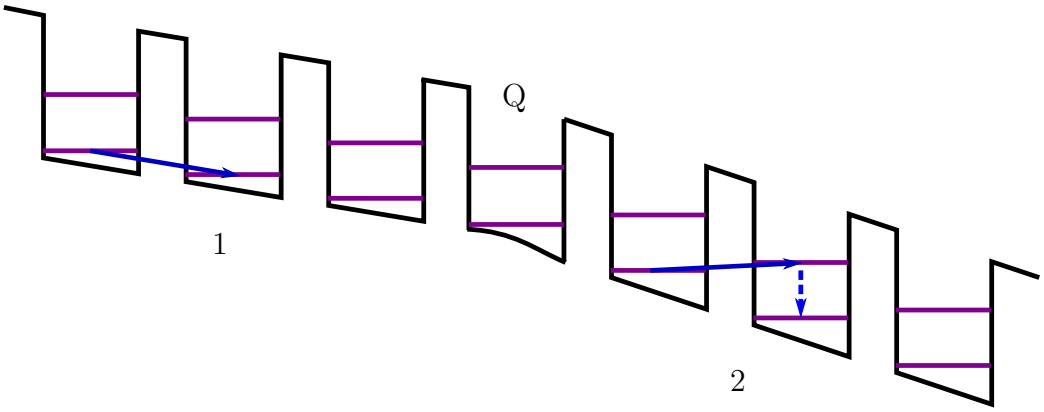

Figure 2.5: Schematic demonstrating domain formation in a resonant tunnelling SL. The purple lines represent the energy levels in the QWs while the blue arrows represent the electron movement. The QW labelled Q features an area of charge accumulation. This results in the electric field in the region labelled 2 being higher than that in the region labelled 1.

to a loss of coherence. The sequential tunnelling regime is applicable when the condition specified in equation 2.11 is fulfilled.

$$W_1 \ll \frac{\Gamma}{\sqrt{2}} \tag{2.11}$$

Where W_1 is the interwell coupling and Γ is the scattering induced broadening as discussed in equation 2.10 [69]. When this condition is true there is not enough coupling between the wells to allow the creation of a miniband. When an electric field is applied the Wannier-Stark hopping model will be valid if the Wannier states stay coherent throughout their spatial extent.

At high levels of electric field the SL transport in both the the case of strongly and weakly coupled quantum wells moves into a new regime. This is characterised by the formation of electrical field domains. These domains are due to an area of charge accumulating in the device leading to the creation of regions with different levels of electric field within the structure. This has been investigated both experimentally [71, 72] and theoretically [51, 52]. As might be expected the formation of, and type of, domains seen varies between weakly and strongly coupled SLs. In strongly coupled SLs travelling domains

are formed, which is similar to the Gunn effect in bulk semi-conductors and results in current self-oscillations. This is where the periodic motion of the domains results in a periodic oscillation of the current at a particular bias. These unstable oscillations do not produce a periodic structure in a stationary I-V measurement because in this measurement the domains will be averaged out [71].

In weakly coupled SLs it is possible for the domains to become pinned in certain parts of the structure leading to the formation of two stationary regions of electric field, this is shown schematically in figure 2.5 [69]. This behaviour can be seen in stationary I-V curves as a series of periodic changes in the value of current which occur as the domain wall moves along the structure. Strongly coupled SLs never featured pinned domains, because this feature is only possible in structures described by discrete equations. However weakly coupled SLs can feature both static and travelling domains [51, 73], with doping being an important factor for determine which will occur [74, 75]. The form of the domains occurring is also strongly related to the effects of the contacts [74, 75]. This makes a description of the behaviour of a weakly coupled SL in the domain regime complicated [51], partially for this reason, and partially because the behaviour of interest is expected to occur there, the experiments in this work concentrate on SLs at voltages below those of domain formation.

A simple estimate was employed to try to gain an appreciation of which transport regime the main SL used in this work, details of which are given in 3.3.1, is best modelled in. The previous discussion of this was in terms of the interwell coupling. For a simpler estimate the coupling between the wells is characterised in terms of the miniband width which can be estimated using the Kronig-Penny model discussed earlier. Applying this to the main SL discussed in this thesis, which features 3.9 nm AlAs wells and 5.9 nm GaAs barriers, a miniband width of 0.7 meV is obtained. This was found using a weighted average of the effective masses in GaAs and AlAs for the SL, with effective mass values taken from [32]. The bandgap of AlAs was taken as

3.04 eV and GaAs as 1.519 eV [39]. These are values for a type I superlattice, for a discussion of this distinction see [63] or [38]. The value of the conduction band offset was taken as 0.45 as given in [76]. In [51] weakly coupled SLs are characterised as having a small miniband width compared to the scattering induced broadening. In this case the time for an electron to escape from the quantum well will be quicker than the scattering time of the electrons, implying that the electron distribution in the wells is in local equilibrium. An estimation of broadening of the energy levels due to scattering can be made using the electron mobility as shown in equation 2.12.

$$E_{sca} \approx \frac{\hbar e}{\mu m^*} \tag{2.12}$$

In equation 2.12 μ is the electron mobility, m^* is the electron effective mass and e is the charge on an electron. An estimate of the mobility of the structure was taken as $4300\,\mathrm{cm^2\,V^{-1}\,s^{-1}}$ [77] this gives an estimate of the broadening due to the scattering of ≈4 meV, significantly larger than the miniband width putting the SL used in the experiments described later in this thesis firmly into the weakly coupled regime.

2.2.2 Acoustic Properties of the Semiconductor Superlattice

As well as a periodic variation of the bandgap of a material the creation of a SL also produces a periodic modulation of the acoustic impedances of the structure. An understanding of the effect of this large scale periodicity on the phonon dispersion can be gained by a consideration of the Bragg conditions for reflection within a SL, which can be written as shown in equation 2.13 [64].

$$n\lambda = 2d\cos(\theta) \tag{2.13}$$

In equation 2.13 n is an integer; λ is wavelength; d is the spacing between layers, in this case the SL period; and θ is the angle of the incident wave. For

large layer spacings, like those in a SL, this Bragg condition is satisfied by acoustic phonons [78]. These phonons are then reflected in the SL and do not propagate propagate through, leading to the formation of stop bands within the phonon dispersion. Considering phonons propagating perpendicular to the SL growth direction the Bragg condition in reciprocal space is shown in equation 2.14,

$$2q = mG_0, \tag{2.14}$$

where $G_0 = 2\pi/d_{SL}$ and $q = 2\pi/\lambda$ [78] is the phonon wavenumber. Phonons will be reflected when, $q = m\pi/d_{SL}$ leading to stop bands. At these stop bands the phonon dispersion can be viewed as being folded back to create a mini-Brillouin zone of width π/d_{SL}.

Quantitative calculations of the phonon dispersion in a SL are important both for the design of structures and for the identification of modes seen in experiments. The phonon dispersion in a SL can be obtained using the Rytov model [79]. This model is a general one concerning the propagation of acoustic phonons in all layered mediums. It is valid when elasticity theorem holds and the acoustic phonon dispersion is linear [30]. The model is strictly valid only for infinite SLs, the errors induced by using it for a finite SL have been investigated [80] and it was determined that the model is sufficient for SLs of more than 20 periods [81]. The phonon dispersion found for a SL in this model is given by equation 2.15.

$$\cos(qd_{SL}) = \cos\left(\frac{\omega d_w}{v_w}\right)\cos\left(\frac{\omega d_b}{v_b}\right) - \frac{1+\delta^2}{2\delta}\sin\left(\frac{\omega d_w}{v_w}\right)\sin\left(\frac{\omega d_b}{v_b}\right) \tag{2.15}$$

In equation 2.15, ω is the phonon frequency, v_w is the phonon velocity in the well material, v_b is the phonon velocity in the barrier material, and $\delta = \rho_w v_w/\rho_b v_b$ is the ratio of the acoustic impedances of the materials, where ρ is the density of each respective material [78]. An example of a dispersion relation calculated from this equation can be seen in figure 2.6a.

The transmission of phonons through the SL as a function of frequency is also an important quantity and can be calculated using a transfer matrix

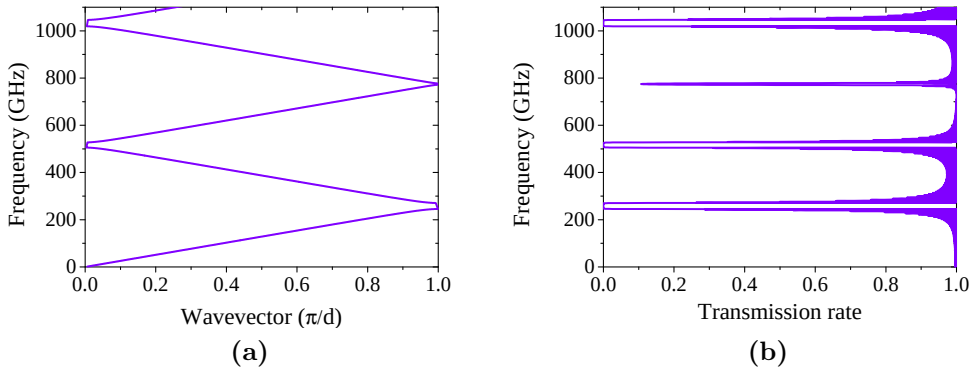

Figure 2.6:
(a) Example dispersion relation calculated for a 5.9nm well 3.9nm barrier GaAs/AlAs SL.
(b) The corresponding transmission rate calculated for a 50 period SL with these properties.

method, this is described in the work of Tamura et al. [78]. An example of the transmission rate calculated in this manner can be seen in figure 2.6b. As is expected from the discussion above, the transmission goes to zero at the frequencies where stopgaps appear in the dispersion. The magnitude of the dips in the transmission is related to the size of the stop gaps and the number of periods in the SL, with more periods corresponding to a better defined gap.

The different values of the band gaps of the constituent materials in a SL mean that, there will be a range of wavelengths when the laser light will be absorbed in the QWs of the structure but not the barriers. This causes a strain field with the period of the SL, leading to the generation of quasi-monochromatic acoustic waves with frequencies corresponding to the $q = 0$ cases of the phonon dispersion. SLs therefore provide a means of generation of quasi-monochromatic waves in the THz and sub-THz ranges, with a frequency which can be tuned by an alteration of the SL period. This property makes SLs attractive for a number of technical applications such as the imaging of nanostructures and high resolution acoustic microscopy. This has led to many

studies of their phonon generation and detection properties, [20, 22, 23, 82], to give just a few. As these properties are important for an understanding of some aspects of this work they will briefly be reviewed here.

As stated earlier the generation of quasi-monochromatic acoustic waves in a SL is due to the absorption of a short pulse of laser light in the QWs of the structure. The laser light is absorbed into the semiconductor by the creation of electron-hole pairs. To create this acoustic wave it is therefore necessary to excite the SL with light of a shorter wavelength than that required for absorption by the first transition in the quantum well of the SL, the heavy hole to electron transition [20]. The width of the quantum wells in the SL therefore dictates the wavelengths at which it is possible to use a SL as a transducer for quasi-monochromatic acoustic waves. This is an important consideration for some of the experiments in this work as will be further discussed in relation to specific samples in section 3.3.1.

The SLs detailed in this work were all grown on the (100) plane of GaAs with the growth direction corresponding to the [001] direction. When such a SL is excited with a laser, using a spot size much larger than the absorption length of light within the sample, it generates a purely longitudinal wave travelling in the [001] direction [23]. There are two mechanisms discussed in relation to the generation of acoustic waves from this process. A displacive mechanism and an impulsive mechanism. The displacive mechanism refers to generation of phonons either through thermal dilation or electronic effects characterised by the deformation potential [83]. The impulsive mechanism refers to stimulated Raman scattering when the pump induces a polarization in the sample, [23], [82]. Knowledge of the specific method is not essential for the analysis of the output of the SLs in most experiments [22].

An important experiment to characterise the phonon generation in a SL is the reflection *pump-probe* experiment, this was first used on SLs in 1994 by Yamamoto et al. [18] and since then has been used extensively. Details about *pump-probe* experiments in SLs have already been mentioned in section

1.1.1. Further specifics about the *pump-probe* experiments used in this work will be given in section 3.6. The detection predominantly occurs through photoelasticity, where the refractive index of a material is altered by the stress it feels. It is also possible to see a signal due to the movement of the interfaces induced by the phonons [84], however this effect is smaller than the photoelastic effect in GaAs [23]. When this reflection *pump-probe* technique is used in SLs it is found that the generation processes are sensitive for 0 wavevector, while the detection processes are sensitive for phonons with wavevector $2k_L$, where k_L is the laser wavevector [24]. This was shown diagrammatically in section 1.1.1. The lack of overlap between these two frequencies means that, in the case of an infinite SL, no signal would be seen in a *pump-probe* experiment. In real experiments the selection rules for phonon wavevector, are relaxed due to the finite size of the SL and light absorption effects [23]. This means a signal can be seen, however reflection *pump-probe* experiments in SLs have quite a low sensitivity to acoustic waves. Alternative methods of coherent detection of acoustic waves will be discussed in chapter 3.

2.2.3 Theory of Transport Induced by Hypersonic Excitation of the Semiconductor Superlattice

The following theoretical explanation for the experimental results presented in chapter 5 was developed by Alexander Balanov from the University of Loughborough. The approach taken was to use an adaptation of John R. Tucker's theory of quantum mixing, this is detailed in reference [85].

Tucker's work describes mixing in the case of non-linear single-particle tunnel junctions. He employs a transfer Hamiltonian formulation of tunnelling theory to develop a dynamic tunnelling model. This model is then used to describe the current in a super-Schottky diode, a diode formed by the interface of a superconductor and a semiconductor. The response of the diode to a sinusoidal potential and thereby the current response expected when the

device is irradiated with microwave radiation is examined. After which he goes on to develop a quantum theory for heterodyne mixing in this device. The full quantum theory features considerable complexity. Fortunately, the results relevant for the analysis here were later summarised by Tucker and Feldman in the form of a simple model [86]. This will be briefly discussed here, before the case for acoustic excitation of a semiconductor SL is given.

Theory of direct detection of millimeter-wave quanta

The section of Tucker's theory used to produce a description of the experiment detailed in chapter 5 is his description of the quantum response of a non-linear tunnel junction at high frequencies. He describes the response of the device when a DC bias and an AC signal are applied simultaneously. The case relevant to the situation in chapter 5 is when the magnitude of the AC signal is small enough that the device acts as a direct detector. When the magnitude of the AC signal becomes stronger the device will start to respond to small changes in the amplitude of the incoming radiation, enabling it to act as a heterodyne mixer, this regime is not relevant for these experiments. The theory applied in that case will therefore not be discussed here.

Tucker's theory of direct detection represents an extension to a previous model of photon-assisted tunnelling developed by Tien and Gordan [87]. The theory models the situation that a DC bias is applied to the junction, then it is irradiated by an AC photon signal. This creates a time dependent voltage such as shown in equation 2.16.

$$V(t) = V_{DC} + V_{\omega}\cos(\omega t) \tag{2.16}$$

In equation 2.16, V_{DC} is the DC voltage, V_{ω} is the voltage induced by the AC field and ω is the angular frequency of the alternating field. Assuming that the applied voltage modulates the potential energy of the particles on the ungrounded side of the barrier adiabatically, it is found that the probability

amplitude for each particle to be displaced in energy by $n\hbar\omega$ is equal to $J_n(eV_\omega/\hbar\omega)$. Here n is an integer, e is the charge on an electron and J_n is the ordinary Bessel function of order n. Modulating all the electron states together like this is equivalent to applying DC voltages of $(V_{DC} + n\hbar\omega/e)$ across the junction. The probability of this occurring, $J_n^2(eV_\omega/\hbar\omega)$, depends on the AC signal amplitude V_ω. This leads to a DC tunnelling current of

$$I_0(V_{DC}, V_\omega) = \sum_{n=-\infty}^{+\infty} J_n^2(eV_\omega/\hbar\omega) I_{DC}(V_{DC} + n\hbar\omega/e). \tag{2.17}$$

Treating the device as a direct detector, for small AC signals, equation 2.17 may be expanded to the lowest order in V_ω, using the expansions for the Bessel functions $J_0(x) \approx 1 - x^2/4$ and $J_{\pm n}(x) \approx (\pm x/2)^n/n!$. This gives an incremental DC current as shown in equation 2.18.

$$\Delta I_{DC} = \frac{1}{4} V_\omega^2 \left[\frac{I_{DC}(V_{DC} + \hbar\omega/e) - 2I_{DC}(V_{DC}) + I_{DC}(V_{DC} - \hbar\omega/e)}{(\hbar\omega/e)^2} \right] \tag{2.18}$$

When the energy of the incident radiation is sufficiently small that the conductance of the device varies slowly on the voltage scale of $\hbar\omega/e$ the form in square brackets can be replaced by the second derivative $d^2 I_{DC}/dV_{DC}^2$. Here we are assuming that the current is following the AC field instantaneously [52]. Equation 2.18 then reproduces classical rectification theory [86].

Application for a weakly coupled semiconductor SL

The approach detailed in the previous section was applied to the case of the irradiation of a weakly coupled SL in terahertz electric fields by Keay et al. [88] and subsequently by Wacker et al. [89]. A detailed theoretical account can be found in the later review of transport in superlattices by Wacker [52] and the review of photon assisted tunnelling in semiconductor nanostructures by Platero and Aguado [74].

The interpretation of the Tucker model given above for the case of sequential tunnelling current in a weakly coupled SL, will now be explained. When a DC field is applied to the SL the energy gap between the lowest levels in neighbouring wells of the structure is defined by eFd_{SL} where F is the field applied and d_{SL} is the superlattice period. The current in this device is a result of sequential tunnelling events between each pair of neighbouring wells, in the case of biases below the threshold for domain formation which will form the basis of this discussion. When the SL is irradiated by microwave photons this allows the possibility of absorption or emission of a photon during the tunnelling process. The tunnelling then corresponds to an energy difference $eFd_{SL} \pm n\hbar\omega$ where $\hbar\omega$ is the photon energy. The probability that each tunnelling event occurs is again represented by a Bessel function and an equation for the current in this situation can then be formed by a weighted sum of all possible photon assisted transitions in a similar manner to equation 2.18 [52].

For the work detailed in this thesis the above approach was adapted to deal with phonon assisted tunnelling as opposed to photon assisted tunnelling. In this case the interaction between the electrons in the structure and the irradiating wave will be mediated by the deformation potential. The case considered is one of a SL uniformly excited by a single frequency phonon wave.

The acoustic wave will cause a modulation of the energy levels in the SL through the deformation potential, this will cause an acceleration of the electrons stimulating tunnelling between the different quantum wells in the structure. This action can be represent by an effective field in the SL oscillating with the angular frequency of the acoustic wave ω. As we are formulating this theory within the sequential tunnelling model of superlattice transport we should consider each well separately. Therefore we consider the potential over a signal period of the structure, $\varepsilon D/e$, will lead to an electric field of $\varepsilon D/(ed_{SL})$ where ε is the strain magnitude, D is the deformation potential and the other symbols are as before. Then in an analogous manner

to Tucker's theory, when the SL is subjected to a DC bias and this acoustically produced field the time dependent voltage can be represented by equation 2.19.

$$V(t) = V_{DC} + \frac{\epsilon D d_L}{e d_{SL}} \sin(\omega t) \tag{2.19}$$

In equation 2.19 d_L represents the length of the superlattice while all other symbols are as before. In the case of excitation with an acoustic wave an additional current is expected due to phonon assisted tunnelling events. The probability of the phonon assisted tunnelling events is represented by Bessel functions and the total current formed by the radiation is then a sum of all the possible phonon assisted events as shown in equation 2.20.

$$I_0(V_{DC}, \alpha) = \sum_{n=-\infty}^{+\infty} J_n^2(\alpha) I_{DC}\left(V_{DC} + \frac{n\hbar\omega}{e}\right) \tag{2.20}$$

In equation 2.20, I_{DC}, represents the stationary current seen when no strain is applied, α is the ratio between the strength of the field created by the acoustic wave and the phonon energy defined by

$$\alpha = \frac{\epsilon D d_L}{\hbar\omega d_{SL}}. \tag{2.21}$$

When α is small, the incremental change in the DC current caused by the AC field can be found by expanding the Bessel functions in 2.20, and taking the difference between current seen when no strain is applied and the strain induced current. This gives

$$\begin{aligned} \Delta I(V_{DC}) = -I_0(V_{DC}) - I_{DC}(V_{DC}) = \\ = \frac{1}{4}\left(\frac{\epsilon D d_L}{e d_{SL}}\right)^2 \times \\ \times \left[\frac{I_{DC}(V_{DC} + \hbar\omega/e) - 2I_{DC}(V_{DC}) + I_{DC}(V_{DC} - \hbar\omega/e)}{(\hbar\omega/e)^2}\right]. \end{aligned} \tag{2.22}$$

Equation 2.22 features a second difference form, in the square brackets, and

as such this can be reduced to the second derivative of the DC I-V curve when the phonon energy is smaller than the voltage scale of the non-linearity in the I-V curve. In this case equation 2.22 reduces to

$$I(V_{DC}) = \frac{1}{4}\left(\frac{\epsilon D d_L}{e d_{SL}}\right)^2 \frac{d^2 I_{DC}(V_{DC})}{dV^2}. \tag{2.23}$$

When this is approximation is justified for the devices used in this work will be further discussed in chapter 5.

2.2.4 The Potential for Acoustic Gain in the Semiconductor Superlattice

The previous section discussed a general theory of electron-phonon interaction in a superlattice device and did not look into the microscopic processes in detail. In this section a theory detailing a microscopic description of the electron-phonon interaction for specific cases will be detailed. This is important for an understanding of the results presented in chapter 4. In this theory, developed by Glavin et al. in 1999 [56], electron-phonon interactions within a SL may cause acoustic gain. After its initial development in 1999, the theory was then further developed with the effects of screening on the electron - phonon interaction [90] and finite length superlattices [91] being considered. More recently, a collaboration between theory and experiment in this area has led to the development of a model for gain in a SL including the effects of the level of disorder likely to be present in experimental devices, as explained in the work of Beardsley et al. [58].

SASER, Sound Amplification by Stimulated Emission of Radiation, in a SL is possible due to the creation of a population inversion from the point of view of phonon assisted electron transitions. This requires the electrons within the SL to be centred in individual wells and travelling through the structure using phonon assisted transitions. As explained in section 2.2.1, there are two separate models of transport in a SL which feature this, the

Wannier-Stark hopping model and the sequential tunnelling model. The original theory of gain within a SL was developed using phonon transitions as predicted by the Wannier-Stark hopping model [56], however in a more recent version of the theory the sequential tunnelling model is used [58]. This is more relevant for the results in this thesis where a weakly coupled SL is investigated.

The mechanism for population inversion between two neighbouring quantum wells in a SASER is shown pictorially in figure 2.7. This features a momentum space depiction of the two wells separated in energy by the application of an electric field to the structure. In the theory of gain in a superlattice structure, electron transitions within the quantum wells of the structure are taken to be fast. When this is the case the electrons within each well can reach thermal equilibrium and form a quasi-Fermi level [90], with states below this level populated and above empty. A phonon assisted transition will be indirect in space as indicated by the arrows in figure 2.7. In the figure the dashed arrows show possible phonon transitions for phonons with energy less than the energy separation of the quantum wells, and the solid arrows show transitions for phonons with energy greater. The purple lines indicate transitions which will be forbidden because they end in filled states, with the black showing allowed transitions. It can be seen that, for phonons with energy less than the well separation, transitions which emit a phonon, i.e. going from the higher well to the lower, are allowed and transitions which absorb a phonon, i.e. go from a lower well to a higher, are forbidden creating a population inversion. For phonons with an energy greater than the well separation the opposite is true.

These arguments for amplification are valid for phonons propagating at angles close to that of the superlattice growth direction. Phonons at larger angles are not amplified because intrawell relaxation processes will lead to the reabsorption of the emitted phonons. However, for small angle phonons energy and momentum conservation restricts intrawell processes [90].

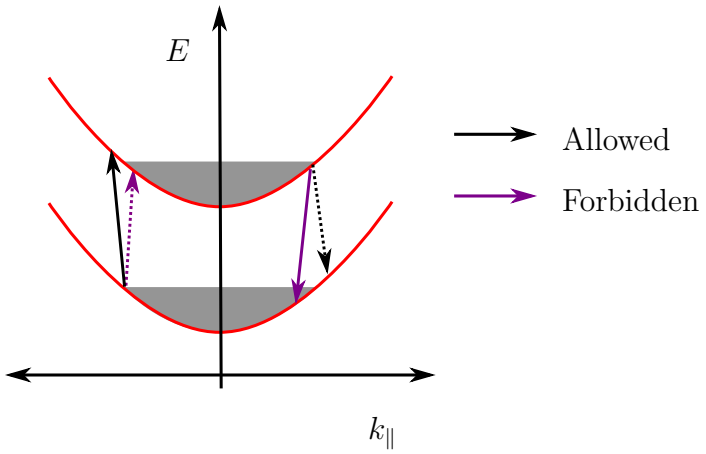

Figure 2.7: Diagram showing the mechanism of population inversion for phonon transitions between neighbouring quantum wells. The two parabolas show the electron subbands for neighbouring wells with the grey region indicating the filled states below the Fermi energy. The dashed arrows show possible phonon transitions for phonons with energy less than the energy separation of the quantum wells, and the solid arrows show transitions for phonons with energy greater.

Theoretical calculations of the gain possible in a SL structure involve the calculation of a phonon increment. This is defined as the difference between the probability of transitions between wells which involve phonon emission, $P^{(em)}$, and the probability of transitions between wells which involve phonon absorption, $P^{(ab)}$, as shown in equation 2.24.

$$\gamma_{\omega,q} = P^{(em)}_{\omega,q} - P^{(ab)}_{\omega,q} \tag{2.24}$$

In equation 2.24: γ is the increment; ω represents phonon angular frequency; and q is the phonon wavevector.

When the phonon increment defined in equation 2.24 exceeds losses in the system, gain will be possible. The increment has been found using probabilities for phonon transitions calculated within the Wannier-Stark hopping model [90] and within the sequential tunnelling model [58]. In both cases longitudinal acoustic phonons were considered and the main mechanism for electron-phonon interaction is the deformation potential.

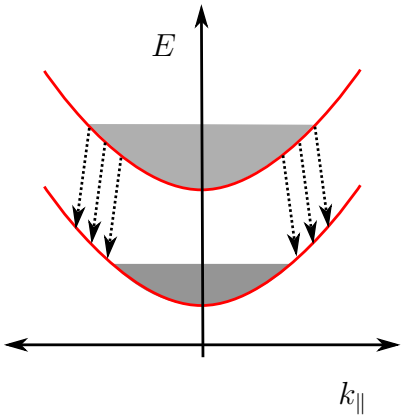

Figure 2.8: Diagram showing a potential mechanism for enhancement of population inversion for phonon transitions between a neighbouring quantum wells in the case of a disordered system. The two parabolas show the electron subbands for neighbouring wells with the grey region indicating the filled states below the Fermi energy. The dashed arrows show possible phonon transitions for phonons with energy less than the energy separation of the quantum wells.

In initial calculations of the phonon increment, population growths of up to 10^8 s^{-1} were predicted. This gain was predicted to be possible at a narrow range of Stark splitting values and it was predicted that the sign of the phonon population increment would become negative for $\hbar\omega > \Delta_S$, Δ_S representing the Stark splitting between the quantum wells induced by a bias and $\hbar\omega$ being the phonon energy. This is the behaviour which would be expected from the discussion of figure 2.7 given earlier. This behaviour was not seen experimentally, however an extension of the theory to include disorder predicted behaviour more in-line with experimental results [58].

Disorder was included in the structure by allowing for broadening of the energy levels in its QWs and spatial variation well and barrier widths through the device. The potential for gain in the device was found to be increased by these considerations. This was largely due to disorder causing a redistribution of electrons within the wells, meaning that in some cases the population inversion is increased as shown in figure 2.8.

Analysis of the variation of the phonon population increment in the case

of a disordered SL led to a different dependence on Stark splitting to that described above. It is still expected that the sign of the increment will change when $\hbar\omega = \Delta_S$. However a coefficient which arises due to the flucuations between different quantum well pairs determines the sign of the increment. The contribution of each quantum well pair to the phonon increment is dependent on the electron energy density mismatch. This is in contrast to the case of an ideal SL where the electron distribution in each well was equal and only the value of the Stark splitting between the wells was important. This allows the possible reversal of bias dependence, from the case presented in figure 2.7, ie. that amplification may be seen when $\hbar\omega > \Delta_S$. Also when the theory is extended to include disorder amplification is expected for a wider range of Stark splitting values than for the ideal SL theory, due to the broadening of the energy levels in the QWs. This theoretical description is more similar to the behaviour measured in the experimental structures.

2.3 Phonon Generation with an Aluminium film

In the experiments detailed in chapter 5 the excitation of an aluminium film by a femtosecond laser is used as a simple method of generating a coherent acoustic strain pulse. An understanding of the processes involved in this method of strain pulse generation will be beneficial for an understanding of the experimental method used to produce the results in that chapter. A macroscopic explanation for the processes occurring will therefore be given here. This will be sufficient to explain the results in this thesis, however a more detailed explanation of the microscopic processes can be found in works such as [28, 92, 93].

We will be considering the case of the excitation of an aluminium film by laser light which has been focussed to a spot of area A. In the previously described acoustic generation by a SL detailed in section 2.2.2, the laser

light was absorbed throughout the SL structure. In contrast at the near infra-red wavelengths used in these experiments an aluminium film is highly opaque meaning the fraction of the exciting laser light which is not reflected is absorbed in a short distance from the surface of the film, ζ. For this description it is presumed that this length is much smaller than the film thickness, d_F. The area of the laser spot is presumed to be much larger than both ζ and d_F. In the experiments detailed in this work, spot sizes of the order of $\approx$100 µm were used, compared to films of 30 nm to 100 nm and absorption lengths of a few nanometers, justifying these assumptions. Under such conditions, it can be assumed that the sound created will be longitudinal, and parameters such as temperature rise can be considered to be dependent only on the distance of the pulse from the surface [10].

The absorption of the energy of the laser pulse, E_F will cause a temperature rise which can be described by [3, 10]

$$\Delta T(z) = \frac{(1 - R_F)E_F}{c_F A \zeta} \exp\left(\frac{-z}{\zeta}\right), \tag{2.25}$$

here R_F is the reflection coefficient for light at the film surface, z is the growth direction of the film and c_F is the specific heat capacity per unit volume. This exponential temperature profile inside the film, sets up an isotropic stress given by equation 2.26.

$$\sigma = -3B_F\beta_F\Delta T(z) \tag{2.26}$$

In equation 2.26, B_F is the bulk modulus and β_F is the linear-expansion coefficient. The stress launches longitudinal acoustic waves in both directions in the film. The pulse which goes towards the surface will be reflected with a change of phase resulting in the bipolar nature of the strain pulse which leaves the aluminium film. If these were the only processes occurring in the film the width of the strain pulse would be purely defined by the absorption length of light within it, leading to a very sharp pulse for highly absorbing metals such as aluminium. However, the energy transferred by the laser to the film will not contribute directly to stress in the profile it was absorbed in the film. The

light is absorbed by the excitation of electrons in the metal, these electrons then diffuse into the metal while transferring their energy to the lattice. The diffusion results in a broadening of the profile of the strain pulse, which is dependent on both the thermal and electron diffusion lengths [10, 93].

Equation 2.27 represents the profile of a strain pulse excited by femtosecond optical excitation of a metal film. Equations 2.27 and 2.28 are taken from [41].

$$\epsilon = \frac{2A_F\zeta_F}{v_F\tau_e^2}(1-R_I)\sum_{j=0}^{j=\infty} R_I^j(t-\frac{(2j+1)d_F}{v_F})\exp\left[-\frac{(t-\frac{(2j+1)d_F}{v_F})^2}{\tau_e^2}\right] \quad (2.27)$$

where A_F is defined as shown in equation 2.28.

$$A_F = 3(1-R_F)\frac{QB_F\beta_F}{2c_F\zeta_F\rho_F v_F^2} \quad (2.28)$$

The various symbols used in this equation and the values used for calculations in this work are defined in table 2.1. An example of a strain pulse generated by this equation is shown in figure 2.9. In these equations the broadening of the strain pulse is included through the use of the value τ_e, rather than a temporal quantity directly representing the absorption length in the exponential term. The value of τ_e should therefore be set appropriately to include the effect of the electron and thermal diffusion in the film. These diffusion lengths are affected by electron scattering rates making τ_e a film dependent quantity. To account for this, it was used as a fitting parameter for strain simulations in this work.

In figure 2.9, at around 47 ps, the first strain pulse caused by the reflection of the strain at the Aluminium/GaAs interface is visible. Further such pulses will be present after the appropriate time intervals but, are not shown for clarity. The amplitude and sign of these reflections is determined by the reflection coefficient, R_I, in an ideal case this coefficient would be set by acoustic mismatch theory, as shown in equation 2.29.

$$R_I = \frac{Z_2 - Z_1}{Z_2 + Z_1} \quad (2.29)$$

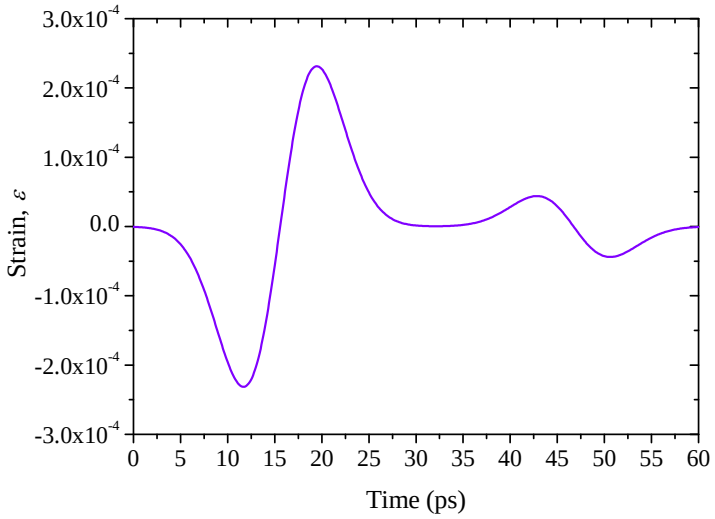

Figure 2.9: Example of strain pulse produced by equation 2.27 using values given in table 2.1, with $\tau_e = 5.5 \times 10^{-12}$, $d_F = 100\,\mathrm{nm}$ and $W = 10\,\mathrm{J\,m^{-2}}$.

Symbol	**Meaning in strain equations 2.28 & 2.27**	**Value appropriate for Aluminium film**
ζ_F	Absorption length of 800 nm light in the film	7.62 nm
v_F	Speed of longitudinal sound in the film	$6420\,\mathrm{m\,s^{-1}}$ [94]
R_I	Reflection coefficient for the interface between the film and the substrate	0.19, value from acoustic mismatch
Q	Fluence of the exciting laser	dependent on experiment
d_F	Thickness of film	dependent on experiment
B_F	Bulk modulus of the film	70.3 GPa [95]
β_F	Linear expansion coefficient	$23.1 \times 10^{-6}\,\mathrm{K^{-1}}$ [94]
c_F	Specific heat capacity per unit volume	$2.42 \times 10^{6}\,\mathrm{J\,m^{-3}\,K^{-1}}$ [94]
ρ_F	Density of the film	$2700\,\mathrm{kg\,m^{-3}}$ [94]
τ_e	Electron diffusion coefficient	dependent on experiment
R_F	Reflection coefficient of light at the surface of the film	0.87 [96]

Table 2.1: Table displaying values needed for a calculation of the strain magnitude, using equations 2.27 and 2.28.

In equation 2.29, Z_1 is the acoustic impedance of film and Z_2 is the acoustic impedance of the substrate. The main reason for the use of aluminium films in this work is that aluminium and GaAs, the substrate material used in these experiments, have similar acoustic impedances which results in a small R_I and minimal reflection at this interface.

Equation 2.29, presumes perfect coupling of the film at the substrate interface, however it has been shown that when the film is poorly bonded to the interface this equation should be modified [3, 97]. For instance in [97] a poorly bonded film is modelled as being attached to the sample surface by bonds which act in a similar manner to an array of springs and extra terms are added to 2.29 to account for the string constants of these bonds between the film and the substrate. The bonding of the film to an interface can have a significant effect on the spectrum of acoustic phonons it produces and will be further discussed in relation to the results of chapter 5.

Chapter 3

Experimental details

3.1 Introduction

This chapter will explain the general techniques used to perform the experiments described in the later chapters of this thesis. Initially details are given of the samples and the sample preparation techniques. After this some of the more specialised equipment is described. Finally details of the experimental techniques and optical arrangements required are provided.

3.2 Sample Processing

Several samples were used for the investigations which form the basis of this thesis. These all consisted of semiconductor structures featuring layers of AlAs, GaAs and AlGaAs at times with doping applied, these layers were grown by molecular beam epitaxy (MBE) either by Dr. Richard Campion using a *Vecco Mod Gen III* system or by Professor Mohammad Henini using a *Varian Gen II*, at the University of Nottingham.

The MBE technique involves using a heated source of the intended growth material to provide a flux of atoms onto a heated substrate. The raised temperature of the substrate gives the atoms the energy to move around and form epitaxial layers. To keep the sample pure and defect free the technique requires ultra high vacuums, below 10^{-10} mbar. MBE techniques are required for the structures used in this work due to the stringent requirements for sharp interfaces in the quantum well structures. The samples were grown on commercially produced GaAs substrates.

All of these wafers required some level of processing before they could be used in the experiments. For most of the samples this processing needed to allow the application of bias to parts of the sample structure. The formation of ohmic electrical contacts is required to achieve this. For this work the use of devices in the range of a few 100 µm diameter was suitable. The standard method to create devices of this size is ultraviolet(UV) photo-lithography. In this technique, areas of the sample are defined by the use of mask and photoresist. This allows large quantities of identical devices to be created. The features of these devices are comparable to the size of a speck of dust, meaning they can easily be ruined by any dust during the fabrication procedure. To prevent this, all the samples discussed in this thesis were processed in a cleanroom. The different devices created for these experiments had different specific processing requirements. The main processes used will be detailed first and then the specifics of the different samples will be discussed after.

3.2.1 Sample Preparation

The structures used in these experiments were grown on commercially prepared GaAs wafers with ≈50 mm diameter. To allow for the possibility of different experiments being performed on the same structure and also to make the samples a more convenient size for use in the cryostat, samples were processed in ≈5 mm squares. To achieve clean edges these squares were scribed from the wafer using a diamond tipped scribe and cleaved along crystallographic

planes. The samples were cleaned using 4 solvents before processing. The solvents were, in order of application, ethyl lactate, acetone, methanol, and isopropyl alcohol, the sample was soaked in each of these for 10 minutes while being sonicated in an ultrasonic bath. This removes any dirt or organic contamination which might be present. The samples were dried between these solvent cleans with nitrogen gas to prevent any staining from the solvent evaporation. The exception to this was the acetone stage when the samples are transferred between the acetone and methanol without drying to prevent the redeposition of material from the solvent to the sample. Between each processing step the samples were again cleaned in acetone, methanol and isopropyl alcohol, this prevents the recontamination of the surface at any point during the processing procedure. It is also a necessary step for the removal of resist at some stages.

3.2.2 Lapping and Polishing

Samples grown using the *Varian gen II* system were mounted within the MBE machine with indium which left a pitted back surface. This surface will strongly scatter acoustic phonons, so for any work which required generation of phonons on the back surface, polishing was required to smooth it.

To facilitate polishing the samples were mounted onto a metal disc mount using wax to protect the front side while polishing was taking place on the reverse side. During the polishing process this plate was mounted on a polishing jig, which allows the samples to be pushed into contact with lapping plates by the application of weights. To make sure the sample thinned uniformly it is important that the surface of the sample to be polished is level with the edge of the polishing jig. This is achieved using the optical alignment technique detailed in figure 3.1, which involves comparing a laser spot reflected off the sample with a spot reflected off an optical flat.

Once the sample is aligned on the jig it was then lapped on a 125 nm

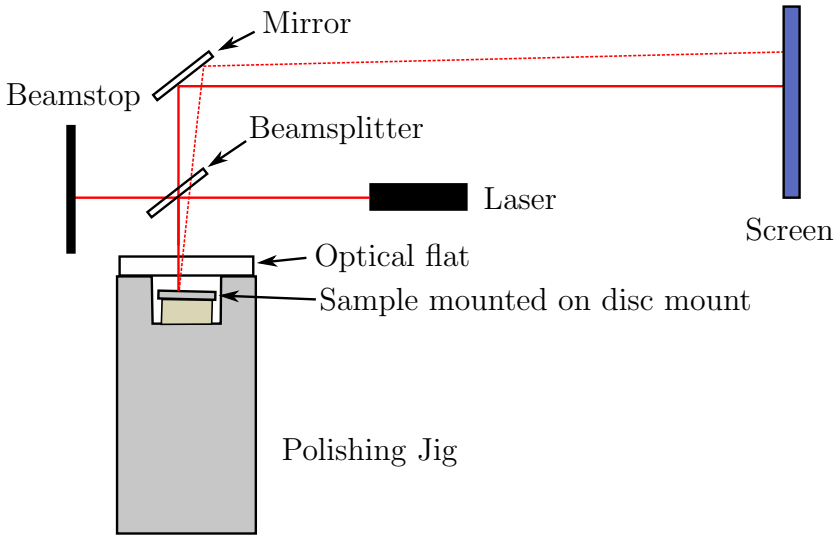

Figure 3.1: Optical arrangement used to level a sample in the polishing jig. Laser light is reflected off the sample and off an optical flat placed on the edge of the polishing jig, then directed to a screen which is placed approximately 3 m away. The sample, which is attached to a disc mount, can be adjusted to be parallel to the optical flat, at which point the reflected beam from the sample (shown as a dashed red line) and the reflected beam from the optical flat (solid red line) will be collinear and arrive at the same point on the screen.

diamond coated Syton lapping plate which thinned the sample through abrasion. Post lapping, the sample was then polished to achieve an optically flat finish to the surface using Logitex Chemlox polishing fluid, applied to a cloth lapping plate. This uses a chemomechanical process where the surface of the sample is removed by dissolution in an etching process which is moderated by mechanical means [98]. Samples contaminated with indium, which only needed a small amount of sample removed, were polished by rubbing the polishing jig over the lapping plates by hand in a figure of eight motion.

3.2.3 Patterning

Most of the processing used for the investigations in this thesis required the protection of certain regions of the sample from the action of the processing step. This was done using a positive photoresist. This is a chemical which becomes more soluble in a basic solution, known as the developer, after exposure to UV light [99]. The principle of patterning is therefore to expose the sample to a UV radiation source using a mask which has regions which need to be protected in the subsequent processes blocked out. Then sample can then be placed in the developer solution removing the desired areas of resist.

In this work the samples were patterned using BPRS150 positive photoresist. This was spun onto the samples at 4000 rpm to provide an even coat and the samples were then baked at 90 °C for 2 min on a hot plate. This step removes excess solvents and sets the resist. After this the samples were exposed to 6 s of UV radiation on a Karl Suss MJB 3 mask aligner. This included an Infra-red (IR) lamp and viewer enabling the alignment of devices on both sides of GaAs samples. GaAs being transparent to IR. A chrome mask was used to expose a pattern onto the sample and the resist was then developed in AZ 400K series positive resist developer.

Two different mask sets were used to produce the devices needed for this

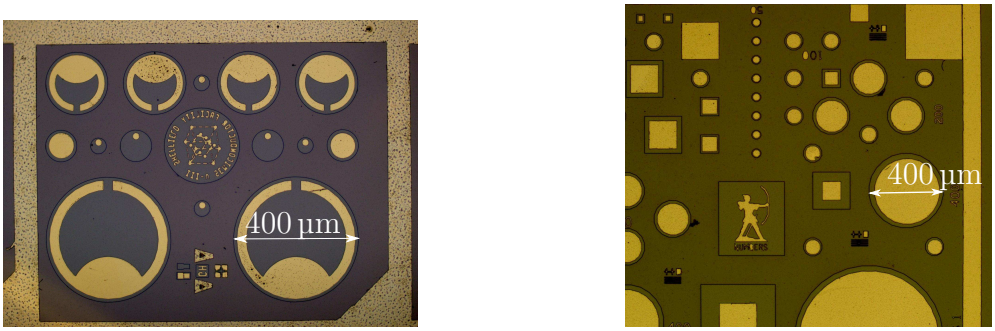

(a) (b)

Figure 3.2: (a) Optical access devices, patterned using the "Sheffield" mask. The mesas are the circular rings with either circular or horseshoe shaped gold top contacts, the square around the edge provides a ground contact.
(b) Devices without optical access, patterned using the "Robin Hood" mask. Square and circular mesas of various sizes are present surrounded by a large ground contact, the edge of which is visible to the right of the picture. The diameter/width of mesas in µm are shown in gold on the mask, one is also marked for clarity.

thesis depending on the requirements of the experiment. For experiments where optical access to the mesa was required the "Sheffield" mask was used, this is shown in figure 3.2a, this mask set includes separate masks for the upper and lower contacts meaning different metalizations can be used. When optical access was not required and it was possible to use the same metalization for both contacts the "Robin Hood" mask set can be used. This is shown in figure 3.2b and uses the same mask for the top and bottom contacts.

3.2.4 Wet etching

Etches were used to reach the lower layers of the structures such as the heavily doped contact layers, and to remove layers which were not necessary for experiments. In this work wet etching was used. This is where an acid or alkali solution is used to dissolve the unnecessary semiconductor material away. This is often used to create a mesa, a small area of the sample which is raised in comparison to the surrounding material.

Most GaAs etches involve the use of an oxidiser to form gallium and arsenic oxides on the surface and then the subsequent removal of these oxides by the acid or base involved [99]. The presence of resist will protect the areas of the sample covered, although when wet etches are used a level of undercutting is often seen. This is where the etch travels sideways as well as downwards leading to some attack of the area under the resist. This can be a problem when very precisely defined shapes are required. It is not an issue for this work where the size of the mesas is much greater than the etch depth.

In this work a solution of H_3PO_4:H_2O_2:H_2O was used as an etchant, including H_2O_2 as the oxidiser and H_3PO_4 to dissolve the material, the ratio 2:8:90 was used. This solution etches at a rate of $\approx 5\,\mathrm{nm\,s^{-1}}$. The etch rates can be varied by: the temperature of the solution, the doping of the material, the crystallographic direction of the material, the material composition and the level of agitation of the sample within the solution. Precise control of these factors is challenging to achieve and some of them will vary as the etch moves through the structure. To achieve an accurate etch depth despite these variations a KLA Tencor alpha step® D120 stylus profiler was used to measure the etch depth at several stages of the etching process, this allows an estimation of the etch rate throughout the structures.

In addition to being used for the creation of mesas, etches are also used to reveal defects on wafer structures [100]. This is due to the etch preferentially following the line of the defect causing pits to form. Certain etches are particularly useful for this purpose. Although the etches used in this work were not intended for this purpose their use did highlight issues which were eventually traced to a defected batch of substrates. These substrates had detrimental effects on the electrical properties of devices grown on them. Discovering the cause of these defective devices was important in the understanding of these experiments.

3.2.5 Contact formation

The bonding of a metal wire to the semiconductor device is necessary for its integration into a circuit. When a metal is deposited directly onto a semiconductor a barrier for electron transport is formed due to the bending of the energy bands required to align the Fermi energies in the metal and the semiconductor material. Such a situation is known as a Schottky barrier and will exhibit diode like behaviour [101]. This is not desirable for the devices used in this work where a low resistance contact is necessary. To create such a contact, known as an ohmic contact, a layer of a material which can act as a dopant to the semiconductor is deposited on the sample before the metal. The sample is then heated to allow this dopant material to diffuse into the semiconductor. Creating a heavily doped region increases the tunnelling through the Schottky barrier mentioned previously lowering the resistance of the contact.

To form low resistance contacts it is necessary for the surface to be very clean to prevent the formation of impurity layers which would be detrimental to the diffusion of the dopant into the contact. The samples were therefore initially three solvent cleaned as described in section 3.2.1, before being patterned as described in section 3.2.3. After patterning an oxide etch was performed. This was achieved by submerging the sample in 1:1 H_2O:HCl for 60 s. This step is thought to lower the resistance of the contacts by removing the native oxide which may interfere with the diffusing layer [99].

The deposition of the contact itself is done using a thermal evaporation technique. In this process the sample and the sources of material to be deposited are placed in a chamber which is pumped down to pressures in the 10^{-7} mbar range. The high vacuum decreases the risk of contamination during the process. The material sources are then heated via a current placed through a refractory metal boat until the point the source material starts to evaporate. The rate of evaporation is monitored via the vibration caused to a quartz crystal which gives a measurement of the flux of material incident

on it. The current through the boat is varied to achieve a stable evaporation rate and then a shutter is opened allowing the metal to be deposited on the sample. The shutter is closed again when the desired layer thickness is achieved. This coats the whole sample in metal. The previous patterning of the sample will have left resist on the area which should be kept free of metal. The excess metal is removed by soaking the sample in warm acetone, this removes the resist and the coating metal layers from this area. In this work evaporations took place in either an Edwards E306A coating system or an Edwards Auto Turbo evaporator, depending on availability.

There are various recipes for contacts to GaAs, some of which include layers to help control the diffusion process as well as those which form the dopant layer itself [99]. In this work, contacts to n-doped semiconductor layers were created using either the layer structures InGe:Au or Ge:Au:Ni:Au. For the InGe contacts, 40 nm of InGe mixed to be 1:1 by weight is used for the dopant layer and 100 nm Au as a capping layer. Whereas for Ge:Au:Ni:Au contacts 60 nm of Ge and Au were used followed by 30 nm Ni with a 150 nm Au capping layer. Here the Ge is the dopant and the nickel layer is used to control the diffusion. Ohmic contacts to p-doped semiconductors were made using 20 nm of Mg with 120 nm Au as a capping layer.

After the evaporation of the metal layers the samples were annealed to allow the diffusion of the metal into the semiconductor. This is done in a rapid thermal annealer (RTA) which provides a stable source of high temperatures. An ANEALSYS AS-One Rapid Thermal Processing Furnace was used for this work. To prevent the oxidation of the contacts during the heating, the samples are placed in a chamber which was purged using a vacuum pump and an inert process gas, specifically for the samples in used in this thesis a mixture of H_2 and Argon was used. The rapid heating in the RTA is provided by a series of heat lamps. To ensure that this heat is transferred efficiently to the samples they are positioned within a graphite susceptor plate. The temperature can be monitored by a combination of a pyrometer and a thermocouple attached to the plate. The samples were heated to temperatures of between 350 °C to

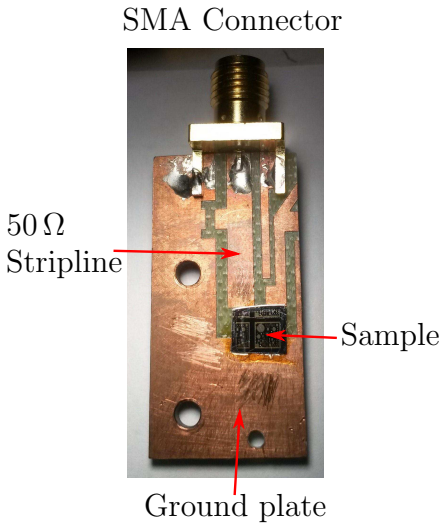

Figure 3.3: Picture of sample holder.

440 °C depending on the contact layers and the sample.

When the devices were completed they were attached to circuits boards with GE/IMI 7031 Varnish, which is an insulating glue capable of withstanding the large temperature changes the samples are subjected to during cryogenic experiments. Figure 3.3 shows a sample on its holder. The devices on the samples were connected to the holder using aluminium wire, enabling the application of bias through the SMA connector shown in figure 3.3. The wires were attached to the sample and the copper plating of the holder using a wedge bonder. A wedge bonder includes a wedge shaped needle and a microscope allowing the precise placement of the wire and then uses an ultrasonic pulse to fuse the wire to the sample surface.

3.3 Sample Structures

There were some design features and considerations which are common to all the samples featured in this work, these will be detailed here, before specifics of different structures are discussed in later sections. The samples were all

grown using combinations of GaAs, AlAs and AlGaAs on GaAs substrates. This is because these materials all have similar lattice constants preventing the formation of strain within the structures. Also GaAs is a direct bandgap semiconductor, with high electron mobility making it ideal for the creation of devices requiring good optical and electronic properties.

The contact layers in all structures were doped to $10^{18}\,\mathrm{cm}^{-3}$. This level of doping aids in the formation of ohmic contacts to these layers and helps to provide a uniform electric field within them. The aim of this work was to study electron-phonon interactions in semiconductors making the design of semiconductor superlattices in these samples an important part of this thesis. When designing SLs for phonon experiments there are two main considerations: what laser wavelength will excite phonon emission from the structure and what the frequency of that emission will be. Section 2.2.2 discusses these properties. SLs emit phonons when excited by a wavelength which corresponds to a laser energy of greater than the electron-heavyhole transition of the quantum wells within the SL [20] [22]. This means that the laser energy at which a SL is excited can be tailored to different experiments by altering the width of its quantum wells. The frequency of the phonons emitted is defined by the period of the SL and again this can be tailored for specific experiments.

3.3.1 MN796

The layer structure of the sample MN796 which was used the majority of the experiments detailed in this thesis is shown in figure 3.4. This sample was designed as a coherent phonon optics chip allowing the coherent measurement of the effect of the application of bias to a structure on the phonons generated in a separate structure. To achieve this a single-pass amplification structure featuring two superlattices was grown on one side and a *p-i-n* photodiode detector was grown on the opposite side of the substrate.

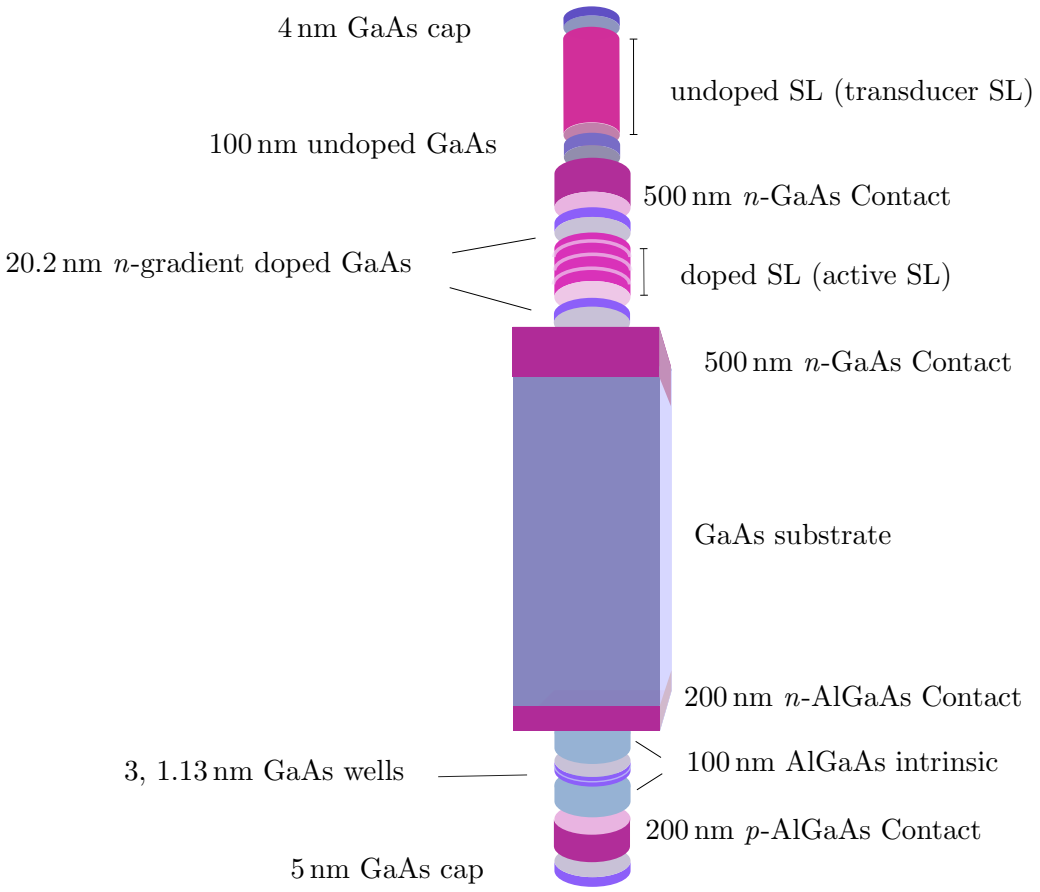

Figure 3.4: Layer structure of wafer MN796, not to scale, layers shown expanded for clarity. All contact layers are doped to $10^{18}\,\mathrm{cm}^{-3}$, n-type contact layers are silicon doped while p-type contact layers are carbon doped. All AlGaAs layers feature 33% Aluminium. In the active SL the doping level in the 5.9 nm quantum wells is $1 \times 10^{17}\,\mathrm{cm}^{-3}$, while in the 3.9 nm barriers the doping level is $2 \times 10^{17}\,\mathrm{cm}^{-3}$. The transducer SL features 4 nm quantum wells and 11 nm barriers. There are some buffer layers between the substrate and the active device. These are required for a high quality MBE growth but do not have a significant effect on the experiment so are not detailed here.

The requirements of this experiment for the upper superlattice (SL) were that it can be excited by laser wavelengths of ≈700 nm and emit longitudinal acoustic phonons with a frequency of between 300 GHz to 400 GHz. It was found that a quantum well width of 4 nm and a SL period of 15 nm would achieve this. The 100 nm undoped spacer layer is included to screen this SL from the effects of applying a bias to the doped SL below it.

The lower SL structure was grown to the specifications used in a previous work, which had been shown to be capable of producing the amplification of longitudinal acoustic phonons [102]. 500 nm contact layers, which are n-doped to levels of $10^{18}\,\mathrm{cm}^{-3}$ with Si, were grown either side of the SL. The highly doped contacts are separated from the lower doped SL region by a 20.2 nm gradiently doped GaAs spacer. This is to shield the SL from the highly doped contact while ensuring there are no insulating layers which might cause a capacitive effect in the device. The SL itself is n-doped to $2 \times 10^{17}\,\mathrm{cm}^{-3}$ in the barriers and $1 \times 10^{17}\,\mathrm{cm}^{-3}$ in the wells, this level of doping was chosen to provide high levels of carriers to take part in the amplification process. This will be further discussed in subsequent chapters. The well width used in this structure was 5.9 nm and the barrier was 3.9 nm these values were chosen because they had been shown to be capable of producing amplification in previous SL devices [102]. For a discussion of the difference between weakly and strongly coupled SLs see section 3.11.

The p-i-n photodiode detector structure was designed to be activated by the same wavelength as the upper SL in the single-pass amplification structure just described. An appropriate energy separation was found to be present in 1.25 nm GaAs quantum wells. To create an easily measurable photocurrent with such a small quantum well, the active area in the detector featured 3 wells. The contact regions in this device were also doped to $10^{18}\,\mathrm{cm}^{-3}$, for the same reasons as stated earlier. The n-doping was achieved using Si while the p-doping was performed with C. All layers around the quantum well in this device were grown from AlGaAs to ensure that when the energy of the laser was tuned for absorption in the quantum well the rest of the device will

be transparent.

For the photocurrent *pump-probe* experiments detailed in chapter 4 it was necessary to be able to apply a bias and excited with the laser on both sides of the sample. To do this the "Sheffield" mask shown in figure 3.2a was processed on both sides of the sample. 400 µm mesas were used on the SL side and 200 µm mesas were used on the photodiode side. The *p-i-n* photodiode is most sensitive to signals incident parallel to its growth direction, this means the mesas on opposite sides of the substrate needed to be aligned opposite each other, this was achieved using the IR viewer on the mask aligner described in section 3.2.3.

As can be seen in figure 3.4, on the SL side of the sample the upper contact is below the top SL. To reach this contact and still leave an area of the SL for optical excitation, the etch to the top contact layer was performed in the contact area of the mask, leaving the top SL present in the optical access area of the mesa.

3.3.2 Samples Investigated in Chapter 5

Several samples were used for the electrical detection experiments described in chapter 5. The samples used in these experiments had predominantly been grown for previous experiments but contained a SL with properties of interest for the study. This means that in some cases they contained layers other than the electrically contacted SL which was the subject of the investigation. To avoid potential complications only the properties of the superlattices themselves and the thickness of the substrate will be listed here, as other layers will not have any effect on these experiments. One sample was grown for these experiments, RC04, this control sample was grown to the same dimensions as the active SL structure MN796, but with an n-doped GaAs layer in the place of the active SL .

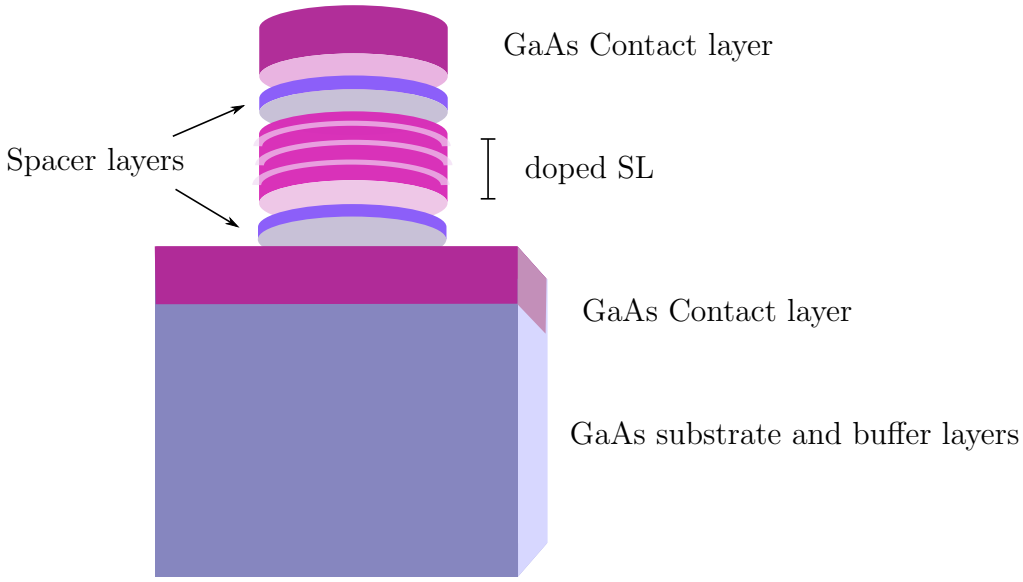

Figure 3.5: General SL layer profile present in all samples investigated in chapter 5, not to scale, layers shown expanded for clarity. All GaAs contacts were n doped with Si to $2 \times 10^{18}\,\mathrm{cm}^{-3}$.

The samples were all grown by MBE and featured the general SL layer structure shown in figure 3.5. Sample NU2299 featured GaAs wells and $Al_{0.7}Ga_{0.3}As$ barriers while all other samples had GaAs wells and AlAs barriers. The spacer layers in sample NU2299 were 30 nm $Al_{0.97}Ga_{0.03}As$ with doping of $1.4 \times 10^{16}\,\mathrm{cm}^{-3}$. All other samples featured spacer layers of 20.2 nm GaAs with a doping which varied between that of the contacts and that of the superlattice through the spacer. The SLs were all n doped with Si. The top contact in NU2299 was 600 nm and the lower 1000 nm. All other samples had two contact layers of 500 nm. Samples NU2299 and NU1778 were grown using an indium mounting process, where the back of the wafer is secured in the MBE chamber using melted indium metal, these samples required polishing, as detailed in section 3.2.2, before use in the experiments. Other samples were secured using clips. Sample NU2299 was grown on an n^+-substrate, all others were grown on semi-insulating substrates. The properties of the SLs in these samples and the substrate thicknesses, which were the attributes important for the experiments performed on them in this thesis are listed in table 3.1.

Sample	NU2299	MN796	MN685	NU1778
Substrate (µm)	262	164	373	227
Well thickness (nm)	10	5.9	5.9	5.9
Barrier thickness (nm)	2.5	3.9	3.9	3.9
Number of periods	15	50	50	10
Doping in SL (cm^{-3})	10^{16}	10^{17}	10^{17}	10^{16}

Table 3.1: Table displaying properties of SLs used in electrical detection experiments

The samples were processed using the "Robin Hood" mask set shown in figure 3.2b, and the methods outlined in section 3.2. Any excess layers on the samples were removed by wet etching as detailed in section 3.2.4. It should be noted that in the case of MN796 and MN685 although the contact layers were grown to 500 nm only ≈250 nm will be left above the SL after this etching.

It was necessary to evaporate an aluminium film transducer on the back of the samples for the experiment detailed in chapter 5, this was done using a thermal evaporation technique in the manner described in section 3.2.5.

3.4 Lasers

Two laser systems were used in this work: a high power amplified system and a oscillator system. The amplified system is capable of achieving pump powers of the order of mJs; while the oscillator system generates pump powers of nJs with a higher repetition rate. A Fabry-Pérot cavity was also used to allow the creation of a pulse train with a tunable frequency from the output of the amplified laser, this will also be discussed here.

3.4.1 Oscillator

The oscillator laser system consists of a mode locked Ti:Sapphire tsunami laser cavity by Spectra-Physics. This is pumped by a Millenia Xs Nd:YVO_4 diode laser also produced by Spectra-Physics. Ti:Sapphire is a solid state laser medium frequently used in research applications because of its high thermal stability and tunability [103]. The laser used in these experiments was capable of operation in the wavelength range 690 nm to 1080 nm and produces pulses of widths between 80 fs to 130 fs while operating at 82 MHz.

The wavelength is tuned by the use of a prism and slit arrangement. The prisms spatially separate the different wavelengths in the beam enabling the slit to select the one required. The pulse width is tuned using prisms which alter the net group velocity dispersion of the beam. It is possible to achieve a quasi-continuous wave output of this system by turning off the active mode locker and misaligning these components.

3.4.2 Amplifier

A Spectra-Physics Spitfire Pro F regenerative amplifier was used to provide the higher power required for some of the experiments performed in this thesis. The amplifier uses a Ti:Sapphire gain medium, in this case it is used to amplify a seed pulse from a mode locked Ti:Sapphire tsunami oscillator, similar to that described in section 3.4.1. The regenerative amplifier can amplify the seed of this laser from nanojoules up to millijoules of energy. This system also has a lower repetition rate, operating at 5 kHz rather than the 82 MHz of the oscillator.

The amplifier uses chirped pulse amplification. In this process a pulse from the oscillator is broadened and the passed several times through the Ti:Sapphire gain medium, which is pumped by a frequency doubled Nd:YLF laser, in this case a Spectra-Physics Empower 15 was used. This amplifies

the pulse, which is then compressed resulting in a short pulse of increased amplitude. It is necessary to broaden the pulse to prevent damage to the Ti:Sapphire crystal by decreasing its peak power. The pulse expansion and compression are both done by diffraction gratings within the amplifier. This relies on the relatively broadband nature of the Ti:Sapphire output, which provides different wavelengths within the pulse, the path lengths of these can separately be altered enabling the expansion or compression of the pulse. This process is not compatible with the wavelength selection used in the oscillator system described in the previous section. The output of this laser is therefore permanently centred at 800 nm.

The reduced frequency of the pulse train is necessary for the high amplitudes to be achieved, enabling the gain from the amplifier crystal to be concentrated in fewer pulses. This is achieved by only allowing some of the pulses from the seed laser into the gain medium. This reduced output frequency means the amplifier system is not capable of such high modulation frequencies or as extensive averaging as the oscillator system, signals taken using this system are therefore more prone to noise. However, there are some phenomena which can only be seen with excitation at powers achieved by the amplification process.

3.4.3 Fabry-Pérot Cavity

The Fabry-Pérot cavity is used to produce a quasi-monochromatic acoustic wave through a technique developed by Choi et al. [104]. A schematic of the operation of the Fabry-Pérot cavity used in the experiments detailed in this thesis is shown in figure 3.6. The purpose of the cavity is to create a train of pulses separated by an equal distance. This is achieved by using a pair of partially reflective mirrors. The laser beam will be reflected back and forth in this cavity with a percentage of the beam released at each mirror, this results in a series of pulses separated by twice the mirror spacing.

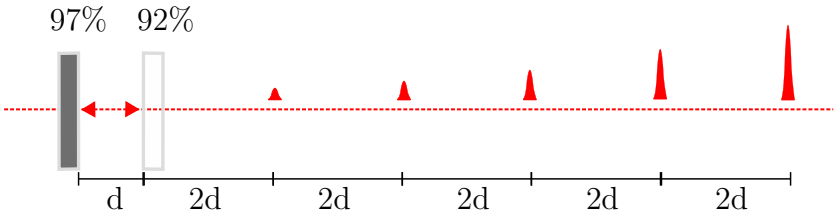

Figure 3.6: Schematic of Fabry-Perot cavity. Two partially reflective mirrors are used to create a pulse train. In this case 92% and 97% reflective mirrors are used.

As can be seen in figure 3.6 the cavity is formed by 92% and 97% reflectance mirrors. To allow precise control of the separation of between the two mirrors the 92% mirror was mounted on a delay stage. This allows easy adjustment of the mirror separation, leading to a change in the pulse separation and hence in the train frequency. The delay stage allowed this change to be controlled precisely, to a level of 0.1 µm, however a systematic error in the frequency readings will be present if there is any error in the separation of these mirrors when the stage is at zero. This will have a much larger effect on the higher frequency settings, because any error will be a bigger percentage of the small spacing required for the creation of high frequencies. To avoid scratching the mirrors by pushing them together the mirrors were initially separated by a spacer at zero, however it was discovered that this could lead to errors when zeroing the mirrors, so the technique was adjusted. The new technique involved moving the mirrors together until a diffraction pattern appeared in the unfocussed laser spot. This will occur when the mirror separation reaches the distance corresponding to the travel time of one laser pulse width, a value which can be measured from an auto-correlator included in the optical arrangement. This enables a precise calibration of the zero of the stage when high frequency pulse trains are required. The mirrors are aligned to be precisely parallel to the beam path so that all the pulses arrive at exactly the same point on the sample where they are focused on the transducer film generating a series of acoustic pulses, with a temporal separation defined by the time it takes light to travel twice the separation of the mirrors.

In the initial work of Choi et al. [104] a novel retroreflector known as the

deathstar compact was used to create a Gaussian profile in the amplitude of these pulses. In this work this additional complexity was avoided and the amplitude of the pulses simply decays exponentially.

As discussed in section 2.3 the strain generated by laser excitation of a transducer film incorporates a broad spectrum of frequencies, centred on a value related to the film thickness. The spectral content of the pulse train created by the Fabry-Pérot cavity is strongly dependent on this as will now be discussed.

Spectral content of Fabry-Pérot cavity output.

Figure 3.7 shows an example of a simulation of a bipolar strain pulse such as is generated by the optical excitation of a 30 nm film, not including any acoustic reflections present in the film. The strain seen here was simulated using equation 3.1, which is a simplified version of equation 2.27 which was introduced to describe the strain generated in an aluminium film in section 2.3.

$$\epsilon(t) \sim (t - t_f) \exp\left[-\left(\frac{t - t_f}{\tau_e}\right)^2\right] \tag{3.1}$$

Here ϵ is the strain, t is time, t_f is the time of flight for phonons in the aluminium film and τ_e is a parameter which defines the width of the strain pulse. The amplitude of this equation was normalised to one for simplicity in these calculations.

As was described in section 2.3, the width of the strain pulse is related to both the absorption length of light in the film and to the thermal and electron diffusion lengths within the sample [92], [93]. In equation 3.1 the parameter τ_e is used to represent these processes. For the 30 nm film shown in figure 3.7a it is presumed that the pulse width is limited by the film thickness and the width is therefore set as the time of flight through this film, 4.67 ps, using 6420 m s^{-1} as the speed of longitudinal sound in aluminium [94]. This width

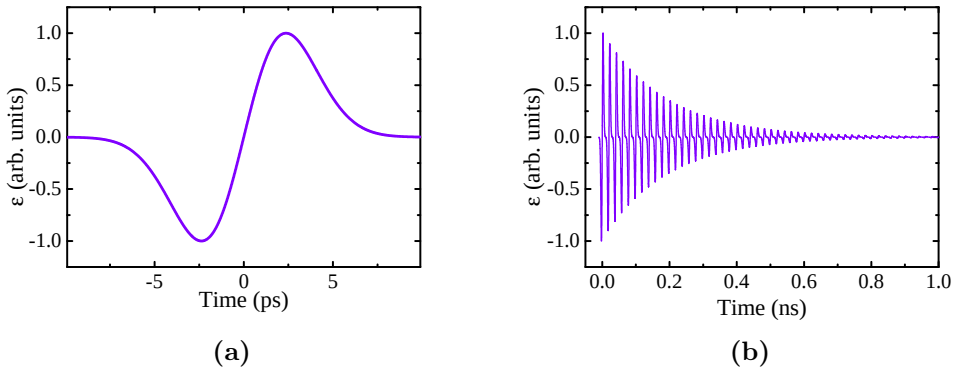

Figure 3.7: (a) A simulation of the acoustic strain pulse expected when a 30 nm aluminium film is is excited by a femtosecond laser pulse.
(b) A simulation of the strain expected when a 30 nm aluminium film is excited by a 50 GHz laser pulse train

is achieved using a value of 3.3 ps for τ_e in equation 3.1.

Figure 3.7b shows the expected output the transducer film when excited by a pulse train from the Fabry-Pérot cavity set at a spacing of 3 mm, which corresponds to a frequency of 50 GHz. It was measured that the reflectances of the mirrors in the cavity correspond to a decay of 0.11 between pulses, which is what is shown here. In figure 3.8 the power spectral density of pulse trains at various frequencies are shown. These are obtained from Fast Fourier Transforms (FFT) of the pulse trains in a 5 ns window, which is long enough that the pulse trains have decayed to negligible levels. In figure 3.8a this is shown for pulse trains generated using strain pulses with $\tau_e = 3.35$ ps, while 3.8b shows the same thing when a value of 6.3 ps is used for τ_e.

In both the figures shown in 3.8, it can be seen that at low frequencies many spectral lines are present, including several harmonics of the frequency corresponding to the train spacing. As the train frequency is increased the number of harmonics seen decreases and eventually at higher frequencies the power seen in the frequency the mirror separation corresponds to starts to decrease. Comparing the power spectra at 10 GHz in graphs seen in figure 3.8;

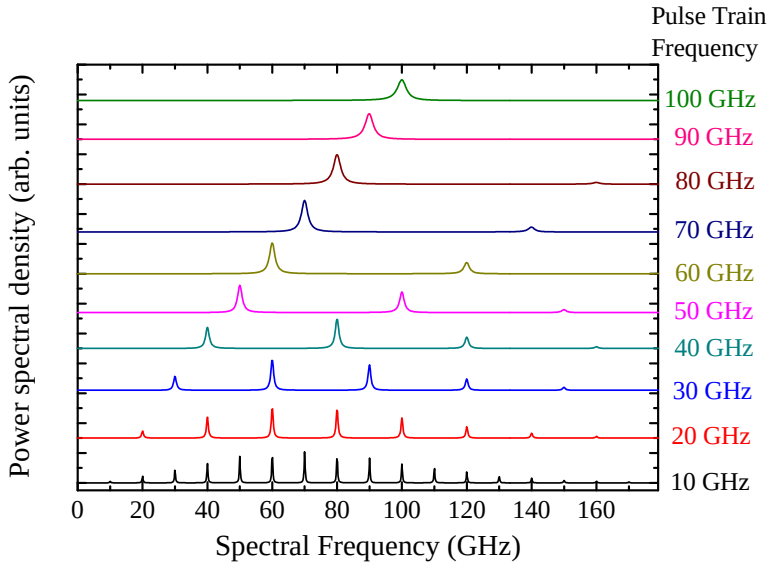

(a) $\tau_e = 3.35\,\text{ps}$

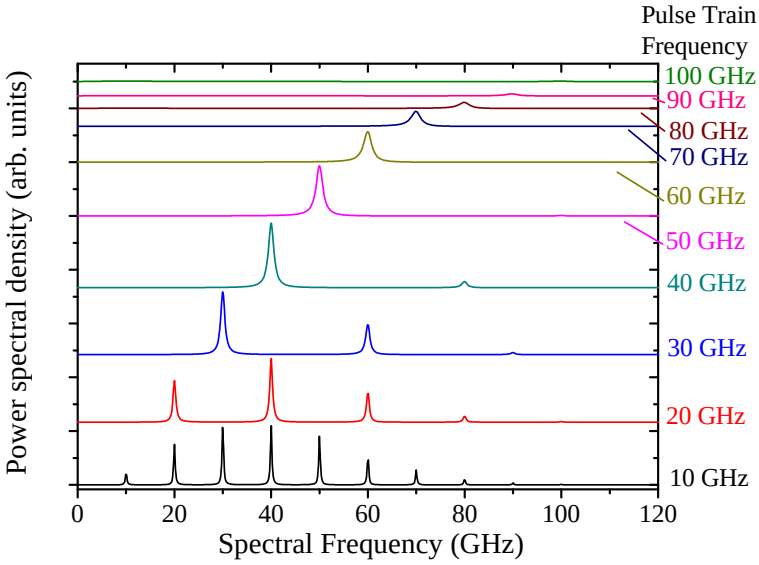

(b) $\tau_e = 6.30\,\text{ps}$

Figure 3.8: Spectra of the simulated acoustic response to optical excitation of aluminium films using the FP cavity at different frequencies. These were found by performing a FFT of the acoustic pulse train in a 5 ns window. (a) shows the spectra using a strain pulse with $\tau_e = 3.35\,\text{ps}$. (b) shows the spectra obtained when a value of $\tau_e = 6.30\,\text{ps}$ was used.

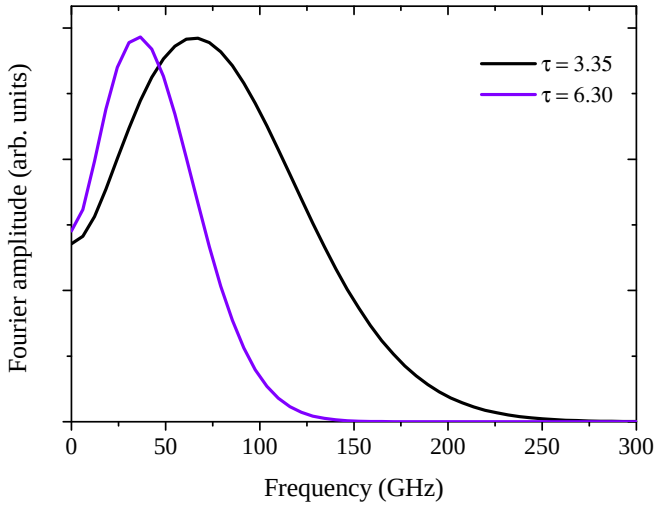

Figure 3.9: FFT of the simulated bipolar strain pulses for the two values of τ_e used to simulate the pulse trains in figure 3.8.

it can be seen that in figure 3.8a maximum spectral frequencies of ≈160 GHz are achieved, while in 3.8b the maximum frequencies seen are only ≈90 GHz.

Figure 3.9 shows the FFT of the simulated bipolar strain pulse shown in 3.7a and also the FFT of the equivalent strain pulse for a value of $\tau_e = 6.3$ ps. Comparing this to the spectra of the pulse trains in 3.8 shows how the output of the pulse trains is defined within an envelope of the frequencies present within the single pulse. This is particularly obvious at the low frequencies when many harmonics are present. The sharper pulse with the lower τ_e value contains higher frequencies, as is expected from standard Fourier theory. This means higher frequencies are possible in the pulse train and more harmonics are seen in the lower frequency trains, as previously stated. τ_e is defined by, both the absorption length of light in the film, and the amount of electron diffusion occurring within the film [92]. This electron diffusion is related to the film thickness but can also be influenced by the defect scattering which may be film dependent. The appropriate value of τ_e for some of the films used in the experiments performed in this work will be further discussed in relation to the experimental results, in section 5.3.6.

As can be seen in figure 3.8, there is a limited frequency range at which the excitation from the pulse trains can be said to be monochromatic and this range is related to the specific transducer film. This is a consideration for some aspects of the experiments performed with this cavity and will be further discussed as relevant.

Figure 3.10 shows the hypersonic energy of the pulse trains as a function of train frequency. This was calculated by integrating the entire acoustic spectrum, 0 THz to 50 THz, at each train frequency. The two values of τ_e which have been considered so far, are both shown. In figure 3.10 it can be seen that the energy in the pulse trains starts to decrease at 38 GHz, when τ_e = 6.3 ps, and at 74 GHz, when τ_e = 3.35 ps. This decrease in energy of the train is caused by the pulses beginning to interfere destructively as the spacing in the pulse train becomes less than the pulse widths. The link between this and τ_e is therefore unsurprising. Figure 3.10 also shows how the energy of the train reaches a minimum at 102 GHz and 192 GHz, for τ_e = 6.3 ps and 3.35 ps respectively, after this point it then begins to increase for both curves. This is due to the overlap of the multiple pulses reaching a point where they form a single pulse, then as the frequency is further increased this leads to more pulses being incorporated within this pulse increasing its amplitude.

The energy in the pulse train as a function of frequency will be investigated experimentally for several films within this work. The method used in the simulations above will be used to investigate the film parameters, as will be further discussed.

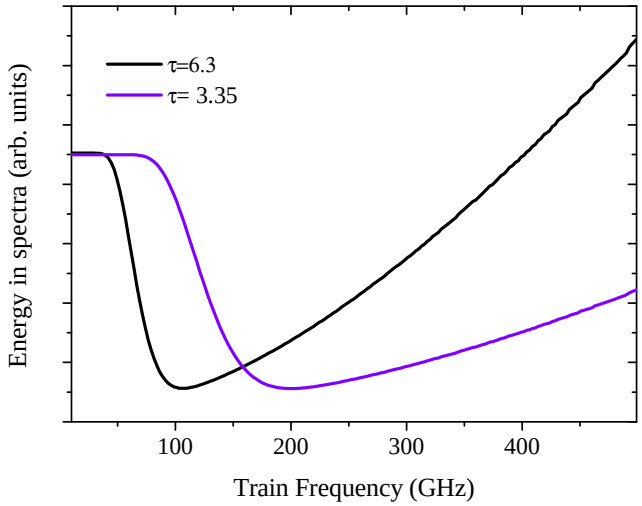

Figure 3.10: Hypersonic energy as a function of pulse train frequency. This was found by integrating the pulse train other the entire spectrum, 0 THz to 50 THz.

3.5 Cryostats

For the majority of the experiments described in this thesis it was necessary to keep the samples at low temperatures. This was for a variety of reasons such as to prevent the attenuation of high frequency phonons as they move through the substrate, to lessen the background noise from thermal phonons and to prevent thermal broadening of energy levels within the heterostructures. Two styles of cryostat were used for these experiments which will be briefly described here.

3.5.1 Bath Cryostat

An Oxford instruments Optistat^{TM} bath cryostat was used for many of the experiments detailed here. In this cryostat helium is transferred directly into a bath within the cryostat. This is thermally shielded from the environment

by both a vacuum and a liquid nitrogen shield, to prevent excessive boil off.

In this cryostat the sample is in a chamber surrounded by helium vapour. The Helium vapour is pulled into the sample space from the bath using a vacuum pump. Through a combination of controlling the pressure exerted by this pump and the use of an electric heater the sample space can be maintained at a stable temperature. Although the cryostat is capable of reaching temperatures of 1.5 K, 10 K was often sufficient for the experiments detailed here.

3.5.2 Flow Cryostat

An Oxford instruments Flow cryostat was also used. In this case the helium is not transferred into the cryostat, but instead is continuously transferred from a dewar by pumping with a vacuum pump. The sample is not in the helium vapour in this cryostat. The helium is thermally coupled to the sample through a conductive heat exchanger. A Oxford instruments temperature control unit is used to control the output of a heater enabling the variation of the temperature.

3.6 Reflection *pump-probe*

The *pump-probe* experiment is a popular technique for the observation of the evolution of material properties with time. As such there are several variations on the technique, a more detailed discussion of this can be found elsewhere, for instance [105]. The main principle of the *pump-probe* experiment is that the laser is split into two components a stronger, pump component, and a weaker, probe component. The pump component is used to create a change in the material and the probe beam is used to monitor how this change evolves over time. This can be done by changing optical path of either the pump or

probe beam, to make the probe pulse arrive at the sample at a later time than the pump pulse. By recording signals at regular time intervals throughout this movement a series of snap shots of the evolution of the process excited by the pump can be obtained. Using highly accurate stepper motor controlled delay stages and laser pulses of femtosecond duration enables a femtosecond time resolution to be obtained in these experiments.

Since its development in the 80s [10] the technique of reflection *pump-probe* has been extensively used to study phonons in a variety of materials. The rapid heating of the sample by the pump beam leads to the generation of a thermal stress which causes the emission of coherent acoustic phonons. These can be detected by the reflection of the probe beam off the surface of the sample. The optical properties of the sample are effected by the presence of the phonons leading to changes in the sample reflectivity.

The experimental arrangement used for reflection *pump-probe* experiments in this work is shown in figure 3.11. These experiments were performed using the oscillator laser described in section 3.4.1. The beam is split into a pump and probe path by a 90:10 beam splitter. The pump beam is then sent into a retroreflector mounted on a motorised delay stage. This has a travel path of 600 mm corresponding to an optical delay of 4 ns. Putting the delay in the pump path means that any changes in beam position caused by the delay will only result in changes in the beam intensity seen by the probe. This is preferable to the possibility of seeing inhomogeneities in the sample if the probe position were to drift.

After the motorised delay stage, the beam is sent into a fast scanning delay stage (shaker). This is a retroreflector on a spring loaded mount which can oscillate back and forth in the beam path. Multiple averages of a relatively small time window can be obtained using this. The shaker was often set to measure a 55 ps time window at 2.5 Hz. The timing of the window compared to the probe pulse is set by the position of the motorised delay stage which is stationary when the shaker is in use.

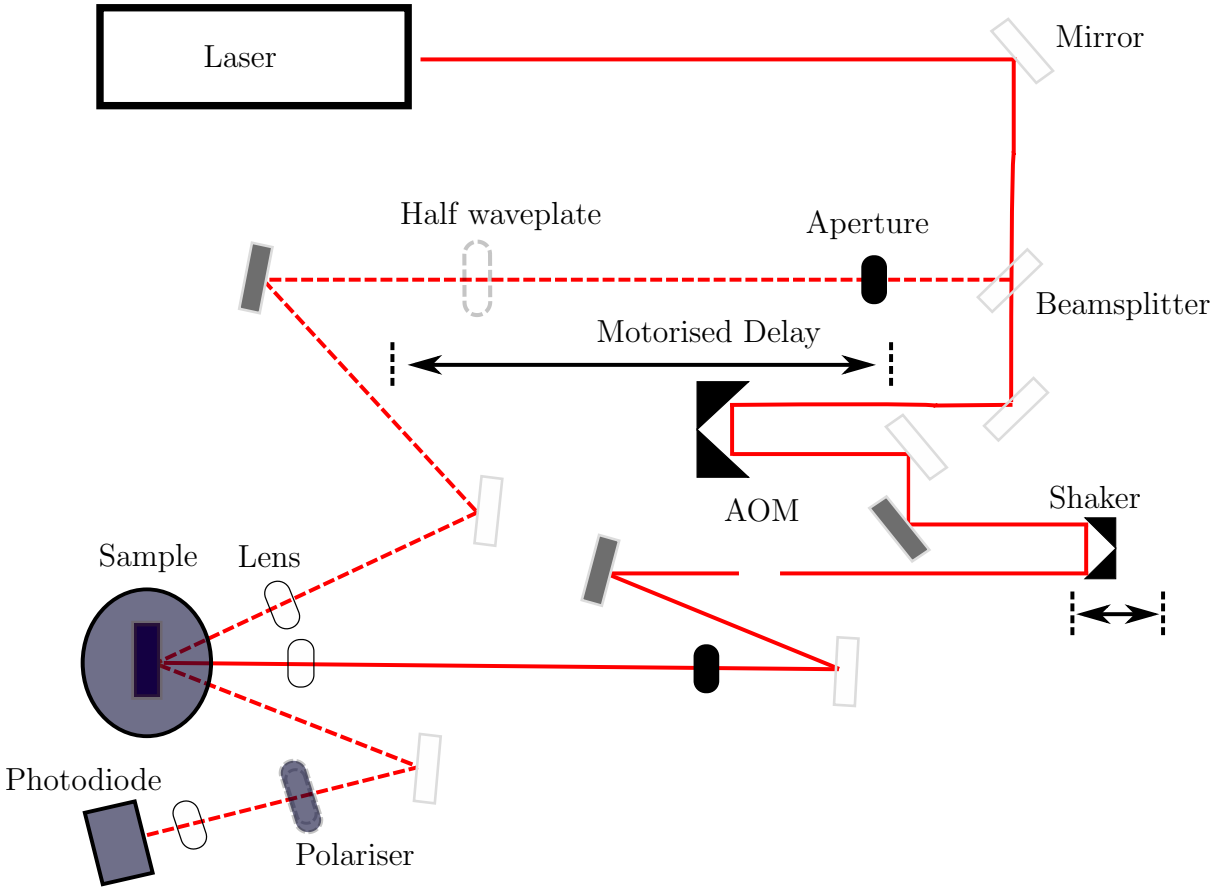

Figure 3.11: Optical arrangement used for reflection *pump-probe* experiments in this work. The pump beam path is shown by a solid line and the probe by a dashed line.

The changes seen in the probe beam are very small compared to the size of the reflected signal, so a lock-in amplifier is used to measure them. An acousto-optic modulator (AOM) is used to modulate the pump beam, for reflection *pump-probe* experiments this modulation generally takes place at frequencies of ≈100 kHz. The frequency used to modulate the pump beam is then used as a reference to the lock-in amplifier. An aperture is used to block the beam which is not deflected by the AOM. The pump beam is then focused on the sample to a spot size of ≈100 µm.

The sample is placed in the bath cryostat, described in section 3.5.1, for these measurements and maintained at a temperature of 10 K. These temperatures sharpen the optical resonances in the sample and lessen the noise from background phonons.

The probe path does not feature any motorised delay stages and is set to a path length such that the path of the pump and the probe beam are equal within the movement of the delay stage. An aperture is used to block any extra beams present after the beamsplitter. The probe beam is polarised and after the reflection of the probe beam off the sample a polarising filter is used to block all the light which is not at the same polarisation the probe beam was set to. This helps to stop any scattered pump light affecting the probe signal.

A camera is focused on the sample and the image on a screen is used to align the probe and pump laser spots together together. The probe beam is focussed to ≈50 µm, a smaller spot than the pump, this makes it less sensitive to any movements of the pump beam that may occur, for instance as the timing between the two is altered.

Finally, after its reflection off the sample, the probe beam is focussed into a photodiode, the output of which is directed into the lock-in amplifier to extract the changes related to the pump pulse. This experimental procedure can achieve sensitivities which enable the measurement of changes in the relative reflectivity of the probe beam with magnitudes of 10^{-7}.

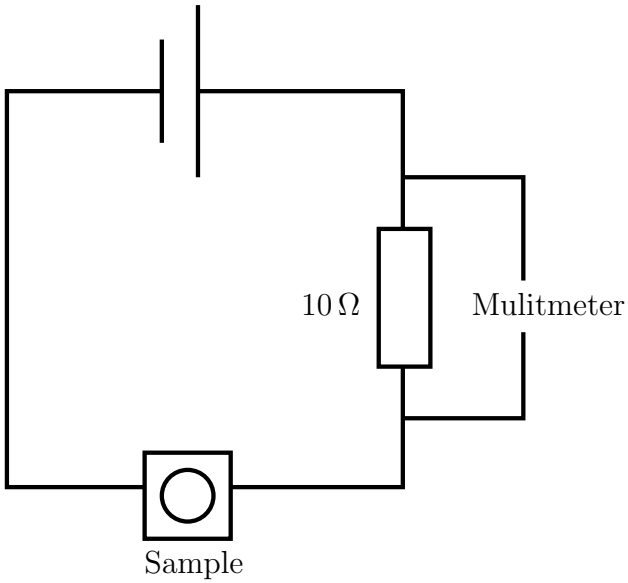

Figure 3.12: Schematic of circuit used for *I-V* measurements

3.7 *I-V* measurements

DC *I-V* measurements were performed to characterise the transport properties of the electrical devices used in these experiments. These give information such as the device resistance and which transport regime it is operating in. There were two methods used for these measurements during this work. The method chosen depended on the availability of equipment and which experimental arrangement was required for subsequent experiments. Either, the whole measurement was undertaken using a Keithly 2400 sourcemeter, or the circuit shown in figure 3.12 was used and a Keithly 230 programmable voltage source was used to provide voltage while a Agilent 43301A Multimeter was used to monitor the current by measuring the voltage over a 10 Ω resistor. These experiments can be performed at different temperatures using the cryostats described in section 3.5.

3.8 Photocurrent Measurements

Laser excitation of semiconductor samples creates carriers which, with the application of bias, leads to the generation of a photocurrent. This can be used to get information about the quality of the optical resonances in the sample. This is important in the characterisation of the *p-i-n* photodiode detector devices as will be discussed in the next section.

The *I-V* set up described in section 3.7 can be used to make measurements of the variation of the photocurrent with bias in the device. When these measurements were made on the samples investigated in this thesis the oscillator laser described in section 3.4.1 was adjusted to operate in continuous wave mode. When the laser operates in this mode it emits a narrower energy pulse giving a better estimation of the wavelength dependence of the current generated.

3.9 *p-i-n* Photodiode Detector

A *p-i-n* photodiode can be used as a sensitive coherent detector of acoustic waves, providing a detection sensitivity of up to 1000× that of traditional *pump-probe* techniques [29]. The investigation detailed in chapter 4 makes use of a *p-i-n* photodiode detector, so details of their operation will be given here. The main principle of a measurement of strain with a *p-i-n* photodiode is to monitor changes in the photocurrent generated in the device as the strain pulse travels through.

The *p-i-n* photodiode is formed of *p* and *n*-doped semiconductor layers separated by an intrinsic region. This functions in the same way as a standard *p-n* diode [101], with the intrinsic region acting like an extended depletion zone. The device can be made sensitive to strain by the inclusion of a quantum well (QW) in the intrinsic region. For use as a detector the device is operated

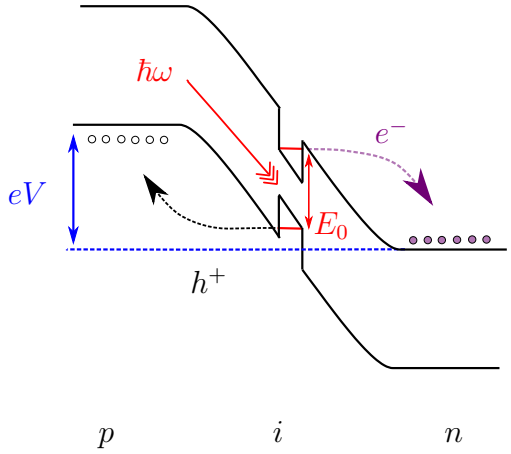

Figure 3.13: Schematic of photocurrent generation in a *p-i-n* photodiode incorporating a QW in the intrinsic region. In the diagram V is the potential present across the device, e represents the electrons, h represents the holes, E_0 represents the separation of the energy levels in the QW and $\hbar\omega$ represents the photon energy.

under reverse bias, at which point it does not conduct current. It is then illuminated with laser light tuned to a wavelength which will be absorbed in the QW. When it is absorbed within the well the light creates carriers which are swept to the contacts by the electric field in the device creating a photocurrent. This is shown in figure 3.13.

The absorption of light within the QW exhibits a sharp resonance when the energy of the light matches the exciton resonance of the well. An exciton is formed when an electron and hole are coupled through the coulomb interaction acting like a hydrogen particle with the hole acting as the nucleus. The masses of the constituents of this hydrogen like particle are determined by the effective masses in the appropriate energy bands. The probability of absorbing light then becomes equal to the probability of creating this particle. This is a particularly strong transition when the particle created would correspond to the 1S state of the hydrogen atom. For this state the probability of creating the particle is related to the proximity of the hole and electron to each other, which is enhanced by confinement in a QW [106]. This sharp transition contributes to the high sensitivity of the device.

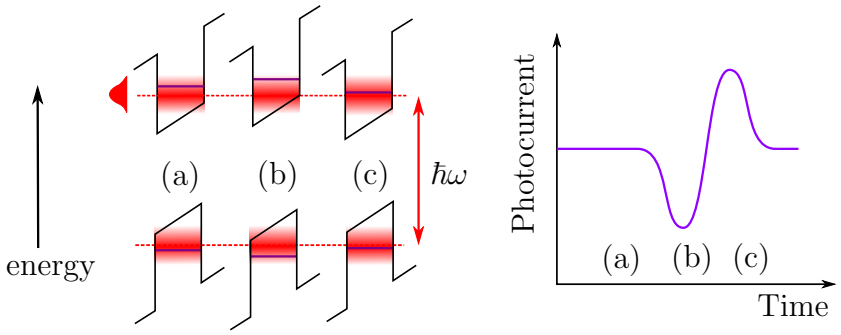

Figure 3.14: Schematic to demonstrate how the *p-i-n* device detects strain. The figure on the left demonstrates the processes in the QW, while the figure on the right demonstrates the photocurrent generated. The red represents the laser energy and the purple line represents the energy level in the well. In both figures processes labelled (a) represent no strain, (b) represent compressive strain and (c) represent rarefaction.

When a strain wave passes through the quantum well it causes causes a change in its energy levels. If the device is being excited by light at this point these changes can tune or detune the QW from resonance with the laser energy leading to strong changes in the photocurrent generated. This is depicted in figure 3.14. An investigation into the main causes the strain induced shifts in the QW found the dominant effect, in similar samples to the ones used in this investigation, was to due to the deformation potential [29]. To achieve the highest detection sensitivity, the device is tuned so the maximum of the laser energy is slightly smaller than the QW energy gap when no strain is present. In this case there will be some photocurrent generated in the device but not the maximum amount possible. A compressive strain moves the energy levels within the well further from the maximum of the laser energy, this will lead to a reduction of the photocurrent in the device, whereas a rarefaction moves the energy levels closer, causing more photocurent.

The operation of the device can be optimised at different wavelengths by adjusting the level of bias applied to the *p-i-n* diode. This can cause shifts in the exciton resonance of the QW by a value in the order of 10 meV. These large shifts are possible due to a process known as the quantum confined Stark effect, which is caused by the confinement of the exciton in the QW

which preventing it from being ionised. The Stark shifts can then be seen due to the effect of the applied field on the exciton [106]. Using this effect the detector can operate at a range of wavelengths around 20 nm from its optimum. However, as larger biases are applied the exciton peak is broadened and the device will start to lose sensitivity. This means that width of the QW in the device needs to be chosen to give an appropriate energy gap for the required wavelength of operation. The potential wavelengths of operation for each device can be tested using the photocurrent measurements detailed in section 3.8.

The width of the quantum well is also a consideration with regards to the frequency requirements of the detector. When the wavelength of the phonon incident on the detector is shorter than the width of the quantum well it is possible for both tension and rarefaction to be present within the well which will lead to the signal being averaged out. Narrower QWs therefore provide better sensitivity to high frequency waves.

3.10 Photocurrent *pump-probe*

Photocurrent *pump-probe* experiments were performed using a *p-i-n* photodiode as the detector for the investigation detailed in chapter 4. These experiments required a *pump-probe* arrangement, using the the oscillator laser described in section 3.4.1. The use of a *p-i-n* in this arrangement, in combination with a femtosecond laser provides a coherent high sensitivity detection system. Generating the photocurrent in the device with a femtosecond pulsed laser allows fast gating of the detection system. Combining this with high accuracy delay stages allows signals to be recorded with femtosecond resolution.

The optical arrangement used for these photocurrent *pump-probe* experiments is shown in figure 3.15. It can be seen in this figure that the main

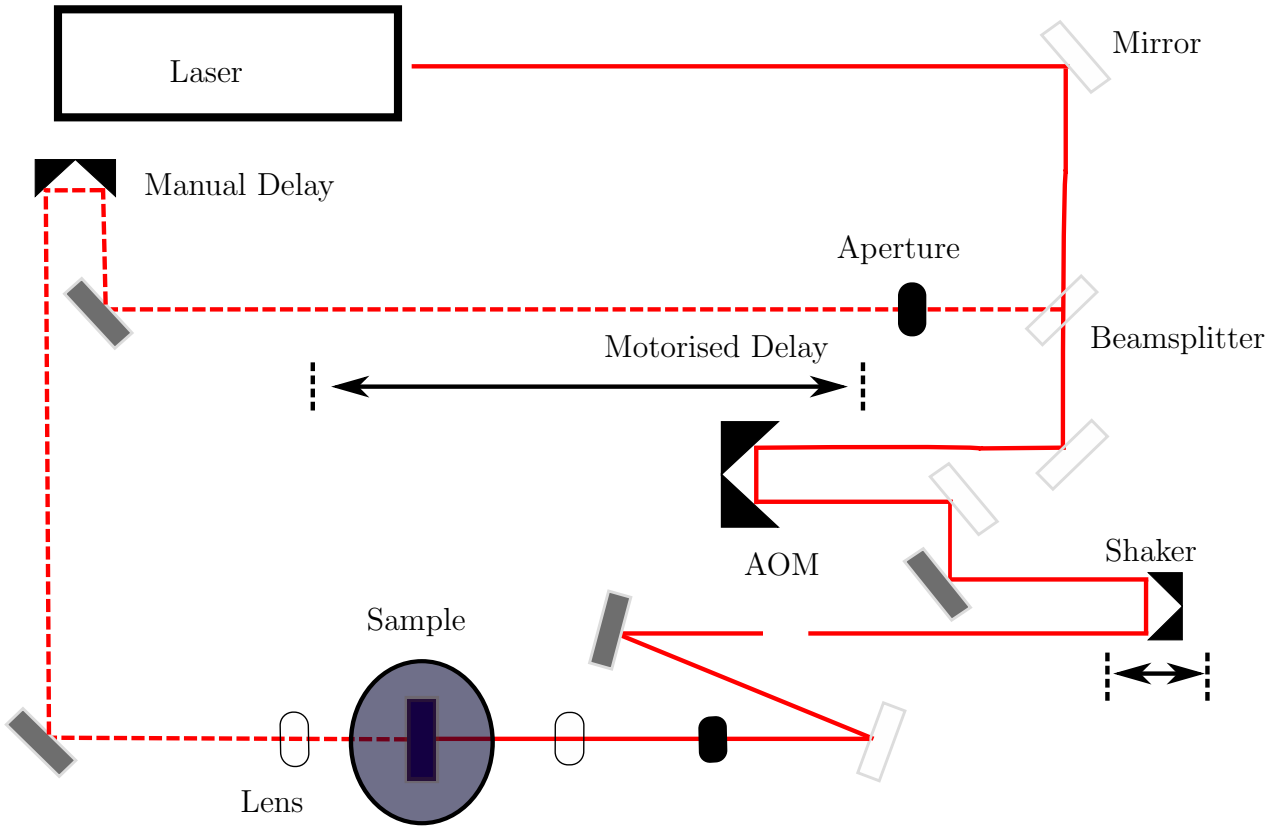

Figure 3.15: Schematic of the optical arrangement used for photocurrent *pump-probe* experiments as detailed in chapter 4. The pump beam path is shown by a solid line and the probe by a dashed line.

difference between this experiment and the reflection *pump-probe* arrangement detailed in section 3.6 is that this experiment requires the pump and probe laser beams to be incident on opposite sides of the sample. Also, the probe beam does not need to be polarised in this experiment because the electrical detection used is not sensitive to optical noise from the pump.

The motorised delay stage and the shaker are used in these experiments in the same way as in the reflection *pump-probe* arrangement described in section 3.6. The pump and probe beam are focussed either side of the sample with a tighter focus on the probe, again as described in section 3.6. A camera is used to align the probe spot on the p-i-n detector, and a luminescence signal which can be seen from the pump spot through the substrate is used to align it opposite.

When the phonon signal is generated on the opposite side of the substrate to that it is detected on extra time has to be allowed between the pump and probe pulses to enable the signal to pass through the substrate. The path lengths required to achieve this delay either use lots of space or multiple reflections which, even with the use of high quality mirrors, would inevitably lower the beam power. Since this experiment is performed with the oscillator laser described in section 3.4.1 it is possible to utilise the high repetition rate of the laser to lower the path length requirements. Time delays corresponding to multiples of the 12.5 ns time separation between the laser pulses can be achieved simply by using a later pulse to probe. The optical delay provided by the laser path then only needs to cover the remainder left when the time required is divided by 12.5 ns. A manual delay stage is included in the probe beam for ease of fine tuning of the probe path to match this condition.

The AOM can be used in the same manner as described in section 3.6, however, in addition, it was necessary in the experiments detailed in chapter 4 to investigate the effect on the signal detected of applying a bias in the generating structure. To achieve this, a bias modulation technique was used. Here the AOM was set to a continuous wave mode where it provides a

continuously deflected beam. The bias to the SL device was modulated and the frequency of this modulation used as a reference to the lock-in. This allows the difference between the signal seen in the sample with and without bias to be extracted enabling small changes caused by bias to be isolated.

In these experiments the sample is kept at 10 K by use of the same bath cryostat described in section 3.5.1. The low temperatures are particularly important in experiments where the signal has to travel through the substrate to prevent the attenuation of the hundreds of gigahertz phonon pulse.

3.11 Microwave Electrical Detection

In the experiments detailed in chapter 5 the electrical output of a sample was monitored while a strain wave was passing through an electrical device present on the sample. This was used to monitor the changes in the electrical properties of the sample as the strain passes through in real time, as opposed to a *pump-probe* experiment where the evolution of the signal over time is built up as a series points at separate times. To achieve this microwave frequency electronics are required. Cabling with a maximum frequency rating of 18 GHz was used with amplifiers rated at 14 GHz. The signal was recorded by a Tektronix DPO 71254 digital oscilloscope rated at 12.5 GHz. The circuit used for these measurements is shown in figure 3.16. DC biases are applied to the device using a bias tee which separates the DC and AC parts of the circuit, this is rated to 12 GHz.

The strain was generated opposite the device by the optical excitation of an aluminium transducer film. This film was evaporated on the back of the substrate using the evaporation techniques described in section 3.2.5, which were used to create the metal layers for ohmic contacts. The excitation of the film was performed using the amplified laser described in section 3.4.2. The optics used for these experiments are as shown in figure 3.17. A glass blank is

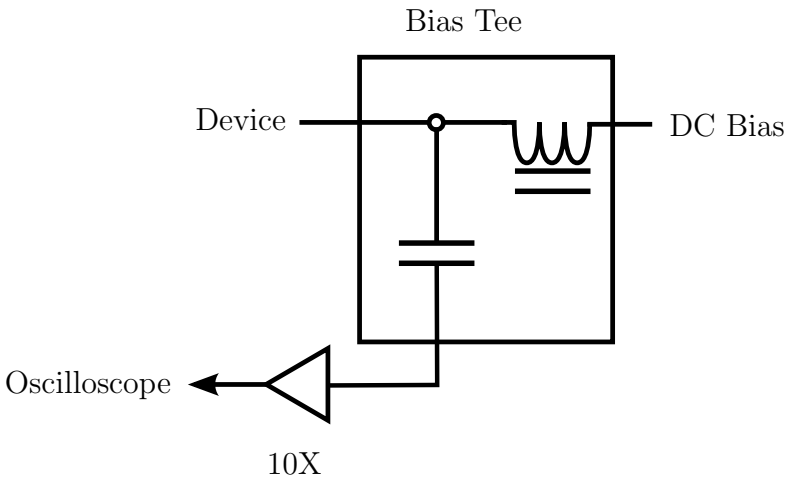

Figure 3.16: Diagram of circuit used for electrical detection.

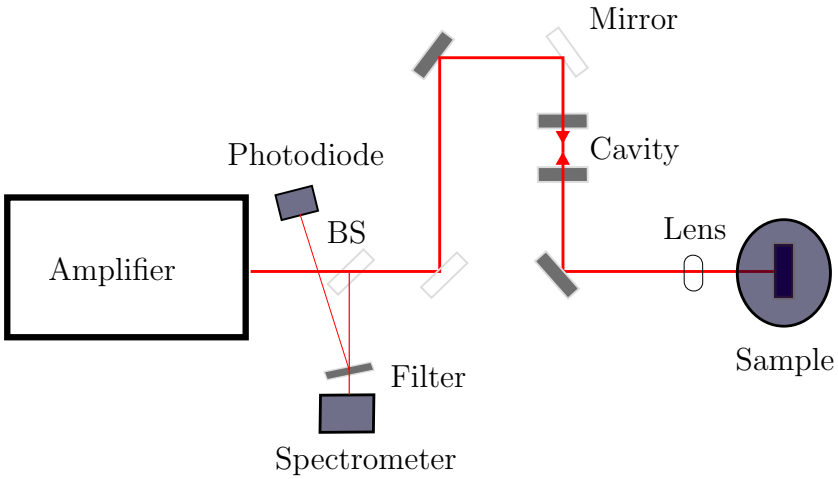

Figure 3.17: Schematic of optical arrangement used to produce strain pulses for electrical detection. BS here stands for beamsplitter.

used as a low power beamsplitter to separate off a small section of the beam which is sent to an autocorrelator. This is used to monitor the width of the laser pulse. An even smaller section of the beam is sent to a photodiode by means of a back reflection off a filter. The pulse measured on this photodiode is used to trigger the oscilloscope measuring the electrical signal. For some of these experiments it was necessary to use a Fabry-Pérot cavity, the operation of this was described in section 3.4.3. Some extra mirrors are included to allow alignment of this cavity and the beam is then focused on the transducer film, with a spot size of $\approx$150 µm. A camera was focussed on the device side of the sample and the laser beam hotting the other side was aligned opposite the device by looking at the spot seen through the sample. The sample was kept at $\approx$5 K by use of the flow cryostat described in section 3.5.2, this prevents the attenuation of the phonons as they move through the substrate.

Chapter 4

Coherent Phonon Optics using an Electrically Controlled Device

4.1 Introduction

Phonon optics, the study of the interaction of phonons with matter, has shown the potential for applications in areas such as high-frequency electronics [48, 49], information technology [107, 108], biosciences [109, 110], and medical diagnostics [8, 111]. Much previous work has concentrated on the generation of THz sound through the optical excitation of semiconductor superlattices [18, 82]. Traditionally these phonons are detected by monitoring changes they cause to the reflection of a laser at the surface of a sample in *pump-probe* experiments [15, 23]. Generation by this method requires a high-power pulsed laser system, limiting the applications to the lab, while this detection method has limited sensitivity [24].

Previous work has identified a potential source of THz phonons through the development of the electrical properties of semiconductor superlattices (SLs) to create a saser device. This device would allow the electrical control

of the amplitude of a phonon beam. This negates the need for complex laser systems so would increase the portability of applications.

Previous work, both theoretically [58, 91] and experimentally [59, 60], has shown evidence that the amplification of sub-THz acoustic phonons can occur in these devices. Experimentally these devices have been studied incoherently through a bolometric detection method, and through the coherent reflection *pump-probe* method. Both of these methods provide limited information about the operation of the device. It is hoped that a high sensitivity coherent detection method would improve our understanding of the processes occurring in a saser structure and enable further development. Such a detector has recently been developed using a *p-i-n* photodiode [29]. This device can be used in a *pump-probe* experiment to achieve coherent detection of acoustic waves with high spatial and temporal resolution.

The work presented in this chapter details an experiment combining a potential saser structure with a *p-i-n* photodiode detector, giving rise to a coherent phonon lab on a chip. The structure allows a separate source and detector to be used to test a potential active phonon device. A schematic of the experiment is shown in figure 4.1. MBE growth techniques were used to produce a single-pass active SL structure on one side of a 164 µm substrate and a *p-i-n* photodiode detector on the other. The single-pass structure incorporates two SLs, an upper one grown to be an efficient phonon transducer and a lower one which was grown according to saser specifications. The two SLs are grown with different periods so they feature different phonon stop gaps. This prevents confinement of the phonons generated in the transducer in the active device, allowing the investigation of the effects of a single-pass through the active medium. The optical excitation allows the device to be phase locked to the *p-i-n* detector, allowing coherent detection in a pump-probe configuration.

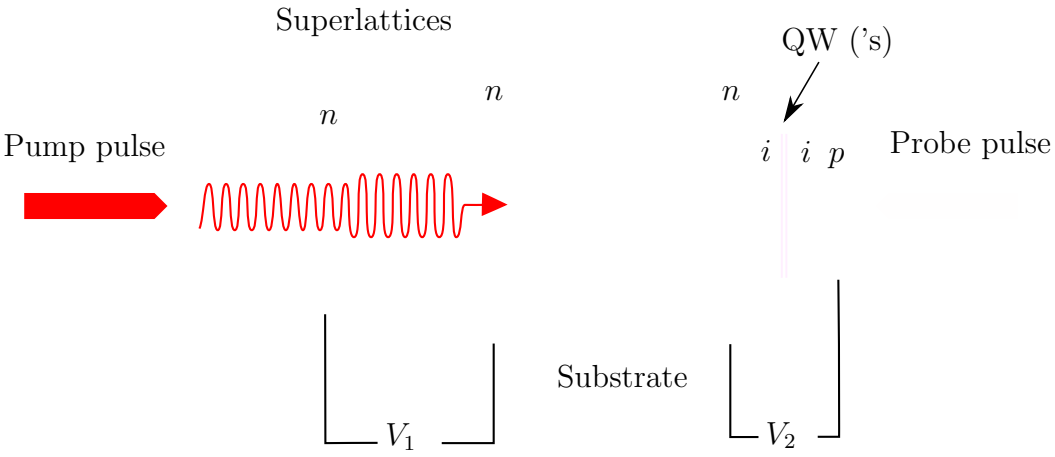

Figure 4.1: Schematic of the photocurrent *pump-probe* experiment. A pump laser pulse is used to excite a phonon signal in the top SL, this then passes through the active SL where it is possible to apply a bias. The phonon pulse then propagates across the substrate to the *p-i-n* detector, which is activated by a time delayed probe pulse. This gives a high temporal resolution reading of the phonon signal within the quantum well of this device. Any effects caused by the bias on the phonon signal passing through the lower SL may be investigated.

4.2 Device Characterisation

These experiments were performed on the wafer MN796. Details of the structures grown on this wafer and the processing they required are given in section 3.3.1.

The nature of this experiment requires the creation of two separate devices on opposite sides of the wafer. These had to be characterised in separate experiments, which will be separately described here. The characterisation experiments were performed at 10 K. This temperature is used throughout these experiments because it limits the attenuation of high frequency sound as it travels through the substrate and prevents thermal broadening of the energy levels in the structure.

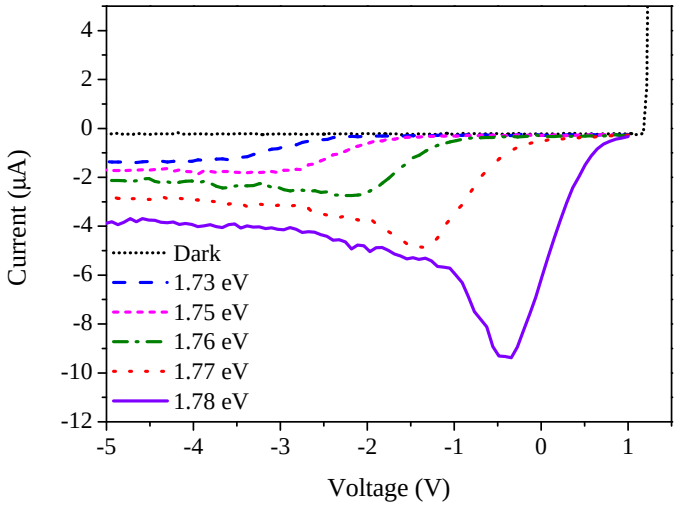

Figure 4.2: *I-V* measurements of the MN796 *p-i-n* device when illuminated by continuous-wave laser light at several laser energies and also in the dark. The laser fluence at all energies was set to 2.3 μJ cm^{-2}.

4.2.1 *p-i-n* Photodiode Detector

To characterise the *p-i-n* photodiode detector, its sensitivity and the wavelength dependence of its sensitivity should be determined. A photocurrent experiment was used to ascertain this information. This was performed as detailed in section 3.8.

Although several devices were used in the experiments presented in this chapter, only one set of photocurrent measurements will be presented here. When different devices are processed from the same wafer there is a chance of variation, despite the apparently identical structure, due to unavoidable processing inconsistencies or growth inhomogeneity across the wafer; this is discussed further in section 5.3.1. However, the differences seen between the different *p-i-n* devices used was small enough to be insignificant to the results of these experiments.

Figure 4.2 shows the *I-V* characteristics of the devices when in the dark

and when illuminated with 5 differing photon energies. In the dark, the device shows the expected diode characteristics with a forward turn on of ≈1 V and minimal current in reverse bias, until a breakdown occurs at ≈−6 V.

When a *p-i-n* device is illuminated with laser light it is possible to generate a photocurrent if the light has an energy greater than the band gap energy of the semiconductor it consists of. Due to the unilateral nature of the device this photocurrent is likely to be the only source of current in reverse bias. As can be seen in figure 3.4, the diode used in this experiment is predominantly constructed of $Al_{0.3}Ga_{0.7}As$. At 10 K the band gap energy of $Al_{0.3}Ga_{0.7}As$ is 1.8985 eV. The laser energies used to excite the sample in figure 4.2 are significantly lower than this. As explained in section 3.9, the operation of the *p-i-n* device as a detector is reliant on a quantum well in the intrinsic region. Exciting the device with light with an energy less than the bandgap of the main device is necessary to ensure that all absorption is occurring in the quantum well.

The sharp peaks seen in figure 4.2, such as at ≈−0.4 V on the 1.78 eV trace, are attributed to excitonic effects. A peak is expected to occur when the laser excitation energy is equal to the exciton resonance of the quantum well [112]. Changing the bias applied to the device decreases this resonance energy, due to the quantum-confined Stark effect for excitons. The way this contributes to the *p-i-n* detection mechanism is detailed in section 3.9, and will only be briefly discussed here.

When the device is used as a detector the shifts in the energy levels of the QW due to a strain wave passing through it, are measured as changing levels of photocurrent. These changes are caused as the exciton resonance energy changes, relative to the laser energy. Therefore, conditions which cause a steep gradient in figure 4.2 correspond to a high sensitivity of the device to strain. For the device shown in figure 4.2, a high sensitivity detection will be achieved when the device is used in the conditions corresponding to the lower bias edge of the photocurrent peaks, for instance ≈0.1 V on the 1.78 eV trace.

When the device is excited by laser light with a lower energy the amount of photocurrent seen decreases. Large electric fields are required to shift the energy levels of the QW far enough to bring the exciton resonance to these energies. At large fields the electron and hole in the exciton will become spatially separated, which decreases the absorption strength [113].

4.2.2 Superlattice Structure

In the SL structure the acoustic frequency excited in the upper SL, hereafter referenced to as the transducer, and the current voltage (I-V) characteristics of the lower saser SL, hereafter referred to as the active SL, were investigated. The frequency emitted by the transducer is important to identify the effect of the active SL on the signal. As explained in section 2.2.4, the effect of the active SL should be determined by whether the value of the Stark splitting applied to it is smaller or larger than the energy of the phonons passing through. A knowledge of the Stark splitting applied to the device and the energy of the phonons is therefore necessary for understanding the results. An estimation of this can be determined from the I-V characteristics of the device.

It has previously been shown that emission of coherent longitudinal acoustic phonons from a SL is possible if the SL is excited by a laser with energy greater than its first inter-band transition [20]. Reflection *pump-probe* experiments were performed on the SL side of MN796 to characterise the frequencies emitted by the transducer SL. These experiments were performed as detailed in section 3.6, using ≈100 fs pulses from the tunable, mode-locked, Ti-Sapphire laser described in section 3.4.1. Figure 4.3a shows the spectrum generated in a reflection *pump-probe* experiment where the transducer SL in sample MN796 was excited with 1.76 eV laser energy. It was at this energy the maximum response was detected in this SL. This energy is therefore approximately the energy of the 1st inter-band transition in the SL. As can be seen in figure 4.2, the *p-i-n* detector is also sensitive to this energy. This fulfils the specification

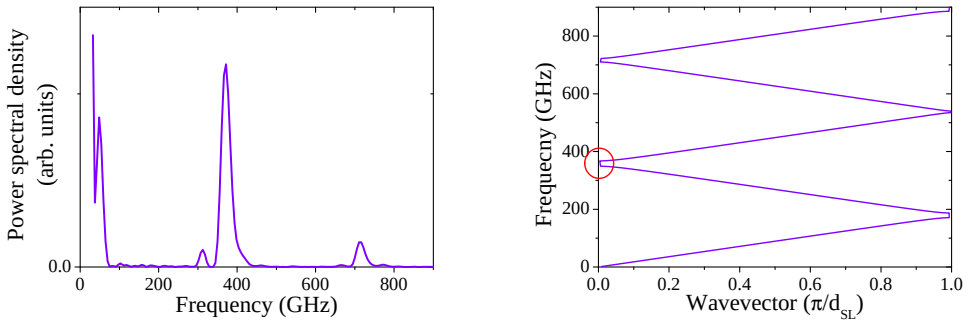

Figure 4.3: (a) The spectrum obtained from reflection *pump-probe* data for the generator SL in MN796. Data taken with a laser energy corresponding to 1.76 eV.
(b) Dispersion relation calculated for a 4 nm well, 11 nm barrier GaAs/AlAs SL. The red circle highlights the 1st zone edge mode of this SL.

of the experiment that the devices on both sides of the chip can be excited by the same laser frequency.

The strongest frequency seen in figure 4.3a is at (370 ± 20) GHz, the large error here is related to the small time window used to take this data. A dispersion curve calculated for the transducer SL, using the Rytov model [79] is shown in figure 4.3b. Comparison between this dispersion curve and the spectrum shown in 4.3a suggests that the strongest frequency seen is the 1st zone centre mode. This is highlighted in figure 4.3b with a red circle. It is this mode that is expected to be seen using the *p-i-n* photodiode detection method. The peak seen at approximately double this frequency is likely to be the 2nd zone centre mode of this SL. The frequency of this mode is too high to be clearly distinguished by the *p-i-n* detector used in these experiments. The peak seen slightly below the 1st zone centre mode is attributed to the $2k_{laser}$ mode. This is seen when the phonon wavevector is equal to twice the laser photon wavenumber. This mode is related to the detection selection rules of the reflection *pump-probe* experiment [23] and will not be present when a *p-i-n* photodiode is used for detection.

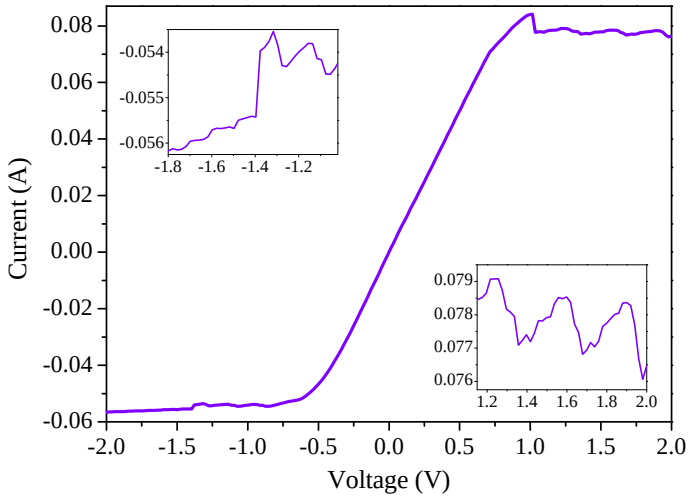

Figure 4.4: *I-V* measurement of an active SL device on MN796, this device has been processed into a 400 µm diameter mesa. The Measurement was performed at 4.2 K. The insets shows the plateau regions of this graph in more detail; the axis units are the same for the inset as the main graph.

An example of a *I-V* result typical to those seen for 400 µm diameter active SL mesas of MN796 is shown in figure 4.4. Although some variations between the resistance of the devices was seen, as will be further discussed in section 4.3.2, the general features of all devices studied was the same. This reading was taken at 4.2 K rather than the 10 K that the experiments were performed at. No significant differences in *I-V* results were seen due to this small temperature variation.

The *I-V* result in figure 4.4 shows three main regions: a linear response at low biases and two plateau regions featuring current oscillations, one at positive biases $>\approx 1$ volt and one at negative biases $<\approx -0.5$ volt. The current oscillations, shown in more detail in the insets of figure 4.4, are attributed to the formations of electric field domains within the SL.

The transport of electrons through a SL is a complicated problem and has merited a number of different theoretical approaches, see for instance the

reviews [52] or [51]. As described in section 2.2.1, the key difference between the different models of SL transport is whether they describe strong or weakly coupled SLs. Both the calculation presented in section 2.2.1 and previous analysis of SLs with properties similar to those of the active SL in MN796 have suggested that it should be considered as a weakly coupled SL and is best described in a sequential tunnelling regime.

In the region of negative differential conductivity of a weakly coupled SL, stable electric field domains can form as was discussed in section 2.2.1. This is the form of behaviour seen in the areas of the active SL I-V highlighted in the insets of figure 4.4. This behaviour is not seen in strongly coupled SLs, where domain walls are not pinned, so travel through the SL causing time dependent oscillations of current as regions of accumulated charge travel through the SL [51]. Time dependent oscillations in the current were also seen at some voltages in this SL, as confirmed by observing the current with a 12.5 GHz Tektronix digital oscilloscope. Such behaviour with regions of stable and unstable domain formation has previously been seen in weakly coupled SLs, see for instance [71, 114].

The presence of stable domain formation in the SL confirms that we are dealing with a weakly coupled SL, where there are unlikely to be any miniband effects. This is beneficial for sasing, where miniband tunnelling would prevent the phonon assisted transport required for the gain mechanism. Sasing effects are not predicted to occur at biases where domains have formed. The different electric fields in the device would prohibit the quantum cascade effect, see figure 2.5. Therefore the experiments discussed here will all take place below the region of domain formation, for the SL shown in figure 4.4, from 1 V to −0.5 V. The possible values of Stark splitting in this structure will be further discussed in section 4.3.3.

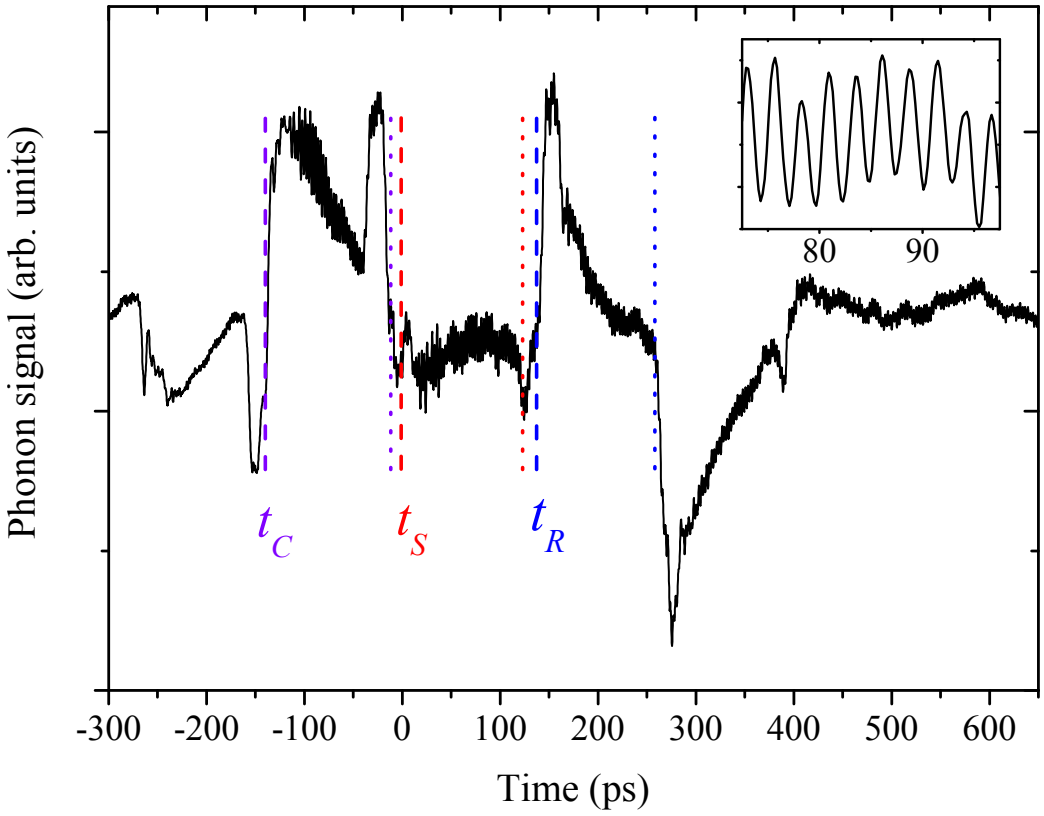

Figure 4.5: Example of signal produced when the SL structure of MN796 is excited with 1.77 eV laser energy, and the output is detected by a *p-i-n* photodiode. The inset shows a section of the trace in more detail; the axis title for the inset is the same as the main graph. The dashed lines refer to timings which have been identified as corresponding to the time taken to arrive at the detector from different parts of the SL structure. They are identified in figure 4.7.

4.3 Results and Discussion

4.3.1 Acoustic Generation in the SL Structure

A photocurrent *pump-probe* experiment was performed on the sample as detailed in section 3.10.

The phonon signal emitted by the superlattice device and detected by the

p-i-n diode is shown in figure 4.5. The most interesting feature of this result for this investigation is the output of the SLs. The inset of the figure shows a small section of the trace in more detail highlighting the high frequency oscillations, which are present throughout the figure. Figure 4.6 shows the Fourier transform of the 1st half of figure 4.5. It can be seen that the dominant frequency in the signal is (378 ± 2) GHz. This agrees with the earlier reflection *pump-probe* measurement carried out on this sample. It can be seen in figure 4.5 that this frequency is still clearly present after 1 ns, demonstrating the long lifetime of this mode and the high sensitivity of this detection scheme. In figure 4.6, a weaker signal at (517 ± 5) GHz can also be identified. These oscillations are attributed to the generation of the zone centre mode in the active SL. The longitudinal acoustic phonon dispersion was calculated for this SL using the same equation as previously applied in the case of the transducer SL. This verified the origin of this frequency. A broad envelope of lower frequencies can be seen in figure 4.6; these are attributed to strain pulses generated at various interfaces of the structure. The gaps between frequencies within this envelope are attributed to the interference of strain pulses reflecting back off various interfaces in the structure.

As can be seen in figure 4.5, many strain pulses are formed at different depths in the sample. Showing that the 1.77 eV light used to excite the device penetrates deeply into the structure. The pulses arrive at times corresponding to the time required to travel through the sample from the point at which they were generated. The journey times can therefore be used to find the origin of the pulses in the structure. The 0 time of the trace in figure 4.5 was set at the time when phonons generated at the surface of the device are expected to reach the detector. Signals arrive at earlier times than this due to the light penetrating into the structure and generating signals which are closer to the detector so have a shorter journey to reach it.

Half of the strain pulses present in figure 4.5 are due to the nature of the *p-i-n* photodiode detector. As explained in section 3.9, previous work [29] has shown that the signal seen in this detector originates from the quantum

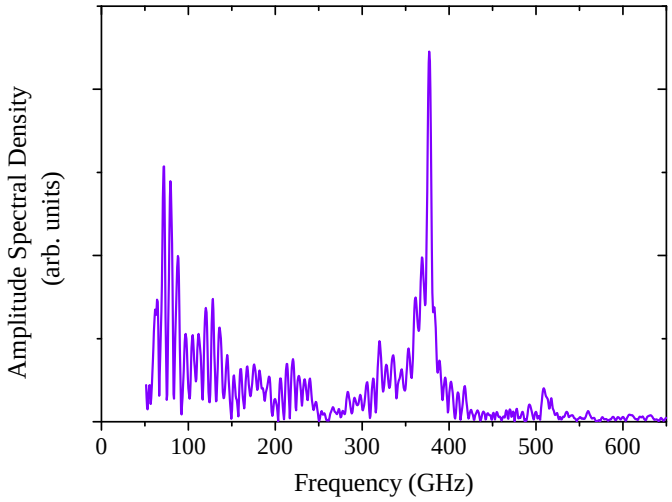

Figure 4.6: Amplitude spectral density obtained from the Fourier transform of the 1st half of the temporal signal shown in figure 4.5

well grown in its intrinsic region. This QW is 304 nm from the surface, an interface between the semiconductor sample and air. This interface is known to produce a complete reflection of strain with a π phase change [10]. A simple calculation of the time it will take longitudinal acoustic waves to travel this distance through $Al_{0.33}Ga_{0.77}As$ suggests that each pulse will return in $\approx$123 ps, having been reflected from the surface. Three of these reflections have been highlighted with dotted lines to illustrate this point. For instance the small pulse appearing around 0 time which is highlighted by the red dashed line reappears with a π phase change due to its reflection off the surface at $\approx$123 ps and is marked by a dotted red line. All timings are calculated using the speeds of longitudinal sound taken from [39] and layer thicknesses shown in figure 3.4. The timings seen in the trace are in good agreement with these calculations, accounting for the fact there is known to be the possibility of an up to a 10 % uncertainty in the layer thicknesses due to the nature of the MBE growth process.

Figure 4.7 demonstrates the origin of some of the strain pulses seen in figure 4.5. The largest strain pulses seen in figure 4.5 are generated around

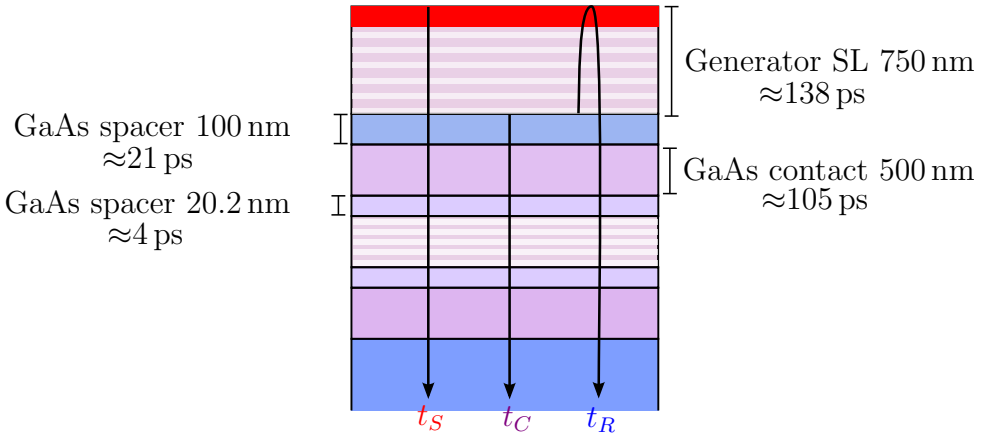

Figure 4.7: Schematic showing the origin of the strain pulses shown in figure 4.5. The red areas mark approximate interfaces where the strain is generated, and the arrows show the subsequent paths of the strain for the timings labelled in figure 4.5. The full active SL structure is shown but only the upper areas are labelled for clarity, the other areas can be identified by comparison with 3.4.

the interfaces between the transducer SL and the pure GaAs of the spacer and doped contact region. The change in the absorption of light between the mostly AlAs transducer SL and the pure GaAs lower layers is likely to be the cause of this strain. The time labelled t_C in figures 4.5 and 4.7, corresponds to the time for phonons to propagate to the detector from this layer. The strain generated at this layer propagates in both directions; this enables it to reflect off the surface and reappear in the trace at a later time. This path is shown by arrow t_R in figure 4.7 and by the blue lines labelled in figure 4.5. The time t_S in figures 4.5 and 4.7 is predominantly attributed to generation at the surface of the sample. A contribution to the signal at this time is also expected to occur due to the strain pulse generated at the interface between the 1st gradiently doped spacer and the active SL lower in the sample. This strain can then travel towards the surface, but be reflected by the transducer SL, causing some frequencies to appear in the trace at around this time. This will be further discussed in section 4.3.2. Other smaller pulses seen in the trace are from other layers deeper in the sample.

4.3.2 The Effect of Bias on Acoustic Emission from the SL Structure

The main aim of this investigation was to study any effect caused to the (378 ± 2) GHz frequency which was generated in transducer SL as it travels through the biased active SL. To achieve this a bias modulation technique was used to isolate the effect of bias on the signals seen in figure 4.5. In this experiment the sample was continuously excited by the laser and the bias applied to the device was modulated at 15 kHz. This frequency was used as a reference to the lock-in amplifier, meaning the lock-in amplifier can extract the effect of bias on the phonon intensity at the detector. This technique records the signal resulting from the subtraction of the signal with bias from the signal detected when the bias is not applied. In the resulting signal, only the changes that the application of bias causes to the signal generated by the laser will be present. This allows any small changes caused by bias to be distinguished from any changes in the signal amplitude caused by noise.

An example of the result seen when the bias is modulated between a positive bias of 500 mV and 0 mV is shown in figure 4.8. This has been scaled by a factor of 100 and plotted alongside a trace taken on the same day using normal laser modulation technique. In figure 4.8 it can be seen that many of the features generated by laser light in the structure are affected by bias. Initially we will focus on the effects to the (378 ± 2) GHz frequency mode. The inset of the figure shows an area where the (378 ± 2) GHz frequency can clearly be seen.

As can be seen in the inset of figure 4.8, the changes to the zone centre mode caused by the application of bias to the active SL are of the order of 0.5% of the amplitude of the signal generated. These changes are too small to be distinguished from noise without the use of the bias modulation technique described here. It was therefore not possible to directly measure the effect of bias to distinguish amplification from attenuation. An analysis of the nature

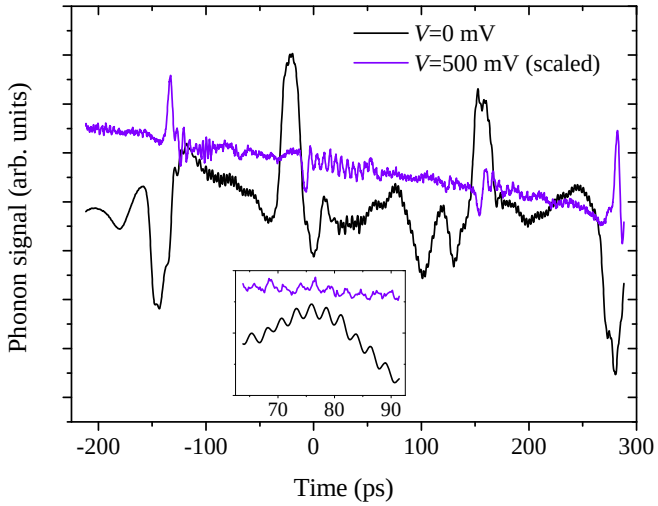

Figure 4.8: Changes caused by the application of bias to active the SL on the phonon signal. The violet trace shows the results seen when the bias applied to the active SL is modulated between 500 mV and 0. This trace has been scaled by 100 and is shown next to the signal generated by the laser when no bias is applied to the structure. The inset shows a section of this signal in more detail, the axis of the inset is the same as the axis of the main graph.

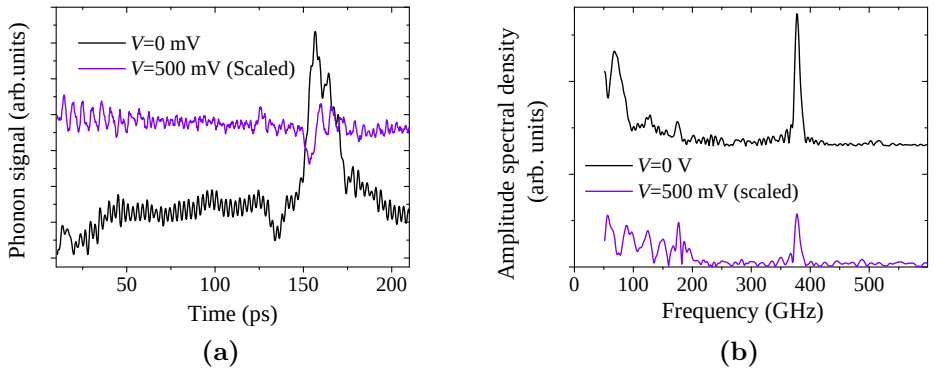

Figure 4.9: Figure showing a 200 ps time window, taken with modulated bias. For this signal the bias was modulated in a way which includes a positive and negative 500 mV contribution in the averaged signal. The bias modulation signal is shown scaled by 200 next to the laser modulation signal for comparison.(a) shows the temporal laser and bias modulated traces while (b) shows the spectrum of the traces.

of the signal will be undertaken later in this section.

To compensate for any polarity dependent pickup effects in the *p-i-n* photodiode, which may create a signal which is not interesting to this investigation, a new modulation method was devised. For this, a pulse was applied to the device featuring both a positive and a negative component, which was then compared to the signal without bias. This resulted in a summation of the signal caused by positive bias and the signal caused by negative bias. Any signal caused by electrical pickup of the bias from the SL on the *p-i-n*, will undergo a π phase change when the polarity of the bias is changed so should be cancelled by this summation. The spectrum of a signal obtained using this method is shown in figure 4.9b, and clearly features a 378 GHz component.

As can be seen in figure 4.8, signals occur in the bias modulation data at the times the strain pulses are present in the laser modulated traces, suggesting some bias dependence of these signals. These signals are short lived and were found to be affected by a change in bias polarity although they are not fully cancelled by the summation of different polarity signals.

As discussed earlier, the times when the strain pulses appear in the signal correspond to the times taken to travel from interfaces near the heavily n-doped contacts where the bias is applied. The application of bias in this area will change the carrier distribution and likely effect strain generation in these places, leading to the signal seen in figures 4.9a and 4.8. This effect was not studied in detail as it is not the main subject of this investigation.

In both figure 4.9a and figure 4.8 a burst of a lower frequency oscillation appears at 0 ps into the bias modulation trace. The frequency is identified as being ≈180 GHz. The timing of this frequency coincides with the path length of a signal generated in the top gradiently doped spacer layer travelling towards the surface but reflected from the start of the transducer SL. This SL features a stopgap at ≈180 GHz, as can be seen in figure 4.3b, here the reflection coefficient can be calculated to be close to one. The reflection of components of the strain travelling towards the surface by this SL is likely the cause for the ≈180 GHz, seen here. The bias dependence is attributed to a bias dependence of the generated signal. The pronounced appearance of the signal in the bias spectrum might indicate a frequency dependence to the change in generation caused by bias in this area. These effects are not relevant to the current investigation so will not be studied in detail in this work.

To asses the level of temporal shift caused to the signal by the application of bias the two signals, with laser modulation and with bias modulation shown in figure 4.9a were analysed. The signals were initially filtered using a 250 GHz high pass filter to obtain a cleaner 378 GHz signal. The filtered signal is shown in figure 4.10. After filtering the signal a fit was performed modelling the signal as $A\sin(\omega t + \psi)$, where A represents the amplitude of the oscillation, ω represents its angular frequency, t refers to time and ψ represents the phase. To perform a fitting of this equation to the data shown in figure 4.10, A and ψ are used as fitting parameters and the frequency was set as 378 GHz. To perform the fit the signals shown in figure 4.10 were split into 20 ps windows, 7 of these were taken in windows of the signal away

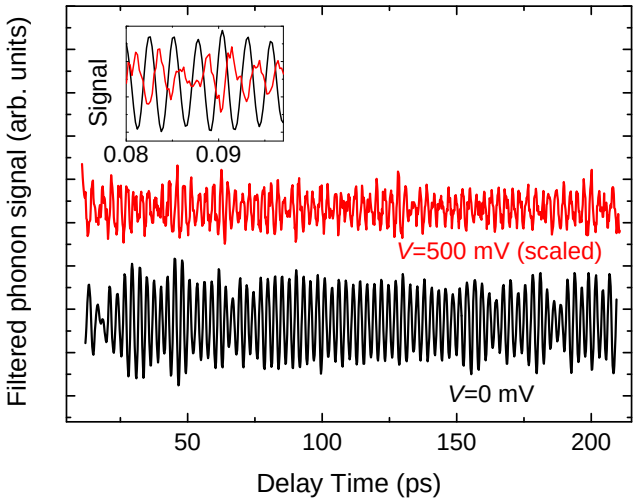

Figure 4.10: Signal as previously shown in figure 4.9 but with a 250 GHz high pass filter applied. The inset shows the oscillations in more detail for clarity the axis on the inset are the same as for the main graph.

from the strain pulses and the various phase differences found were averaged. The two values of ψ which were found for the signal with and without bias were subtracted from each other giving a phase difference. This gave a phase difference of $(0.76 \pm 0.03)\pi$.

To fully analyse the effect of bias on the signal the changes the bias causes to the amplitude of the signal need to be isolated from the changes it causes on the timing of the signal. To achieve this the data was again modelled as a sine wave. If the signal without bias is modelled as

$$P_0(t) = A\sin(\omega(t + t_0)), \tag{4.1}$$

then the signal seen as a result of bias modulation will be

$$\Delta P_0(t) = \Delta A\sin(\omega(t + t_0)) + A\Delta t\omega\cos(\omega(t + t_0)). \tag{4.2}$$

We can then use equation 4.2 to isolate the change in amplitude, $\alpha = D/A$ where D is the amplitude of $\Delta P(t)$ and A is the amplitude of $P_0(t)$. This is

shown in equation 4.3.

$$\alpha = \sqrt{\left(\frac{\Delta A}{A}\right)^2 + (2\pi f \Delta t)^2} \tag{4.3}$$

Similarly the phase difference of the signals can be expressed as

$$\Delta\psi = (H(\Delta A) - 1)\pi + \arctan\left(\frac{2\pi f A \Delta t}{\Delta A}\right), \tag{4.4}$$

Where H is the Heaviside step function. Applying this analysis to the data shown in figure 4.9a we estimate $\alpha \approx 0.14\%$ which means $\frac{\Delta A}{A} \approx 0.1\%$ and $\Delta t \approx 0.4\,\text{fs}$. The value of $\Delta\psi$ measured can only be achieved in equation 4.4 when ΔA is negative, meaning that this signal is caused by a decrease in oscillation amplitude.

How the magnitude of this signal depends on the magnitude of the bias applied will now be investigated.

4.3.3 Dependence of Signal on Bias Magnitude

The variation of the amplitude of the 378 GHz zone centre mode with bias is shown in figure 4.11. This was measured by taking multiple bias modulated traces in a 55 ps time window, where the zone centre mode is present, but the strain pulses are absent. A fast scanning delay stage was used to achieve this. The fast scanning delay stage allows extensive averaging of the signal, so the small signals seen at the lower biases can be distinguished from noise. The bias modulation used to measure these signals included a pulse which combined both positive and negative signals in the modulated bias, so only signals which were not cancelled by the changing of the polarity of the applied bias are considered. A fast Fourier transform was performed at each bias measured and the amplitude of the 378 GHz mode was assessed. The results can be seen in figure 4.11. A background was removed to account for the

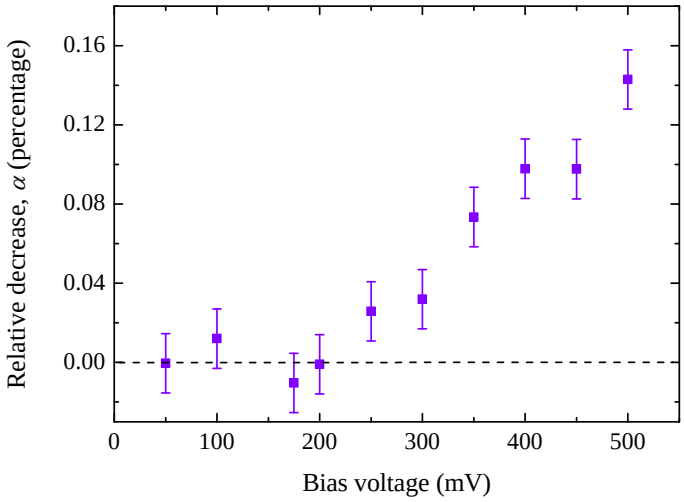

Figure 4.11: Figure showing the amplitude of the frequency identified as the zone centre mode of the transducer SL when different magnitudes of modulated bias are applied to the active SL. The dashed line represents the background level.

broadband noise in the Fourier trace. In figure 4.11 no signal is seen until ≈200 mV, after which the magnitude of the signal increases as the bias applied to the device is increased. Referring back to the *I*-*V* of the device used in this experiment, figure 4.4, we can see that this 200 mV threshold is not directly related to the current, which increases from 0 V without experiencing any threshold.

The lack of signal below ≈200 mV could be an indication that when this value of bias is applied the level of Stark splitting achieved between the different QWs in the SL structure is too small to cause an appreciable effect. This is surprising if all the bias applied is contributing to the Stark splitting. A further investigation was undertaken to asses the level of Stark splitting achieved in the device.

In the 400 µm devices studied resistances as low as 10 Ω were seen, with variations up to 16 Ω. The low resistance is attributed to the high doping

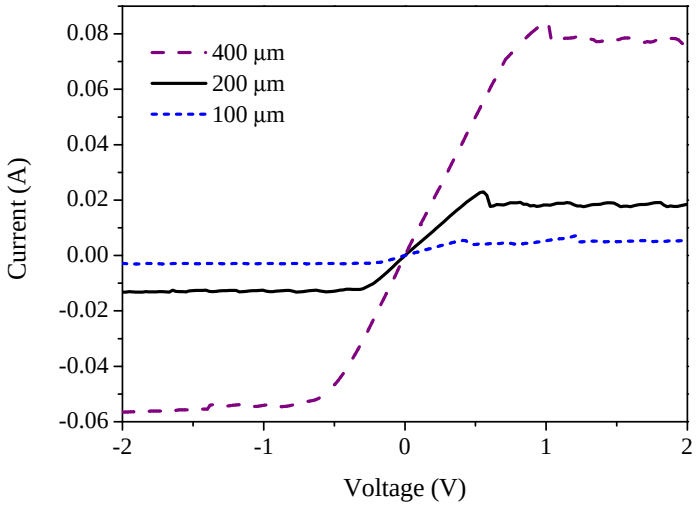

Figure 4.12: *I-V* characteristics of three different sizes of mesa processed from the active SL device structure on MN796. The Measurement was performed at 4.2 K.

levels in the active SL, which is doped to $2 \times 10^{17}\,\mathrm{cm}^{-3}$. It is possible when the device and packaging combined generates such a low resistance that a significant proportion of the resistance comes from parasitic resistances such as the contacts and the wires. This would mean that not all of the voltage applied to the device was dropped over the SL.

To try and isolate the proportion of the device resistance which is due to the SL, the variation of resistance with mesa area was investigated. Figure 4.12 shows the *I-V* characteristics of three different sized mesas. These were bonded on the same chip to minimise any effects from processing variations. As can be seen in figure 4.12, the resistance of a device increases with decreasing device area. This is as would be expected when looking at devices of different areas made from the same resistivity material. However, the variation with size is not linear, which suggests that factors other than size are also having an effect.

The mask used to create these mesas can be seen in figure 4.13. There

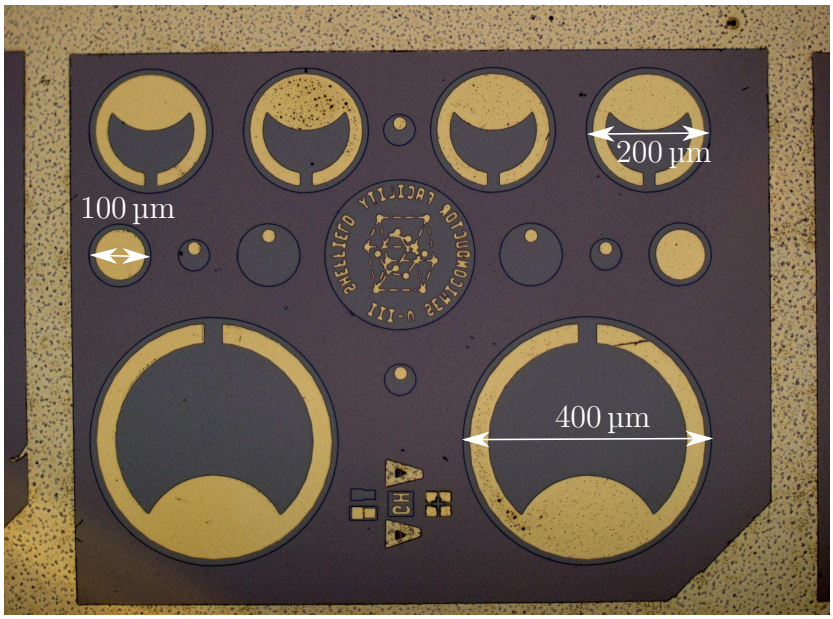

Figure 4.13: Picture of devices patterned with the "Sheffield" mask which was used to process devices for this experiment. The mesas are the circular rings with either circular or horseshoe shaped gold top contacts, the square around the edge provides a ground contact.

are two features of this relevant for this investigation: the top contacts are not proportional to the mesas area, also the geometry of the ground contact means that there is a large area surrounding the mesas where no gold is deposited. Any current flowing though the devices is therefore forced to travel a large lateral distance through the semiconductor contact material to reach the metal ground contact. These things are both likely to be making a contribution to the resistance of the devices.

An analysis of the various contributions to the device resistance was made using the assumption that the resistance for each size device could be split into three contributions: a contribution which varies with device area; a contribution which varies with the area of the top contact in each size device and a contribution which was constant with variations of device area. This allowed a set of simultaneous equations to be solved. The solution to this system of equations gives constants from which the contribution from each type of resistance can be analysed for the different device areas. Analysing

the resistances in this way suggests that for a 400 µm device up to 80% of the resistance may come from a non-area dependent contribution. This could be some combination of the wires used to bond the sample, the cabling connecting the holder to the voltage source, or the resistance caused by lateral transport through the back contact layer.

To check that this was a reasonable estimate a measurement was also performed bonding to ground through ≈1 mm of the grid contact. This gave a reading of 5 Ω. This places a lower limit on the non-area dependent resistance, since in this case the current was able to travel through the annealed metal grid contact which is likely to be significantly less resistance than the doped semiconductor contact layer. From this reading it would seem that 8 Ω for the non-area dependent resistance is not unreasonable. Due to the nature of the bonding process, the lengths of wire used and the distances between the ground bond and the device are variable. This may be the source of the resistance variations between different devices.

Unfortunately no simple method is known to accurately separate the contribution to the area dependent resistance due to the SL from that caused by other layers which vary with area. It is therefore not possible to obtain an accurate value for the Stark splitting over the superlattice, however we can say from these estimates that at least 50% of the voltage is not being dropped over the SL and it could be as little as 20% that is eventually reaching the device.

In relation to figure 4.11 this shows that at 200 mV there may not be a significant level of Stark splitting occurring in the active SL device. Further details of the consequences of this for an interpretation of the response of the signal to bias will be discussed in the following section.

4.3.4 Potential Causes of Bias dependence

Electrical breakthrough:

As is discussed in section 3.9 the sensitivity of the *p-i-n* device is related to the bias across it. The bonding of the sample involved a common ground between all the devices in the cryostat, it is therefore possible that applying a bias to the SL could change the level of bias seen on the *p-i-n* detector. This would cause a change in the detection sensitivity of the device, and appear in a bias modulation measurement. This is unlikely to be the cause of the signal seen in these samples, because the temporal shape of the bias modulation signals is different from the shape of the laser modulation signals. Also this effect should be largely cancelled by the addition of the two polarities of signals.

To further eliminate this possibility, a control experiment was performed in which the SL device adjacent to the one aligned directly opposite the *p-i-n* device was bonded. The experiment was then set up as before with the laser aligned opposite the *p-i-n* device and it was confirmed that a signal without bias similar to the one shown in figure 4.5 could be seen. The bias was then modulated in the bonded device. Since the laser was not incident on this device no signals should be generated here which could be seen by the *p-i-n* detector. However the devices do still share a common ground so may cause a change in the sensitivity of the *p-i-n*. No bias modulation signal was seen in this configuration, suggesting the sensitivity effect is not causing the signal seen in figure 4.8.

It is also possible that the detection sensitivity could be altered by a inductive coupling between the two devices either side of the semi-insulating substrate. The lack of signal in the control experiment described here also suggests this is not the case. Also it is likely if this were causing the signals the bias modulation signals would be identical in shape to the laser modulation

signals.

Heating:

At 500 mV, 24 mW of power is dissipated in the device. This will cause a temperature rise in the sample through Joule heating. This increase in temperature will change the speed of sound in the sample [115], causing a phase shift between the bias modulation and laser modulation signals. It may also cause a change in the amplitude of the signal due to an increase in phonon-phonon scattering, which could be caused by the increased number of background phonons. This effect should also appear in the control experiment described above. Its absence again suggests that this is not the cause of the signals seen in figure 4.8. To further confirm this is not the case the size of the signal change anticipated from this temperature dependent effect was estimated

The first step in this process was observing the phase shift caused by the application of a DC bias to the SL. If this phase shift is caused by the signal arrival time being altered by the increase of the temperature of the sample, we can estimate the temperature rise required to cause it. The speed of longitudinal sound waves travelling in the [100] direction in GaAs can be calculated using equation 4.5.

$$S(T) = \sqrt{\frac{C_{11}(T)}{\rho(T)}} \tag{4.5}$$

where $C_{11}(T)$ is an elastic stiffness tensor and $\rho(T)$ is the density. The dependence of C_{11} on temperature was modelled using data from [116]. While the dependence of ρ on temperature was modelled using data for the dependence of the linear expansion coefficient, α_L, of GaAs on temperature taken from [117]. α_L can then be related to ρ as shown in equation 4.6.

$$\rho(T) = \rho_0(1 - 3\alpha_L(T)) \tag{4.6}$$

Modelling the dependence of the speed of sound on temperature in this way allows us to estimate that applying 500 mV of DC bias to the sample will cause the temperature to increase from the 10 K that the cryostat is maintained at to ≈23 K.

The model used above was then applied to the bias modulation case to find the amount this temperature change follows the modulation of bias at 15 kHz. The 0.4 fs temporal shift previously calculated to be occurring when the bias is modulated corresponds to a temperature modulation of mK using this model, suggesting that the frequency of modulation is much greater than the thermal time constant of the sample. When this is true the frequency of bias modulation chosen is fast enough to prevent the majority of the changes the bias causes due to heating appearing in the bias modulation trace.

To further investigate the consequences of this heating, the level of attenuation expected for this temperature change was estimated. There are a variety of models which describe the attenuation of a phonon beam due to phonon-phonon interactions. These models have different ranges of validity depending on the frequency of the phonons travelling through the sample and the temperature of the sample. The important issues are how $\omega\tau_{th}$ compares to 1 and how k_bT compares to $\hbar\omega$, where k_b is the Boltzmann constant, T is the temperature, ω is the angular frequency of the phonon in question and τ_{th} is the average lifetime of thermal phonons. Identifying which theory is the correct one to use for the experiment in question is an important consideration, with errors of up to 2 orders of magnitude being reported when the wrong theory is employed [115, 118–121].

If $\hbar\omega \ll k_bT$ then the frequency of the phonon beam is less than the dominant frequency of the thermal phonons within the sample. In this case the dominant attenuation is through the interaction of the phonons with the thermal phonons. This is in contrast to the case when the frequency of the phonon beam becomes higher than the frequency of the dominant thermal phonons; in this situation the attenuation is more likely to be dominated by

the spontaneous decay into lower energy phonons [115].

When $\omega\tau_{th} \gg 1$ the phonon mean free path is long and the attenuation can be treated as individual scattering events. This theory was originally developed by Landau and Rumer [122]. When $\omega\tau_{th} \ll 1$, the phonon mean free path, is short and the phonon energy and momentum become less well defined. It is then more accurate to treat the phonons as a macroscopic wave which is attenuated through its coupling to the thermal phonon bath. This theory was originally developed by Akhesier [123].

For the experiment discussed here, the low temperatures and high phonon frequency, 378 GHz, mean we are definitely in the $\omega\tau_{th} \gg 1$ regime. However $\hbar\omega$ is, although smaller than k_bT, not much smaller. This puts us close to the limit where the phonons will begin to spontaneously decay. The Landau-Rumer method should deal best with phonons close to this limit [124]. It is also useful to note that, for these calculations, we are only interested in the changes in attenuation caused by changes in temperature. The spontaneous decay of phonons, which becomes the dominant process when $\hbar\omega \gg k_bT$, is only a weakly temperature dependent process [125] and would therefore have little influence on this result even if it is important for a calculation of the overall phonon attenuation in this regime. The attenuation was therefore considered in the Landau-Rumer regime.

The phonon scattering processes in this model were initially studied by Herring [126] and the attenuation caused by these process at low temperatures was later calculated by Simons [127] to be

$$\alpha(\omega) = A\omega^2T^3 \tag{4.7}$$

where for GaAs A=$9.4 \times 10^{-30}\,\mathrm{cm^{-1}\,s^2\,K^{-3}}$ [115]. Using this model the change in phonon amplitude caused by the mK modulation of temperature calculated earlier is $\approx 2 \times 10^{-5}$. Two orders of magnitude less than the change measured, suggesting that the heating of the sample causing attenuation through increased phonon collisions is unlikely to be the cause of the signal.

The approximately quadratic dependence of the amplitude of the signal on bias may be an indication that it is related to the dissipation of electrical power in the device. The possibility of a lattice heating effect has been dismissed, however there is still the possibility of an electron heating effect. This may cause an increase in the scattering of a phonon beam passing through the sample by increasing the number of allowed electron transitions.

At low temperatures many electron transitions which could cause the absorption of phonons are forbidden as they would involve the electrons moving to states below the Fermi level of their destination quantum well, which are already filled. The increased broadening of the Fermi level caused by the increased temperature may result in more of these transitions becoming allowed. A full calculation to quantify the magnitude of this effect when it is averaged throughout the entire SL has yet to be attempted, meaning this remains a possible explanation.

Sasing:

The active SL device used in this sample was designed to operate as a saser device, with specifications which had been seen to produce sasing in previous devices [60]. It may therefore be expected that sasing will be the cause of the bias dependence seen. However, the reaction of this device to bias is different to that seen in these previous samples. To understand if the device is acting according to SASER theory the cause of these differences should be understood.

The size of the effects seen in this device are very small with the maximum change induced by bias at 500 mV only being $\approx 0.14\%$. This is significantly smaller than was seen in previous saser devices [58, 60], these devices also saw gain which was not seen in this device. A possible explanation for these differences is due to the doping levels in the device.

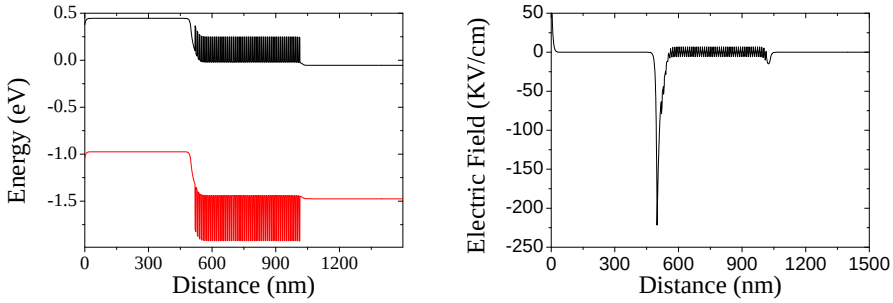

(a) Doping level $2 \times 10^{17}\,\mathrm{cm}^{-3}$ **(b)** Doping level $2 \times 10^{17}\,\mathrm{cm}^{-3}$

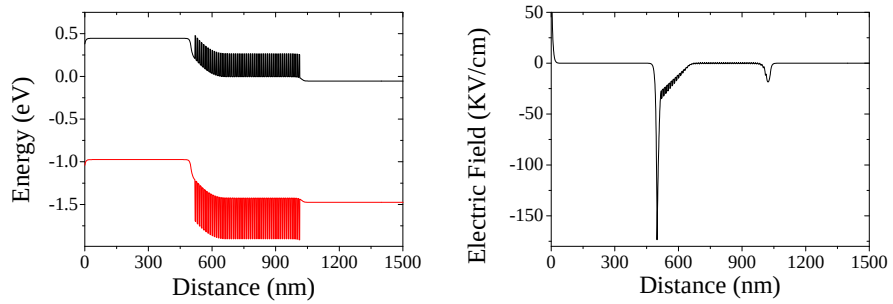

(c) Doping level $2 \times 10^{16}\,\mathrm{cm}^{-3}$ **(d)** Doping level $2 \times 10^{16}\,\mathrm{cm}^{-3}$

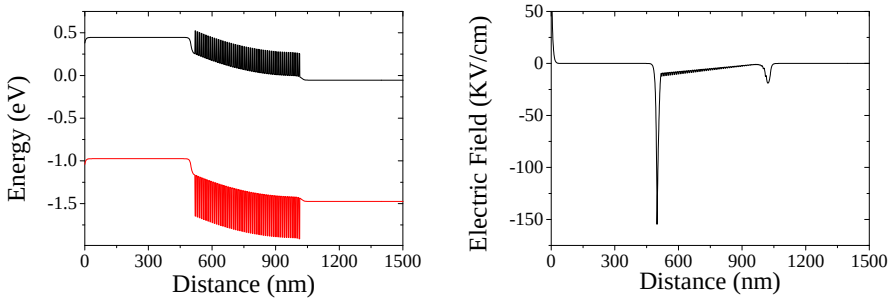

(e) Doping level $2 \times 10^{15}\,\mathrm{cm}^{-3}$ **(f)** Doping level $2 \times 10^{15}\,\mathrm{cm}^{-3}$

Figure 4.14: The energy bands recovered from solution of the Poisson equation for an SL with 5.9 nm wells and 3.9 nm barriers with different levels of doping. All simulations run at 10 K, with a bias of 500 mV applied to the device. The corresponding electric field plots for each doping level are shown to the right.

Figure 4.14 shows the solution found by a 1D Poisson solver applied to the active SL when different levels of doping are present. The simulations were performed using 1D Poisson solver freeware by Greogory Snider [128]. The situation when 500 mV of bias is applied has been modelled by setting the Fermi level of one of the contacts to 500 mV while the other is set at 0 mV. For a full solution of the carrier distribution in the case of a SL the Poisson equation should be solved self consistently with the transport equations within the SL structure. This is a complicated task. In previous work by Beardsley et al., on a similar structure [58], this was only achieved in certain limiting cases, which do not apply for the higher doping used in the current device. A simple Poisson solver was therefore used to gain an indication of the effect on the structure although it does not deal fully with transport within a SL. It can be seen in figure 4.14 that in the case of higher doping, when more charges are present, the field applied over the structure is screened, preventing the separation of the quantum wells necessary for the formation of a Stark ladder, in the majority of the structure. From the point of view of sasing this will mean that the Stark splitting required for amplification will not be achieved in the majority of the device, effectively lessening the length of the active gain medium. When lower doping levels are present in the device this screening becomes less pronounced, increasing the amount of device which experiences a Stark splitting.

This gives a possible explanation for the smaller effect seen in this device compared to the lower doped devices used previously. The only superlattice which had been studied previously with a doping nominally as high as in the current sample did show a gain effect, however this effect was weaker than measured in previous lower doped samples. Recent calibrations of the MBE machine used to produce these samples have shown that the doping levels of the machine have risen over time. It is therefore likely that the sample which was used in these experiments, which was more recently grown, had a higher doping level than the one used previously, despite them featuring nominally the same specifications.

These calculations suggest that doping levels as low as $2 \times 10^{15}\,\mathrm{cm}^{-3}$ may be required to prevent strong screening of the electric field applied to the device. Even in this case, shown in figure 4.14e, the Stark splitting is not equal throughout the wells. However, as discussed in section 2.2.4, an investigation of sasing in the presence of moderate levels of disorder such as in this situation found the phenomena to be robust.

Although a full simulation of the charge distribution within this SL is beyond the scope of this work, these results do seem to suggest that future works on SASER amplifier devices would be improved by using lower levels of doping in the structure.

A further difference between the reaction of this device to bias compared to previous devices, is that this device did not feature any gain effects. The theory of SASER amplification predicts that, when a Stark splitting which is equal to the energy of the phonon mode is applied, the device should move from attenuating the signal to amplifying it or vice versa depending on the specific device [58]. The energy of a 378 GHz phonon is 1.6 meV. If all the bias applied to the device was contributing to the Stark splitting of the SL it would be expected that the device would have moved through this Stark splitting in the bias range investigated, i.e. between 50 mV to 500 mV. This would be accompanied by a decrease in signal and a change of phase, followed by a subsequent increase of the signal in the opposite phase. No evidence of this is seen in this device. As discussed in section 4.3.3 due to the low resistance of the SL itself there is a high chance that between 50 to 80% of the voltage applied to the device is not dropped across the SL. If this is the case it is possible that at 500 mV the device has still not reached a Stark splitting equal to the phonon energy and as such would not have moved into the regime of gain. Above −500 mV the device reaches an area of negative differential conductivity and domain formation so sasing is not possible. This consideration provides further evidence that the high doping of this device is not beneficial for sasing applications.

The considerations presented in this section suggest that the differences between the response of this device to bias and the response of previous SASER devices to bias are consistent with what may be expected for a highly doped device, in the framework of a SASER theory. The possibility that this is the explanation for the effects seen can therefore not be ruled out.

4.4 Conclusions

A novel coherent detection scheme was used to study the effect of bias in an active device on a 378 GHz beam of phonons from a transducer structure. The bias was seen to cause the attenuation of the coherent phonons propagating through the device. This demonstrates the feasibility of a coherent phonon optics experiment which can decrease the amplitude of a phonon beam through the application of an electrical bias.

The amplitude of the effects seen in this experiment were small, the changes caused by bias were of the order of 0.14% of the signal generated. Although this device was designed to act as a SASER this is a much smaller effect than seen in previous SASER devices. The doping of this device was also greater than had been used in previous devices; it was hoped the additional carriers might lead to improved gain by providing an increase in the number of carriers available to take part in the transitions associated with phonon emission. However, an investigation into the effect of the electric field on this structure suggested that the high level of doping used led to a strong screening preventing the occurrence of the Stark splitting required for a sasing effect. It is thought that this may be a large contribution to the small effect seen in this device.

The dependence of the amplitude of this signal on the magnitude of the bias applied was investigated. This suggested that it was not possible to apply biases to this SL structure equal to the energy of this phonon mode

without moving the sample into a regime where electric field domains would form. This was caused by the low resistance of the SL compared to the other unavoidable resistances in the device structure. The approximately quadratic dependence of the signal on the bias magnitude suggests the possibility that electron heating may be a contributor to the attenuation of the phonon beam seen in this device.

Although no definite evidence of SASER effects occurring were seen in this experiment it has provided insight into the processes occurring in SASER devices. These results suggest that the optimisation of these devices may be achieved by careful consideration of the doping levels within the structure, with lower doping levels being desirable. This consideration will hopefully be instrumental in improving future SASER devices.

It has been successfully demonstrated that *p*-*i*-*n* devices can be used to provide a coherent detection method to measure the acoustic output of a separate active device. This suggests the feasibility of using this experiment to test the output of other acoustic structures. The experiment demonstrates the control of the amplitude of an acoustic signal by the application of an electrical one. This could lead to phononic chips where the interaction of phonons with charges, spins, and photons could lead to the control of new electrical, microwave, and thermal devices.

Chapter 5

A Weakly Coupled Semiconductor Superlattice as a Harmonic Hypersonic-Electrical Transducer

5.1 Introduction

As was discussed in Chapter 2 the behaviour of electrons and phonons in a semiconductor superlattice is significantly altered compared to that in bulk semiconductors due to the additional periodicity of the SL. In this chapter the possibility to use superlattices as transducers for the conversion between acoustic waves and electrical current is investigated. The conversion of high frequency acoustic waves into an electric signal may have potential applications in ultrafast electronics.

In this chapter the electrical response of a weakly coupled semiconductor SL to a train of acoustic pulses created by the excitation of an aluminium film transducer with the output of the Fabry-Pérot cavity discussed in section 3.4.3 is measured. The variation of the magnitude of the current response with

laser energy density and DC bias applied to the device mesa is investigated. These results are then compared to the theory of a weakly coupled SL as a hypersonic transducer which was detailed in section 2.2.3. The prediction of this theory that the output of the device should not be frequency dependent is then tested through a study of the frequency dependence of a selection of different aluminium films. The measured frequency dependence of the films is then compared to the frequency dependence predicted from simulations of the film output when it is excited by the optical pulse train not including any frequency dependence of the device. Finally the behaviour found in the main sample investigated is briefly compared to the behaviour in a series of other semiconductor nanostructure devices.

5.2 Experiment Overview

The aim of these experiments was to investigate the electrical response of semiconductor devices to hypersonic excitation. Of particular interest was the response of a weakly coupled SL to a quasi-monochromatic excitation in the form of a strain pulse train. The hypersonic pulses were generated by femtosecond laser excitation of an aluminium film transducer evaporated on the opposite side of the sample to the SL. The amplified Ti:Sapphire laser described in section 3.4.2 was used for this excitation. The samples were maintained at a temperature of 5 K, using the flow cryostat described in section 3.5.2, to prevent the attenuation of the high frequency component of the acoustic pulses as they travel through the substrate. A camera was used to align the laser spot opposite to the device mesa.

The samples were processed into electrical mesas allowing the application of bias to the devices and the monitoring of the current generated in them during the experiment. Details of the processing of these mesas can be found in section 3.2. The mesas used in this experiment were all 100 µm in diameter. This is approximately the diameter the laser spot was focussed to, meaning

the whole device should experience the laser generated phonons. The current in the device during the experiments was monitored using a 50 GS/s digitizing oscilloscope with a 12.5 GHz analogue bandwidth. This was triggered from a photodiode placed in the laser beam. Further details of the experimental arrangement and the microwave detection circuit used can be found in section 3.11.

An example of a current response typical of that seen in the semiconductor devices used in these experiments is shown in figure 5.1. Many electrical pulses are present, The first at $t = 0$ is identified as the response of the sample to laser light which has travelled through the substrate almost instantly. The acoustic response follows this at a time corresponding to the travel time of longitudinal phonons through the substrate. A careful measurement of the thickness of the sample with a micrometer, prior to starting the experiments, enables the positive identification of this signal. Further pulses can then be seen with a spacing corresponding to two trips through the substrate. These are pulses which have been reflected at the top surface of the sample after the device and travelled back. It is then possible for them to be reflected on the opposite side of the substrate to the device, and travel back through the substrate encountering the device again. In this work we focus on the response to the initial acoustic pulse to reach the sample.

In some samples, heat pulses were seen in addition to the optical and strain response of the sample. Figure 5.2 shows a typical heat pulse response, this was detected using the SL structure of wafer MN796 with -120 mV bias applied. The optical response, strain pulse response, the longitudinal (LA) and transverse acoustic (TA) heat pulse responses are labelled. In contrast to the coherent strain pulse caused by pico or femtosecond laser excitation, heat pulses are caused by slower thermal relaxation processes and are not coherent [129]. The heat pulses seen in figure 5.2 are much longer than the strain pulse, stretching over a time of $\approx$20 ns as opposed to the $\approx$500 ps strain pulses responses seen. The times at which the pulses are detected, 35 ns and 49 ns after the optical response correspond to the time of flight through the

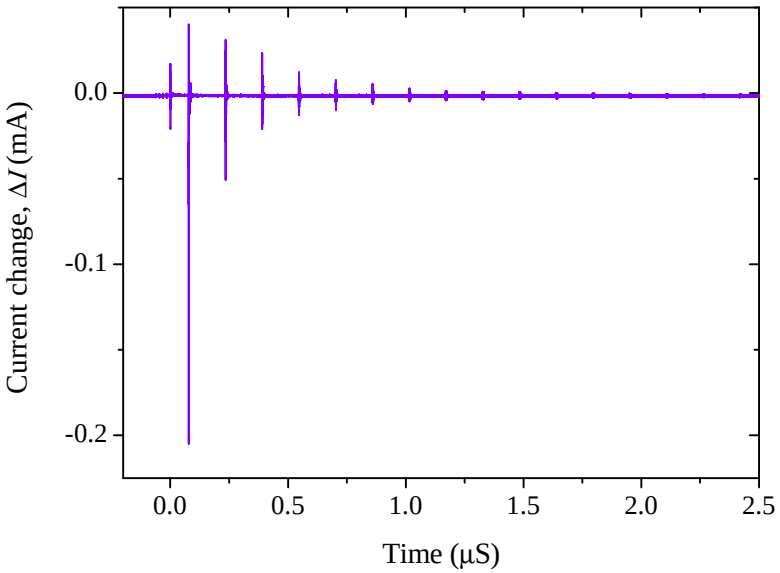

Figure 5.1: Current response showing optical pulse and multiple acoustic reflections. The trace was taken using the SL structure of wafer MN685 with a bias of 5 V applied, while the aluminium film transducer was excited with $\approx$5 mJ cm^{-2} of laser energy density.

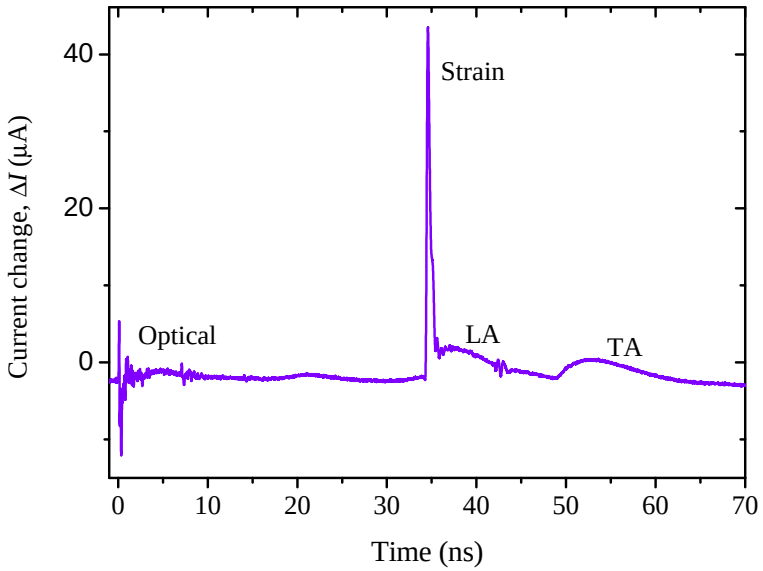

Figure 5.2: Current response showing heat pulses as well as the strain pulse. This was taken using sample MN796 with −120 mV bias applied. The sample was excited using a 46 GHz pulse train with a total energy density of ≈8 mJ cm^{-2}.

164 µm substrate for LA and TA phonons. This was calculated using the speed of LA phonons as 4730 m s^{-1} and TA phonons as 3350 m s^{-1} as taken from the ioffe database of semiconductor constants [39]. The experiments detailed in this chapter focus on the strain pulse response rather than the heat pulse response because the coherence of the strain pulse response leads to greater possibilities for the control of electrons.

In figure 5.2 an oscillation can also be seen in the middle of the LA heat pulse response. The timing between this response and the strain pulse response is equal to the timing between the main optical response and a smaller secondary optical response. The two optical responses are likely to be caused by the amplifier laser cavity allowing some leakage of the pulse build up between the main pulses. The response which appears in the centre of the LA signal is likely due to a small acoustic pulse which is generated by this optical leakage.

5.3 MN796

The majority of the investigation which is the subject of this chapter was performed using sample MN796, this sample will therefore be discussed initially, with comparisons to other samples made subsequently. Details of this sample are given in section 3.3.1, for this work only the doped active SL is utilised and other layers are removed.

5.3.1 DC *Current-Voltage* Response

7 different mesas created from wafer MN796 were used in this investigation. The large number of different samples were required for the investigation of different aluminium transducer films. Table 5.1 details the films used on the different mesas. These films were created using the thermal evaporation technique detailed in section 3.2.5. The thicknesses given in table 5.1 are measured by the quartz crystal monitor present in the evaporation chamber. These were used as a guide only and may include an error of up to 40%. The value given by the crystal monitor should be calibrated to account for the fact that its displacement from the source is different from the samples displacement from the source. This calibration should then be altered if the position of the crystal monitor is changed. The fact that the evaporator is used by multiple students who can change the arrangement makes these calibrations difficult. There is also the possibility that the reading on the thickness monitor is affected by the condition of the boat used in the evaporation, with the possibility that after multiple evaporations degradation of the condition of the boat results in it contaminating the aluminium. This may affect the reading of the crystal thickness monitor. The actual thicknesses of these films will be discussed in section 5.3.6. The composition of the non-standard films on mesas 4-7 will be discussed in section 5.3.5.

To characterise the electrical properties of these different devices *current-*

Mesa	Domain thresholds	Aluminium Film details
1	400 mV, −140 mV	30 nm
2	320 mV , −210 mV	50 nm
3	400 mV, −150 mV	100 nm
4	300 mV, −220 mV	100 nm on oxidised AlAs layer
5	330 mV, −220 mV	110 nm on oxidised AlAs layer
6	420 mV, 0.23 mV	Double layer. 60 nm, oxide layer, ≈50 nm layer
7	420 mV, −170 mV	Double layer. 125 nm, oxide layer, 25 nm layer

Table 5.1: Table displaying properties of aluminium films and the domain thresholds of different mesas. Film thicknesses shown feature uncertainties of 40%. Layers in order from surface towards the substrate.

voltage (I-V) measurements were performed on each device, these are shown in figure 5.3. The measurements were made as detailed in section 3.7, at a temperature of 5 K. This temperature was maintained through the use of the Oxford instruments flow cryostat described in section 3.5.2.

The different *I-V* curves in figure 5.3 all show similar features. All feature a reasonably linear region around 0 V then, after some threshold voltage, move into a regime of domain formation and current oscillation. The vertical lines indicate the start of the domain regime for mesa 2 as an example, the threshold voltages for all the mesas are recorded in table 5.1.

In the domain region the SL displays negative differential resistance, and current oscillations. As was discussed in section 4.2.2, MN796 was designed as a weakly coupled SL. In such structures the barriers between the quantum wells within the SL are large enough that the transport should be described by discrete equations, due to the localisation of the electrons within the quantum wells. This means the transport through the SL acts like a series of tunnelling events between adjacent wells, rather than conduction within a band as is seen in strongly coupled SLs [51]. In a weakly coupled SL it is possible to

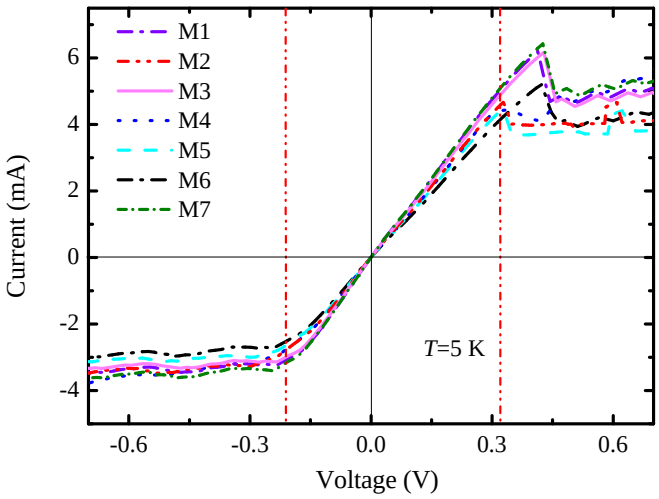

Figure 5.3: *Current-Voltage* characteristics of different SL mesas created using wafer MN796. This data was taken at a temperature of 5 K. The vertical lines indicate the value of the voltage thresholds where the device moves into a domain regime for one mesa as an example.

see the formation of stationary current oscillations. This is where a domain forms and becomes pinned to a section in the SL resulting in oscillations in the current being visible in the stationary time-averaged *I-V*. This form of oscillation can be seen above the threshold voltage on the negative side of the *I-V* and the positive side of some mesas. At some biases it was seen that the device also experiences current self-oscillations, where current domains form and travel in the device resulting in time dependent oscillations. This form of domains has also been previously seen in weakly coupled SL devices [71]. At biases where this happens it was not possible to see the acoustic response of the device as the strong current oscillations obscure the acoustic signal. Due both to this, and to the difficulty of modelling the SL in the domain region, most of this investigation will focus on the acoustic response of the devices below the threshold voltage.

It can be seen in figure 5.3 that the value of the threshold voltage and the resistance of the devices varies between the mesas. There is the possibility of

growth variation across the wafer leading to the alteration of doping levels between regions and therefore causing a higher resistance in some areas of the wafer. There are also two processes in the device fabrication which are likely to produce variation between mesas of the same wafer: the contact metallisation and the bonding of wires to the contacts. Both of these processes are capable of altering the device resistance by adding additional parasitic resistances. The variation in the threshold voltage is likely to be due to alterations in the behaviour of the SL emitter contact, which is crucial in the formation of domains [51]. The threshold voltages recorded in table 5.1 will be used to distinguish the relevant current-voltage regime for each mesa when the current response of the device to acoustic excitation are recorded with a DC bias applied to the device.

5.3.2 Acoustic Response when Excited with a Pulse Train

The novel component of this investigation was the use of the Fabry-Pérot cavity to create an optical pulse train. The response of the devices to the acoustic output generated when an aluminium film is excited by this pulse train will therefore be the main subject of this chapter. A comparison with the response to single pulses will be made in section 5.3.7. Details of the Fabry-Pérot technique and the different acoustic pulse trains created when different aluminium films are used can be found in section 3.4.3.

Figure 5.4 shows a typical current response of a SL device made from wafer MN796 to a 46 GHz pulse train, with and without the application of bias. Figure 5.4 shows that when the bias applied to the device is positive the current response is negative and vice versa. The acoustic pulse is therefore producing a decrease of the current in the device. This was true for all biases below the threshold voltage where domain formation starts to occur within the device. It can also be seen that the application of bias causes large increases in magnitude of the acoustic response seen in this device.

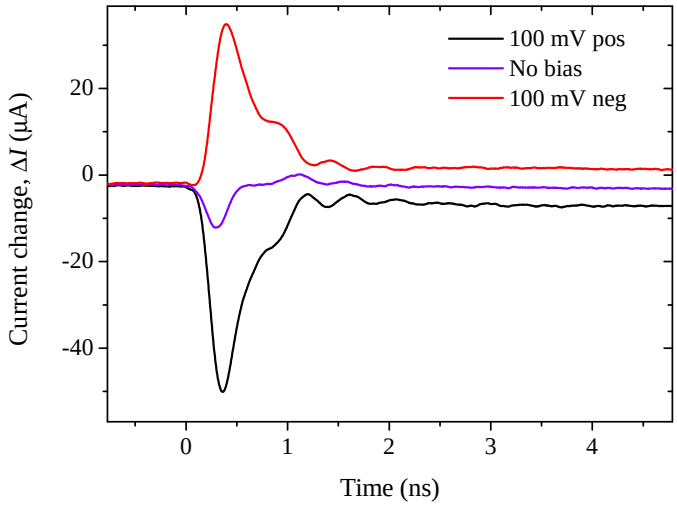

Figure 5.4: Current response of wafer MN796, mesa 4, to a 46 GHz acoustic pulse train with and without the application of bias. This signal was taken with a laser energy density of $\approx 8\,\mathrm{mJ\,cm^{-2}}$.

Figure 5.4 shows that the pulse is predominately of a single polarity. This suggests that the signal is predominantly from the SL itself, as signals from the contacts or other interfaces in the device have previously been shown to be bipolar in nature [48].

When biases above those where domain formation was seen are applied to the device the sign of the signal seen will change, however this was not the main subject of this investigation as was discussed in section 5.3.1.

The amplitude of the pulses forming the train decreases with each pulse, meaning that after a certain number of pulses it will be undetectable by the device. How the device responds to this pulse train is determined by how this train length compares to the device length. At very low frequencies individual pulses from the train can be resolved. This is due to the separation between the pulses being sufficiently large that only one pulse is present in the device at a time. Figure 5.5 shows an example of a signal taken at the point the cavity spacing is becoming large enough that the pulses begin to separate,

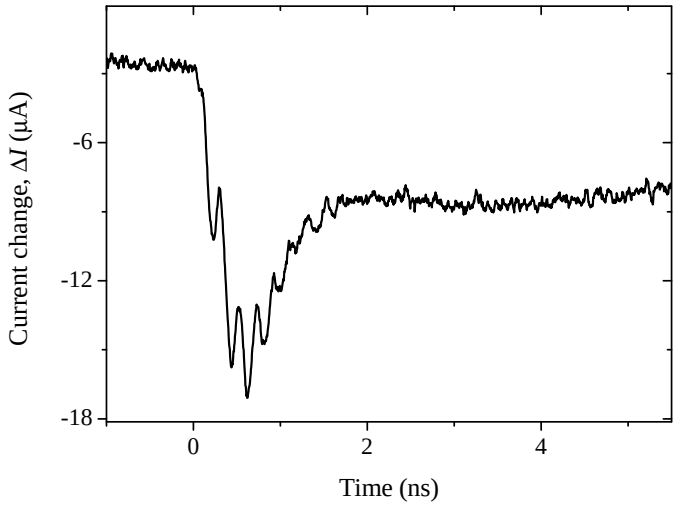

Figure 5.5: Current response of wafer MN796, mesa 3, to a 5 GHz acoustic pulse train. This signal was taken with a laser energy density of ≈7 mJ cm^{-2} with a bias of positive 300 mV applied to the device.

here the cavity is set to a frequency of 5 GHz.

As the train frequency is increased single pulses are no longer resolved and the temporal length of the acoustic response seen decreases until a point at which it becomes stable. This behaviour can be seen in figure 5.6, which shows a coloured contour plot of the temporal acoustic responses seen at frequencies between 14 GHz to 30 GHz. This data was taken using mesa 3, with a bias of 300 mV applied. The amplitude of the maximum acoustic response at each frequency has been normalised to one to make a comparison of the temporal lengths of the traces clearer. Figure 5.6 shows that temporal extent of the peak in the acoustic response has approximately halved in the frequency window shown. The distance from the lower side of the SL in the structure of MN796 to the surface of the sample is ≈750 nm. It would be expected that the lower limit of the temporal acoustic response would be the time taken to traverse this distance twice, ≈300 ps. This is comparable to the length of the signal in the sample, as can be seen in figure 5.6. The fact that the time that the maximum of the signal appears in the trace stays quite

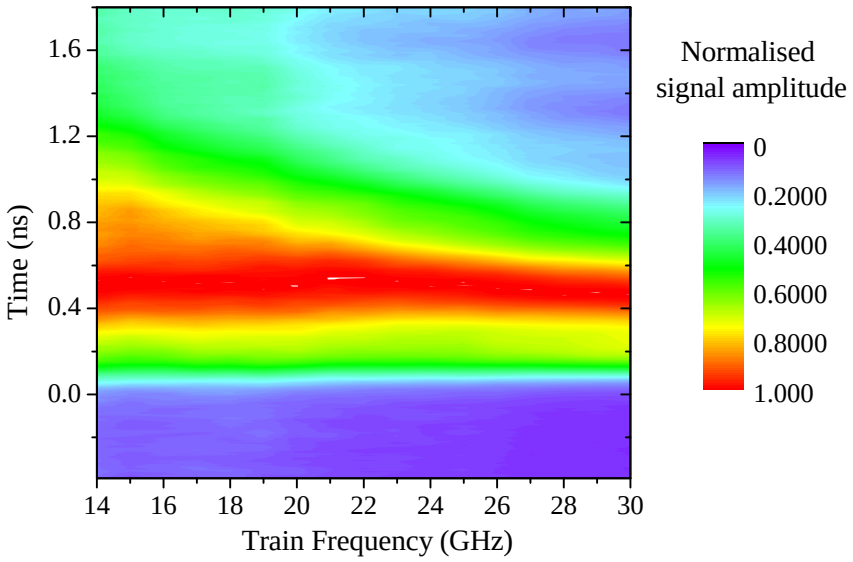

Figure 5.6: Variation of temporal acoustic response length with frequency of pulse train. This data was taken using mesa 3 and an ≈100 nm aluminium transducer film. The transducer was excited with ≈7 mJ cm^{-2} of laser energy and the acoustic response was recorded with 300 mV of bias applied to the device. The amplitude of the maximum acoustic response at each frequency has been normalised to one.

constant despite the changing pulse length shows that the rise time of the electronics is not changing with pulse length. This implies that the rise time in the circuit is comparable or shorter than the pulse length.

The acoustic response of the weakly coupled SL device, grown in wafer MN796, will now be investigated. Initially the cavity spacing and hence the transducer film output frequency are kept constant and variation of the magnitude of the electrical response with laser energy density and device bias are investigated. The variation of the magnitude of the response was investigated at several different fixed frequencies. This was chosen between the values of 35 GHz to 100 GHz, as at these values the pulse length was found to be constant suggesting the the device is experiencing the whole pulse train. Also, as is discussed in section 3.4.3, the frequency of the pulse train

can be considered close to monochromatic at frequencies in this range. The variation of the magnitude of the electrical response when the frequency of the pulse train is varied is later discussed in section 5.3.5.

5.3.3 Variation of the Magnitude of the Device Response at Fixed Acoustic Train Frequency

Charge Transfer

The theory described in section 2.2.3 deals with the changes caused to the device current. The shape of the current response was constant with all parameters apart from pulse train length, meaning no physics is lost if the variation of charge rather than current is analysed. The current response may be affected by the detection circuit and parasitic components within the device packaging. Therefore, when making comparisons of the magnitude of the signal in the device in different conditions a value of the charge displaced by the pulses was used rather than the current. This value was found by integrating the current pulse as shown in equation 5.1.

$$\Delta q = \int_0^{t'} \Delta I(t) dt \tag{5.1}$$

In equation 5.1 q is the charge, I is the current, t is time and t' is a time exceeding the length of the strain pulses. It can be seen in figure 5.7 that the signals featured varying backgrounds and, as shown in figure 5.2, some feature heat pulses. To remove these backgrounds, including the heat pulse, a polynomial fit was used. Examples of this fit applied to two extremes of the energy dependence of mesa 3 when excited with a 60 GHz pulse train are shown in figure 5.7.

The fit is shown in the area it is integrated over, which was chosen to be

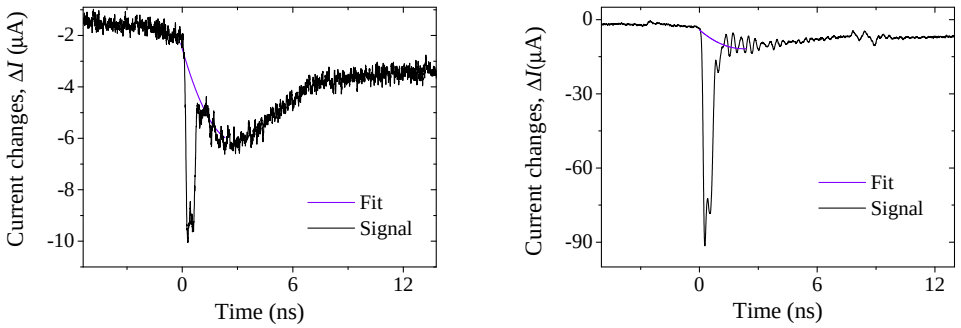

(a) $3\,\mathrm{mJ\,cm^{-2}}$ **(b)** $7\,\mathrm{mJ\,cm^{-2}}$

Figure 5.7: Example of fits used to remove the backgrounds from signals taken at two different powers using mesa 3. The data was taken when a bias of 300 mV was applied to the device and it was excited with a pulse train of 60 GHz

slightly longer than the pulse width. As well as fitting the heat pulse after the strain pulse a small amount of the data before the strain pulse was included in the fit window to ensure the fit starts at the same background level as the strain pulse. The data was smoothed before fitting to lessen the effects of any oscillations, such as those seen in figure 5.7b. The signal was integrated in the window where the fit is shown in figure 5.7, the fit was then integrated in the same manner and the difference between the two was used as a measure of the charge transferred by the hypersonic pulse.

Fluence Dependence

Figure 5.8 shows the dependence of the charge transferred by the hypersonic pulse on the energy density of the optical excitation used to generate the hypersonic pulse train, for several different mesas, applied biases and frequencies of pulse train. The values of biases used are below the thresholds for domain formation identified in table 5.1. The solid and dashed lines show quadratic and linear dependences respectively. From this figure we can see that the energy dependences of the acoustic response are superlinear and

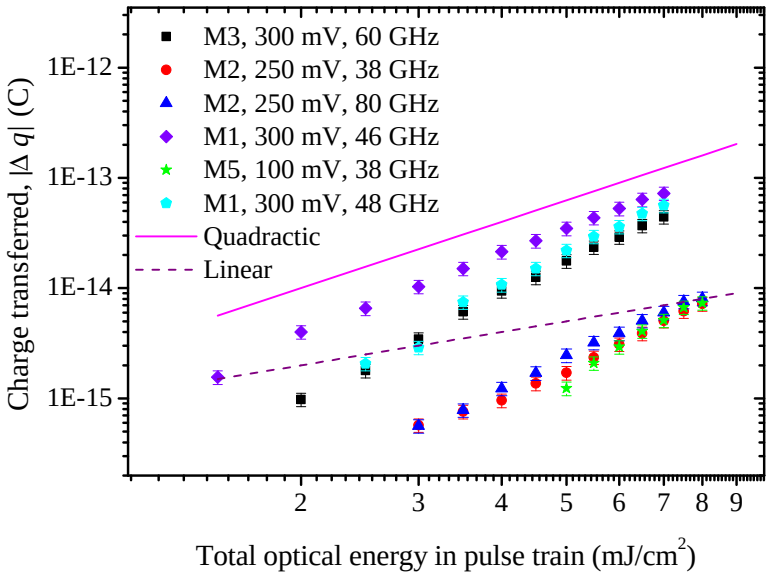

Figure 5.8: Dependence of charge transfer in the SL device on the energy of the acoustic pulse train, for several different mesas, bias voltages and train frequencies, as shown in legend. Quadratic and linear dependences are also shown for comparison.

reasonably close to quadratic. For instance a fit to the data taken with M1 with a bias of 300 mV when excited by a 46 GHz acoustic pulse train gives a power of 2.44 ± 0.05.

Non linearity in the propagation of acoustic pulses is expected when strain amplitudes of $> 10^{-4}$ are achieved, at which point the strain becomes high enough to generate solitons; as detailed in the following references [130–132].

Details of the strain generated by an aluminium film transducer and equations which may be used for the calculation of its magnitude are given in section 2.3. The fluences shown in figure 5.8 are measured using a power meter in the laser beam after the cavity. The power meter placed here is measuring a sum of the power of all the pulses output by the cavity. A calculation of the strain magnitude, using equations 2.27 and 2.28 for the case of: a pump fluence of $8\,\mathrm{mJ\,cm^{-2}}$, film thickness 100 nm and $\tau_e = 4$ ps; gives a

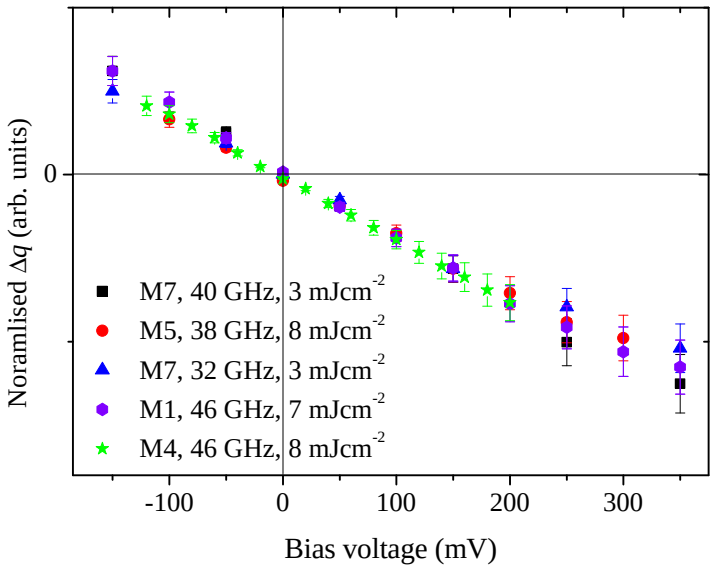

Figure 5.9: Dependence of charge transfer magnitude in the SL device on the bias applied to the SL mesa, for several different: mesas, train frequencies and total energy densities of laser excitation, as shown in legend.

value of $\epsilon = 2.5 \times 10^{-3}$. In previous works non-linear effects have been seen in GaAs at these values of strain [130] which could suggest that the non-linearity seen in figure 5.8 is due to non-linear effects in GaAs. However, this would be assuming that the laser energy supplied to the cavity was concentrated into a single pulse rather than split between different pulses as is actually the case. The value of the strain in the largest pulse in this train is $\epsilon = 2.8 \times 10^{-4}$. At these values of strain strong non-linear effects are not expected in GaAs [130], particularly in this sample where the substrate is only 164 µm thick.

Bias dependence

The effect of applying different biases on the magnitude of the charge transferred in the devices by the hypersonic pulse trains is shown in figure 5.9. The biases used here are all below the thresholds for domain formation identified

in table 5.1. It can be seen that the magnitude of the signal has a close to linear dependence on applied bias for all the conditions shown in figure 5.9.

These results will now be compared to the theoretical description of the acoustic response of a weakly coupled SL to a single frequency acoustic wave which was described in section 2.2.3.

5.3.4 Comparison between Theory and Experiment

For the case when the phonon energy is smaller than the voltage scale of the non-linearity in the *I-V* curve, the device is operating in the classical limit and theory developed in section 2.2.3 predicts that the current response of a weakly coupled SL should be described by the second derivative of its *I-V*. It was assumed that the phonon energy is sufficiently small to justify the approximation necessary for the reduction of equation 2.22 to equation 2.23 when the phonon energy is an order of magnitude less than the voltage. At 100 mV this is true for frequencies of less than ∼500 GHz, making equation 2.23 valid for the frequencies detailed in this chapter. As discussed in section 3.4.3, the Fabry-Pérot technique combined with aluminium film transducers is not capable of achieving frequencies above 500 GHz because there is not sufficient spacing between the individual pulses at these frequencies for them to be resolved.

To make a comparison between this and the results presented in section 5.3.3 using equation 2.23 it is therefore necessary to know the second derivative of the device *I-V*. Figure 5.10 shows the *I-V* of mesas 2 and 3 fitted using equation 5.2, in the region below the voltage threshold.

$$I(V) = aV + bV^3 \tag{5.2}$$

Equation 5.2 is a standard equation for use as an approximation of the *I-V* characteristics of tunnel devices [133], with a and b as fitting parameters

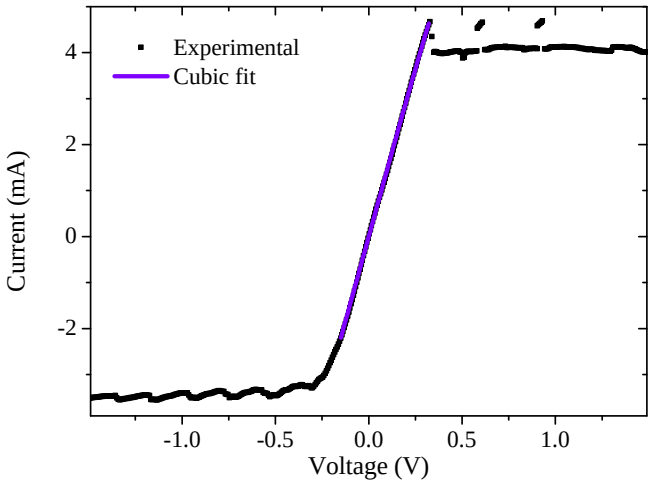

(a) Mesa 2

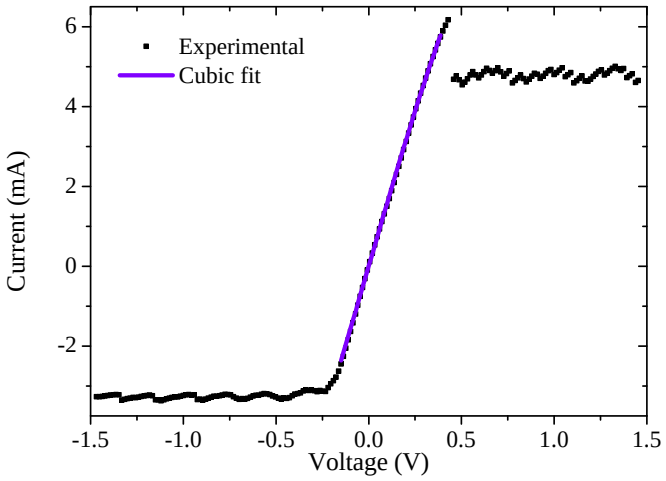

(b) Mesa 3

Figure 5.10: Cubic fits to the I-V curves of mesas 2 and 3 below the thresholds voltages where electric field domains form.

which depend on the electric properties of the device. It can be seen, in figure 5.10 this gives a good agreement. The adjusted R-squared value calculated by the technical computing language Matlab for the fit of mesa 2 was 0.9996 while for mesa 3 the value was 0.9995. The fitting parameters used for mesa 2 were $a = (0.014\,82 \pm 0.000\,06)\,\mathrm{S}$ and $b = (-0.0038 \pm 0.0009)\,\mathrm{S\,V^{-2}}$ while for mesa 3 agreement was found with $a = (0.0160 \pm 0.0001)\,\mathrm{S}$ and $b = (-0.007 \pm 0.002)\,\mathrm{S\,V^{-2}}$. Since the *I-V* curves of all the mesas are quite similar, see figure 5.3, it seems reasonable to assume that this fit makes a good approximation to the *I-V* results of all of these samples.

The doped semiconductor contact regions either side of the superlattice have a large effect on the electric field distribution in the SL mesa and therefore an effect on the device *I-V*. To make a comparison between the equations derived in section 2.2.3 and the device *I-V*s we therefore need to include their effect. Due to the complexity of a full model of the transport in the device including the contacts, for a first approximation here we just include the length of the contacts into the length used in the transport equation 2.23. For future work a more advanced analysis of this device is expected to give a better agreement to the experiment. Substituting equation 5.2 into equation 2.23, we may obtain equation 5.3.

$$I(V) = \frac{3b}{2}\left(\frac{Dd_L}{ed_{SL}}\right)^2 \epsilon^2 V_{DC}. \tag{5.3}$$

Equation 5.3 contains a square dependence on strain, ϵ, and a linear dependence on the bias voltage applied V_{DC}. The other symbols in equation 5.3 are D = deformation potential, d_L = device length, d_{SL} = SL period, e = charge on an electron, with b being the fitting parameter from equation 5.2.

As was shown in figure 5.9 the charge transferred in several devices, under several different conditions, all feature a linear dependence on bias, to good approximation. The pulse width was not found to vary with bias so the charge transferred is linearly related to the current, this then shows good agreement with the prediction of equation 5.3. Figure 5.8 shows the

dependence of several devices on laser fluence. As is discussed in section 5.3.3, for values corresponding to strains of less than 10^{-4} the dependence of strain on fluence is expected to be linear. This means that figure 5.8 shows that the experimentally obtained results have a close to quadratic dependence on strain.

The theory described in section 2.2.3 therefore provides a good description of the variation of the magnitude of acoustic response seen when the device is excited by a fixed frequency acoustic wave train. The slight deviations between the theory and experiment may suggest that a more sophisticated approach could be required for a full description, for instance a more accurate fit to the *I-V*, and a full description of the effect of the contacts on the current.

Unfortunately a quantitative comparison between any theoretical estimate of the strain and the measured strain values is difficult to achieve with the current samples and experimental procedure. There are several values needed for an estimate of the strain using equation 5.3 which are not known to a high degree of accuracy. Equation 5.3 requires a value of the magnitude of the strain which the SL experiences at the frequency of the pulse train. As was discussed in section 3.4.3, the pulse train created by the Fabry-Pérot cavity features a decay between the pulses and may also feature multiple harmonics of the frequency making an estimation of the magnitude of the strain at a particular frequency difficult. This is further complicated by the fact we expect that after the train of strain pulses passes through the SL it will be reflected at the surface of the sample and pass back through the SL again. This means the pulse train is able to interfere with itself in the SL. The distance between the top of the SL and the surface is not accurately known making any simulations of this effect difficult.

The use of equation 5.3 to estimate the magnitude of the strain also requires a knowledge of the value of the b coefficient obtained from fitting the *I-V*. This value characterises the small cubic contribution to this *I-V* and is very susceptible to any fluctuations in the device resistance, such as may be caused

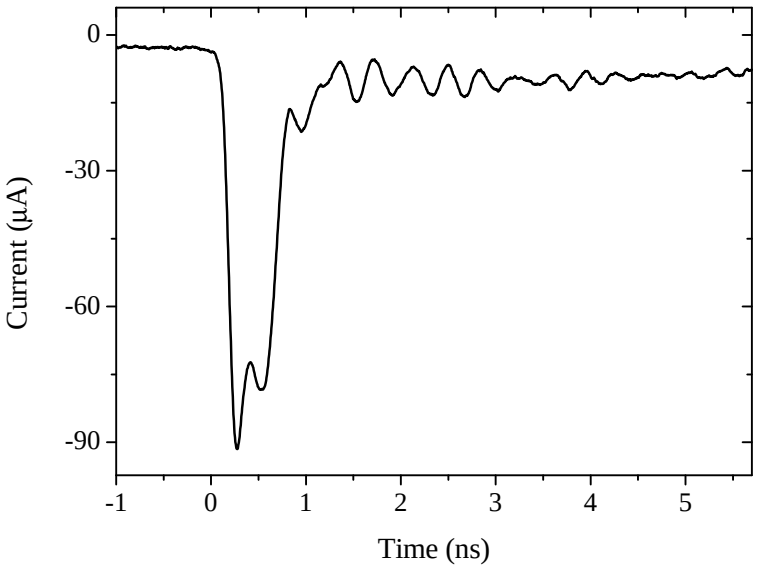

Figure 5.11: Example pulse used for quantitative comparison between the strain magnitude predicted by theory and measured experimentally. Pulse was taken using mesa 3, with 300 mV of bias applied and excitation with a 60 GHz pulse train, using a total laser energy density of $7\,\mathrm{mJ\,cm^{-2}}$.

by slight alterations in temperature day to day or differences in the charge distribution caused by differences in the device cooling rate. For example, fitting two I-V curves of the same device which where taken on different days was found to give the two different values of b, $-5.5 \times 10^{-4}\,\mathrm{S\,V^{-2}}$ and $-4.5 \times 10^{-4}\,\mathrm{S\,V^{-2}}$. Also there are potential errors in the value of b depending on where the voltage threshold is taken to be with a difference of one point on the curve having an effect on the value.

A final difficulty is in the estimations of I from the experimental data with there being a possibility of this value being affected by the device packaging and the detection circuit. Despite these difficulties a trace was chosen to provide an estimate to see if an order of magnitude level of agreement was possible between the theory and experiment.

To estimate the experimental current a typical signal taken with mesa 3

at a bias of 300 mV and a train frequency of 60 GHz was used. This is shown in figure 5.11. The train frequency of 60 GHz was used because as can be seen in figure 3.8b, for this frequency, and a value of τ which is reasonable for the 100 nm film on this sample, the output of the pulse train should be monochromatic. The mean current in the device was calculated by dividing the charge transferred in the device by duration of the acoustic pulse seen, found by using the full width at half maximum. In the signal shown in figure 5.11 this is 530 ps giving a mean current of $\Delta I = 8.7 \times 10^{-5}$ A. Fitting the *I-V* of this mesa gives a value of $b = -7.1 \times 10^{-3}\,\mathrm{S\,V^{-2}}$. For an order of magnitude estimate of the strain we take the value of the strain formed by first laser pulse leaving the (FP) cavity, this will give an upper limit for the strain predicted by the theory. For excitation using an energy density $7\,\mathrm{mJ\,cm^{-2}}$, in the full pulse train we expect the level of strain in the first pulse to be $\epsilon \approx 8 \times 10^{-5}$. The value of 1.3 µm was used for the device length, and 10 eV for the deformation potential in GaAs, as was discussed in section 1.2.1 this value is also not know to a high degree of accuracy. Evaluating equation 5.3 with these values gives a change in current of 3.2×10^{-5} A, which is in good agreement with the experimental values considering the large uncertainties in many quantities.

Equation 5.3 predicts that there should be no dependence of the response of the device on the frequency of the acoustic excitation. To test this prediction the variation of the magnitude of the electrical response as the frequency of the pulse train was altered was investigated.

5.3.5 Dependence of the Electrical Response Magnitude on the Frequency of the Acoustic Pulse Train

At low frequencies the device is operating in the classical limit and the current follows the field instantaneously, it is then possible to relate the change

in current caused by the phonons to the DC I-V of the device. As was explained in section 5.3.4, in this limit equation 5.3 can be formed and the current response no longer includes any dependence on the frequency of the exciting phonons. This means that any variation seen in the amplitude of the hypersonic response when the frequency of the pulse train is varied will be due to the frequency dependence of the output of the transducer film.

To test this hypothesis, the frequency dependence of the same film was measured under different conditions. It would be expected that the response of the device will change in these different conditions, so if no change in the form of the frequency dependence is seen it implies that the response of the device is not having an effect on the frequency dependence. The measurements were taken by mounting one of the FP cavity mirrors on a delay stage to allow precise variation of the distance between them and hence the frequency of the pulse train they produce. Signals were taken at different train frequencies and then the pulse associated with the acoustic response was integrated to find a value of the charge transfer in the device as described in section 5.3.3. As was discussed in section 5.3.2 the length of the pulse seen in the device is dependent on the frequency of the pulse train with longer pulses seen at lower frequencies. To account for this variation the window used for all the pulses was long enough to cover the low frequency pulse length. Any additional signal which is not part of the acoustic pulse which is included in the window should be removed by the fitting procedure previously discussed.

Error bars are not included on the graphs shown in this section, for clarity. To gain an appreciation of the variation possible it should be noted that when a measurement was made in the same conditions, i.e. same bias, same laser power and same frequency, at several different times throughout a day, the standard error on the mean of these values was found to be $\pm$ 14%. The relatively high error is thought to be due to the high sensitivity of the signal to drifts in the alignment of the laser spot relative to the device mesa. There is also a high probability of systematic errors in the frequency values. Although the separation of the moveable mirror from its zero point was precisely

controlled by a motorised delay stage, to an accuracy of 0.1 µm, there is a chance of error in the calibration of the separation between the two mirrors at this zero point. This will have a much larger effect on higher frequencies, where smaller distances between the mirrors are used. For instance at 100 GHz an error of 100 µm in the zero separation will contribute a 6 GHz error while at 10 GHz the error caused by this miss-measurement will be only 0.1 GHz. This level of error may be present in these graphs.

Figure 5.12 shows the charge transfer measured in the SL device opposite a film of an ≈100 nm evaporated onto an oxidised AlAs layer as a function of the frequency of the exciting laser pulse train in several different conditions. The sharp peaks seen in the dependence of the charge transferred in the device on train frequency will be discussed further later in this section.

In figure 5.12 it can be clearly seen that frequency dependence of the charge transferred due to the hypersonic excitation, is not dependent on the laser fluence incident on the transducer or the temperature of the sample. The electrical behaviour of the device is likely to be appreciably altered by a 95 K temperature increase. In a 400 µm mesa of the same wafer a 10% increase in resistance was seen when the temperature was increased from 10 K to 100 K. The lack of change between the two different temperature curves therefore suggests that the electrical behaviour of the device is the not the cause of the frequency dependence seen. The power in the pulse train will effect the level of the effective acoustic field created over the device again a factor which may alter the reaction of the device to the strain wave. Figure 5.12 shows that this has no effect on the frequency dependence, providing further evidence that the frequency dependence is caused by the output of the film.

Figure 5.13 shows the charge transfer measured in mesa 2 as a function of frequency in different conditions. This mesa is opposite an ≈50 nm aluminium transducer film. In this case, the curve measured when a bias of 300 mV was applied to the device and a total laser fluence in the pulse train of 7 mJ cm^{-3}

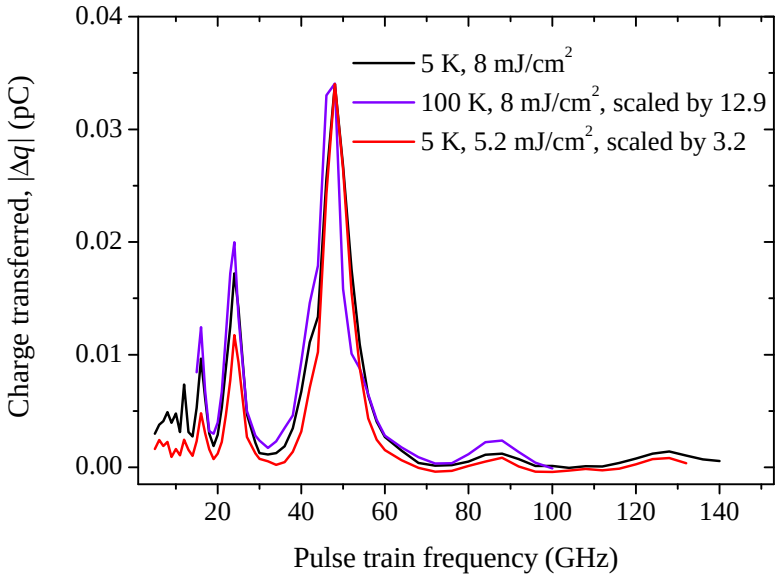

Figure 5.12: Frequency dependence of the charge transfer measured in the SL device opposite a film of an ≈100 nm evaporated onto an oxidised AlAs layer in different conditions, signal taken with mesa 4. All of these signals were taken when a bias of 200 mV applied to the device.

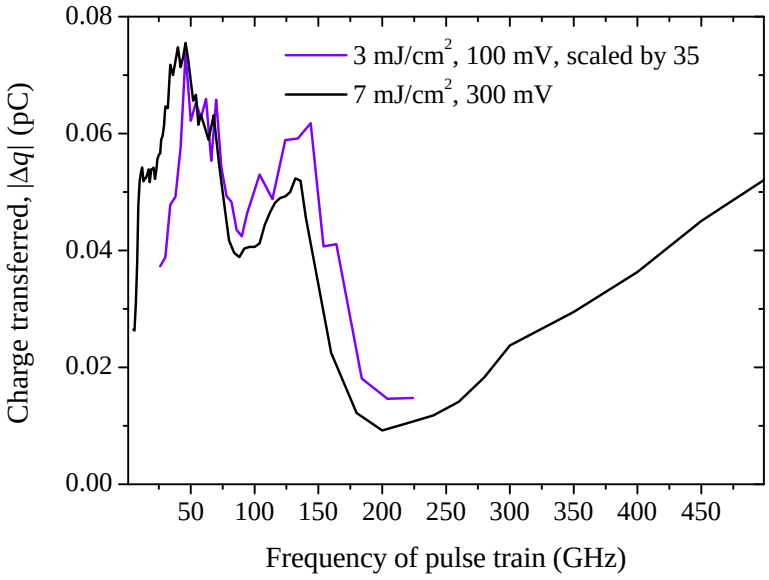

Figure 5.13: Frequency dependence of the charge transfer measured in the SL device opposite a film of an ≈50 nm in two different conditions, signal taken with mesa 2.

was used to excite the transducer, was repeated with a bias of 100 mV and an excitation of 3 mJ cm^{-3}. In figure 5.13 it can be seen that, despite the extremely different conditions the curves were taken under, they feature strong similarities, with differences likely caused by the high level of noise in the low power trace. The fact that the frequency dependence is not altered by these different conditions provides further evidence that it is due to the output of the film rather than variations in the detection sensitivity of the device.

If the frequency dependences seen are purely due to the output of the aluminium film when excited by the Fabry-Pérot cavity it should be possible to simulate these responses, combining a simulation of the cavity output with the pulses generated by the films. This will be the subject of the next section.

5.3.6 Simulations of the Frequency Dependence of the Output of the Transducer Films

The output of different aluminium films was simulated using an extension of the model described in section 3.4.3. Equation 3.1 was extended to include reflections of the generated strain at the interface with the sample as shown in equation 5.4.

$$\epsilon(t) \sim \sum_{j=0}^{\infty} (-R_I)^j \, (t - 2t_f) \, exp \left[- \left(\frac{t - 2t_f}{\tau_e} \right)^2 \right] \tag{5.4}$$

In equation 5.4 R_I is the reflection coefficient of the film/substrate interface and t_f is the time taken for longitudinal sound to travel through the aluminium film and τ_e is a parameter defining the width of the strain pulse, a discussion of the origin of this value can be found in section 2.3. The equation includes a summation over all pulses leaving the film, the attenuation between these pulses is set by the R_I with the minus included to represent a phase change occurring between pulses due to the multiple reflections. Acoustic mismatch theory predicts that this phase change will be necessary if the substrate has a greater acoustic impedance than the film. This simulated output of the film was then used to create a pulse train as in section 3.4.3 and the spectra of the trains at each frequency was integrated to obtain a measure of the energy at this frequency. As the charge transferred is dependent on the square of strain the signal measured by the device should be proportional to this value. The simulated output was fitted to the measured frequency dependences using the values of τ_e, R_I and the thickness of the film as fitting parameters.

Figure 5.14a shows the dependence of the acoustic response on train frequency for aluminium films with thicknesses of nominally 30 nm and 100 nm, both of these films were evaporated directly onto GaAs substrates. The curves displayed in figure 5.14a were both taken using pulse trains with a total energy of $7\,\mathrm{mJ\,cm^{-2}}$, on mesas with biases of 300 mV applied.

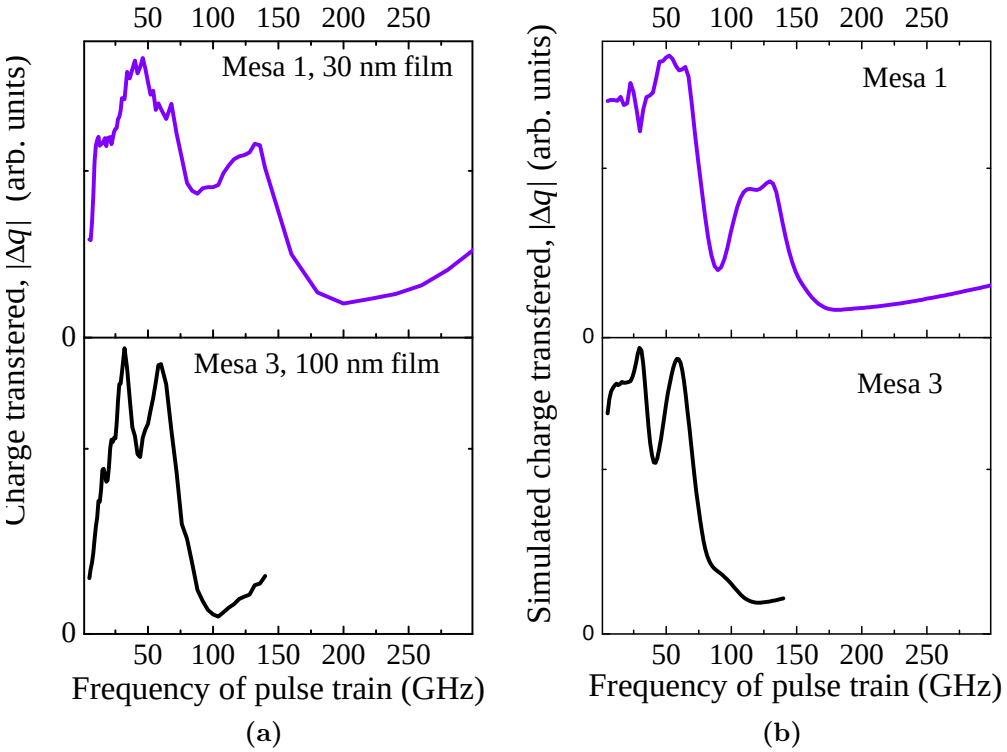

Figure 5.14: (a) The variation of the acoustic response with train frequency, measured in mesas opposite approximately 30 nm and 100 nm transducer films. Both of these traces were taken when a bias of 300 mV was applied to the devices and the total laser power exciting the aluminium film was 7 mJ cm^{-2} (b) Simulation of the data shown in (a).

Figure 5.14b shows the simulation of the results in figure 5.14a using equation 5.4, as an initial strain pulse for the train. A good agreement was found using the parameters $R_I = 0.43$, $\tau_e = 3.4\,\text{ps}$ and the film thickness $d_F = 44\,\text{nm}$ for the nominally 30 nm film. While the output of the nominally 100 nm film was found to be well produced with $R_I = 0.18$, $\tau_e = 5.5\,\text{ps}$ and $d_F = 78\,\text{nm}$. Both films were well reproduced using simulations which included a phase change of the pulse as would be expected in the case of an ideal interface in acoustic mismatch theory. There is some discrepancy between the experimental and simulated graphs, with the simulated results showing a greater magnitude at lower frequencies, than the measured. This may be due to the multiple harmonics in the cavity output at the low frequencies..

As was discussed in section 5.3.1, the figures quoted for the film thicknesses from the thickness monitor in the evaporator are not known to a high accuracy. The variations between these thicknesses and those found to fit the data in the simulations are therefore unsurprising. The value of τ_e is expected to vary somewhat between different films due to properties such as defect scattering in the film [92], but the values found here follow the expected trend with the thinner film having the shorter value. If the aluminium film is perfectly bonded to the GaAs surface it would be expected that the value of R_I could be determined from the acoustic mismatch between the two films as shown in the equation below,

$$R_I = \frac{Z_2 - Z_1}{Z_2 + Z_1}, \tag{5.5}$$

For this experiment Z_1 is the acoustic impedance of aluminium and Z_2 is the acoustic impedance of GaAs. This equation was also shown in section 2.3 and is repeated here for clarity. The value obtained for R_I using equation 5.5 is 0.18, a good match for the thicker film, however the value for the thinner film is much higher than this. It has been shown that higher reflection coefficients can be found in cases of poor adhesion of a film to the surface [3,97], this could be the case for this film. The frequency dependences of the acoustic signals measured using the weakly coupled SL sample are therefore well reproduced with reasonable values of fitting parameters by a simulation assuming no

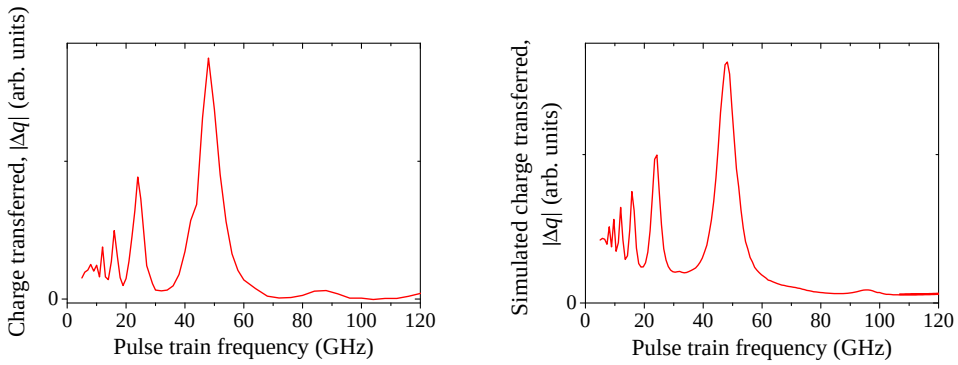

Figure 5.15: (a) The variation of the acoustic response with train frequency, measured using mesa 5 on a sample which is believed to include a roughened AlAs layer, under the transducer film. The data was taken with a bias of 200 mV applied to the mesa and a total laser excitation power of 8 mJ cm^{-2} (b) Simulation of the data shown in (a).

frequency dependence of the response of the device. This supports the theoretical description.

There was one sample of MN796 which produced very sharply defined peaks in frequency with a high contrast between the signal on and off resonance. A frequency dependence measured using an ≈100 nm film transducer on this sample is shown in figure 5.15a. Figure 5.15b shows that a simulation of this data using the method outlined above, with $R_I = 0.45$, $\tau_e = 6.4$ ps and $d_F = 67$ nm. For this simulation a better reproduction of the experimental results was found when no phase change was included between reflections out of the aluminium film. A set of peaks seen in both the experimental and simulated data occur at train frequencies of 12,16,24 and 48 GHz. If the film thickness found from the simulation, 67 nm, is taken, it is found that the fundamental frequency for standing waves in this film will be 48 GHz, suggesting the film is acting in a similar manner to a free standing membrane [2]. The presence of the first 3 divisors of this frequency may be a consequence of the Fabry-Pérot cavity method, where as was discussed in section 3.4.3, due to the generation of harmonics of the frequency the cavity spacing is set

for, a higher frequency can be well produced by its divisors.

The interpretation given of the frequency dependence shown in figure 5.15a implies that the bonding of the film to the sample in this case was extremely poor. The film used to obtain the results shown in figure 5.15 was later removed from the sample and a new thicker film was applied. This produced similar results but with a lower fundamental frequency. Suggesting the poor bonding was a result of the surface of this particular chip. The sample MN796, which was used for this study was initially developed for coherent phonon optics experiments as described in chapter 4, and as such, featured a *p-i-n* device on the reverse side to the SL device. In preparation for the experiments detailed in this chapter the *p-i-n* side of the sample was etched to remove this structure. It is believed that the poor adhesion of transducer films to this sample are due to the etch leaving an AlAs layer from the *p-i-n* structure exposed. Aluminium is a highly reactive metal and it is known that it quickly forms a several nanometer thick oxide in atmospheric conditions. The exposure of the AlAs layer to atmosphere before the evaporation of the Aluminium film over the reverse side of the sample may have therefore led to the formation of an roughened layer under the film, leading to poor film adhesion and the frequency dependence in figure 5.15.

To test the hypothesis that the roughening of the surface through oxidisation could cause this poor adhesion, an experiment was performed where a layer of aluminium was evaporated on the GaAs substrate then allowed to sit in atmospheric conditions for ≈4 h. A further layer of aluminium was then evaporated on the sample, creating a sandwich film with two layers of aluminium separated by an oxide layer. The frequency dependence of the output of this double film transducer is shown in figure 5.16. In this figure we see that the output of this sample is significantly different from that produced by other films evaporated directly on GaAs substrates, such as those shown in figure 5.14. This suggests that the oxidisation of the first film has a significant effect on the bonding of the second film. Previous works, which have studied these effects in detail, have found that interfaces such as the one produced

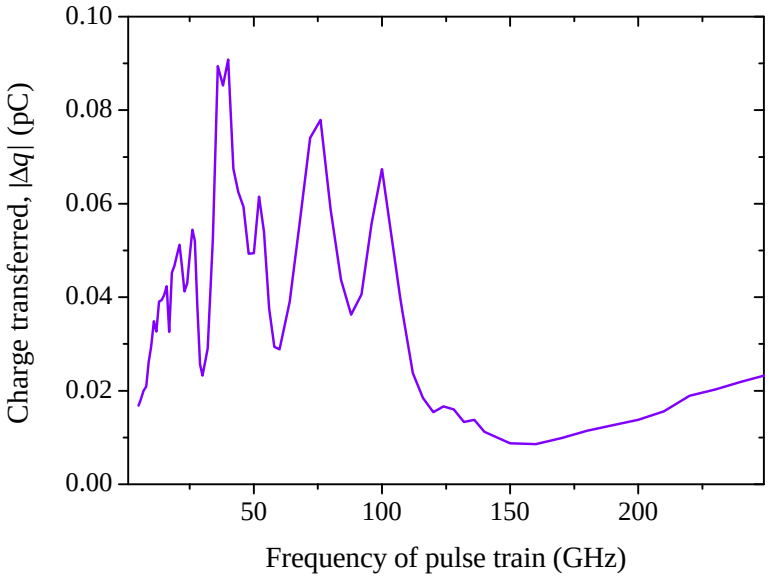

Figure 5.16: Frequency dependence of the charge transfer measured in the SL device opposite a double film incorporating a 60 nm film deposited on a 50 nm film which was left in atmospheric conditions for 4 h. The signal was taken with mesa 6, with a bias of 300 mV applied, using an excitation density of 7 mJ cm^{-2}.

here may produce a strong softening of the elastic constants [5, 134]. This supports the explanation for the frequency dependence seen in the previous sample, figure 5.15, which was given above. Suggesting that even the dramatic frequency dependence seen in figure 5.15a is not related to the response of the device.

5.3.7 Single Pulse Excitation

The theory described in section 2.2.3 was developed for the case of acoustic excitation of the whole SL with a wave of single frequency. It is therefore unlikely to provide a good description of the excitation of the SL with a single pulse. Even in the case of a thick aluminium film, where the whole acoustic pulse may have a temporal width 18 ps only 115 nm, $\approx 20\%$ of the SL, will be

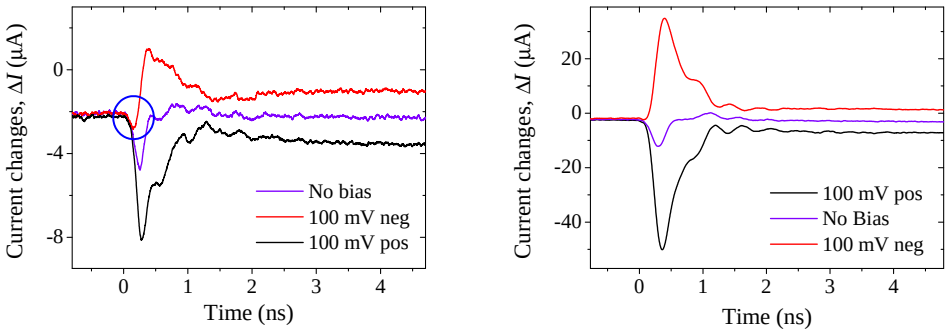

(a) Signal without FP cavity **(b)** Signal with cavity at 46 GHz

Figure 5.17: Signal detected with mesa 4 , which featured a 100 nm film on an oxidised AlAs layer, with and without the FP cavity present in the laser path.
(a) Signal without cavity, measured with Laser fluence 4 mJ cm^{-2}.
(b) Signal with cavity set to 46 GHz, measured with with Laser fluence 7 mJ cm^{-2}. Data was previously shown in figure 5.4.

effected by the pulse at a time. Also, as was discussed in section 3.4.3, a single pulse features a broad range of frequencies centred on the one characteristic of the pulse width, and is not a good approximation to a monochromatic wave.

Figure 5.17a shows the signal measured using mesa 4 with single pulse excitation, while figure 5.17b shows the signal measured using mesa 4 with 46 GHz excitation from the FP cavity for comparison. The data in 5.17b was previously shown in figure 5.4 but has been repeated here for ease of comparison. In figure 5.17 it can be seen that the signal seen without the FP cavity shows a decrease in current due to the acoustic excitation compared, in the same way as the signal excited by the cavity. However, the effect of the bias on the signal when it is excited without the cavity is much smaller, than with the cavity. It can also be seen in figure 5.17a that the signal excited by the single pulse features a small negative pulse before the main signal in the trace with the negative bias applied this is highlighted by the blue circle. It is possible that this is a signal from the contact layers in the device, which is not visible when the cavity is present due to the stronger response from the

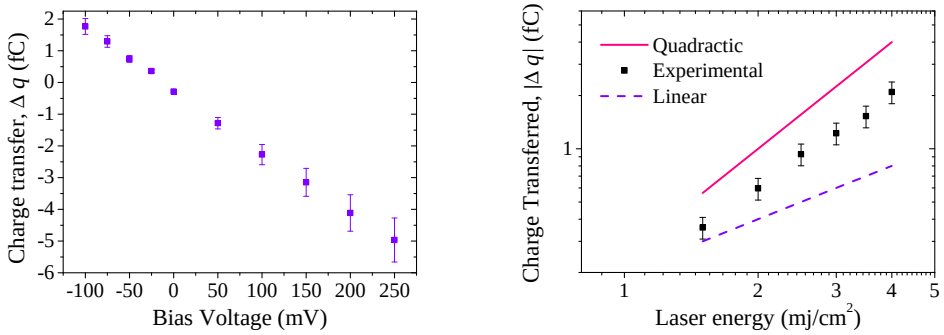

(a) Signal without FP cavity **(b)** Signal with cavity at 46 GHz

Figure 5.18: Variation of signal in mesa 4, when excited with a single laser pulse.
(a) Variation of signal in mesa 4, with bias applied to the mesa, signal taken with a laser power of $4\,\mathrm{mJ\,cm^{-2}}$ in a single pulse.
(b) Variation of signal in mesa 4 with energy of the exciting laser pulse, signal taken with no bias applied to the device mesa.

SL to the bias.

The variation of the signal in mesa 4 under DC bias, when it is excited by a single acoustic pulse, is shown in figure 5.18a. The variation with bias is, to good approximation, linear in agreement with the trend seen when the sample was excited with a pulse train from the Fabry-Pérot cavity in the laser path. The variation of the signal seen with the energy of the single pulse laser excitation is shown in figure 5.18b. Again it is in general agreement with the trend seen when the FP cavity was used, A power law fit to this data gives a power of 1.6 ± 0.1. Although, it should be noted the energies shown in figure 5.18b are all concentrated in a single pulse rather than being split between pulses as in the cavity case. At these levels of excitation it is therefore possible that the strain may start to exhibit non-linear effects when propagating through the GaAs substrate.

The behaviour of the sample when excited with single acoustic pulses is largely similar to the behaviour when excited with the pulse train although the bias produces a weaker increase in the size of the hypersonic response

seen, over the response without bias. This may be due to a combination of the facts that the energy of the exciting pulse is split between a number of different frequencies, and that the the length of the pulse is such that it is only exciting $\frac{1}{5}$ of the device at any one moment. This shorter excitation length means the signal is shorter compared to the electronic rise time of the circuit resulting in it appearing smaller when integrated over this time. This suggests that mechanism of the response of the sample to a single acoustic pulse may not be so different to the response to a pulse train. It is possible the two situations may be described by the same theory with an extension to include the effect of multiple frequencies.

5.4 Other Samples

The sample investigated so far, MN796, has been shown to act as an efficient hypersonic transducer for GHz frequency acoustic waves and be well described by a theory relating the current seen to the stimulation of tunnelling events within the device. To further understand if the phenomena seen in this sample were unique to weakly coupled SLs a brief investigation of some different samples was conducted. The samples used in this investigation were processed into 100 µm mesas and measured using acoustic excitation with the Fabry-Pérot cavity in the same manner as was used for sample MN796. Details of the samples can be found in section 3.3.2.

5.4.1 RC04

Figure 5.19 shows the I-V characteristic and acoustic response of sample RC04. This sample featured a 490 nm GaAs layer which was doped to levels of $2 \times 10^{17}\,\mathrm{cm}^{-2}$, between two 500 nm GaAs contact layers. This sample is not expected to produce the sequential tunnelling events which were the basis for the theory described in section 2.2.3.

As can be seen in figure 5.19a, the sample features an ohmic *current-voltage* characteristic as would be expected, for a plain layer sample. It is therefore not expected that there would be any signal which could be described by the theory discussed in section 2.2.3. Since the signal described in this theory is reliant on the non-linearity of the I-V curve, of which there is none in this sample.

The signal seen at the time associated with the arrival of longitudinal phonons after a journey through the sample substrate is shown in figure 5.19b. This is identified as the response of the sample to the coherent strain pulse, it can be seen that this response is only weakly dependent on the DC bias applied to the device mesa, with a slight decrease in signal seen when bias is applied. Previous work with similar samples saw a signal which was attributed to charge carriers being trapped in a potential well formed by the strain pulse and dragged through the doped layer [129]. It is likely this is the source of the current signal seen in this device. The signal seen is predominantly positive, as would be expected for this case when electrons are dragged from the ground of the device towards the top contact. Comparing the signal seen in figure 5.19 with that in 5.17b, it can be seen that the change in the acoustic response in sample RC04 when a bias is applied is much smaller than was seen in MN796, suggesting a different mechanism for the response in this sample.

Figure 5.20 shows the dependence of the signal in RC04 on the total energy of the exciting laser pulse train. This signal was found by integrating the acoustic response and also integrating a background window to remove this signal in a similar manner to that used for sample MN796. No strong response to the heat pulse was seen in this sample so no fitting was used for this. It can be seen in figure 5.20 that dependence of the signal in RC04 on laser energy is non-linear, here fitting gave a value for the power of 3.2 ± 0.2. This is further from quadratic than was seen in MN796 further suggesting a different mechanism of the response in this sample.

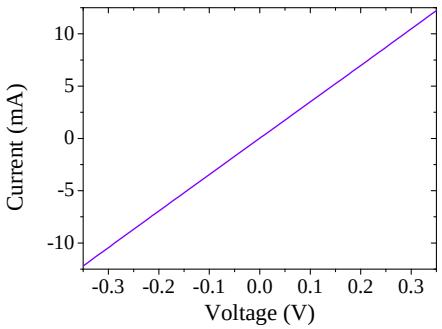

(a) I-V measurement of sample RC04

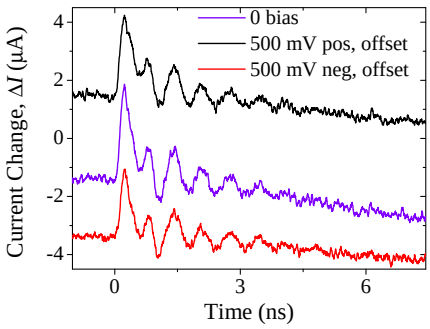

(b) Acoustic response of sample RC04

Figure 5.19: (a) I-V measurement of sample RC04, performed at 5 K. (b) Example of acoustic response of sample RC04, the signal was taken using laser excitation with a total energy of 8 mJ cm^{-2} in a 44 GHz pulse train. a 100 nm aluminium film transducer was used. Offsets have been applied to the signals with bias for clarity.

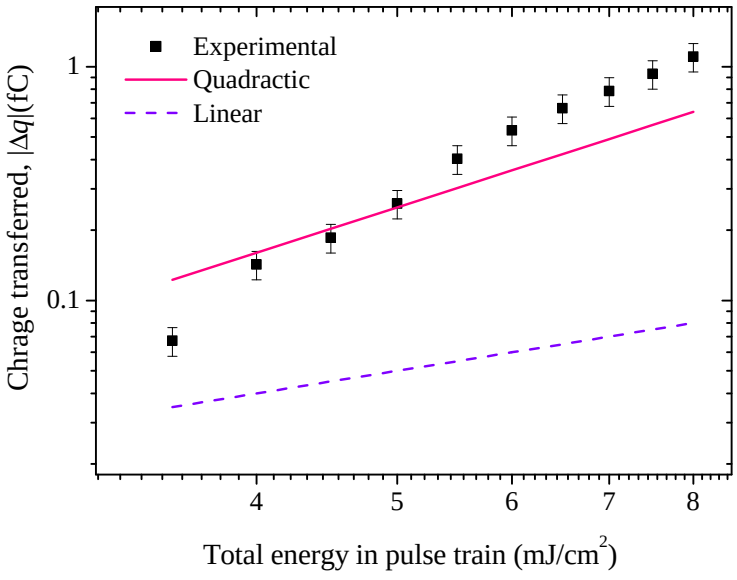

Figure 5.20: Dependence of the charge transferred in sample RC04 on the energy of a laser pulse train exciting a 100 nm aluminium film transducer opposite the device. The signal was taken using a train frequency of 44 GHz. No bias was applied to the device while the signal was taken.

5.4.2 NU2299

Sample NU2299 featured a semiconductor SL formed of 10 nm, GaAs wells and 2.5 nm, $Al_{0.7}Ga_{0.3}As$ barriers. Previous work on this SL [135] has suggested it features strong coupling between the wells and therefore may be described by tunnelling in a miniband below voltages at which domains form [51]. This kind of tunnelling can be considered to take place coherently between many wells at a time, as opposed to the series of independent sequential tunnelling events expected in weakly coupled SLs like MN796. The initial theory developed by Tucker was formulated for the case of a series of independent tunnelling events. It is therefore possible that the adaptation of it used in this work will not describe this SL.

Figure 5.21 shows the stationary I-V measurement for a 100 µm mesa made from wafer NU2299, measured at 5 K. It can be seen that the I-V characteristic is highly asymmetrical with the domain region starting in the device almost instantly on the negative side of the I-V but not till 300 mV in the positive direction. For the same reasons as were discussed for the case of sample MN796, the weakly coupled SL, the investigation will focus on areas below this region of domain formation.

A fit to the I-V using equation 5.2 is also shown in figure 5.21,. This fit shows a good agreement to the data, using the fitting parameters a =0.5371 S and b =−0.1875 S V^{-2}. These are similar to the values used to fit the I-V of sample MN796, which implies that if the theory described in section 2.2.3 is valid for this sample equation 5.3 should be valid and the device should respond to hypersonic excitation in a similar way to sample MN796. However as is shown in figure 5.22 the behaviour of this sample when a DC bias of less than the domain threshold is applied to the device is very different to that seen in sample MN796.

Figure 5.22 shows the signal seen at the time of flight for longitudinal acoustic phonons through the film, which is associated with the acoustic

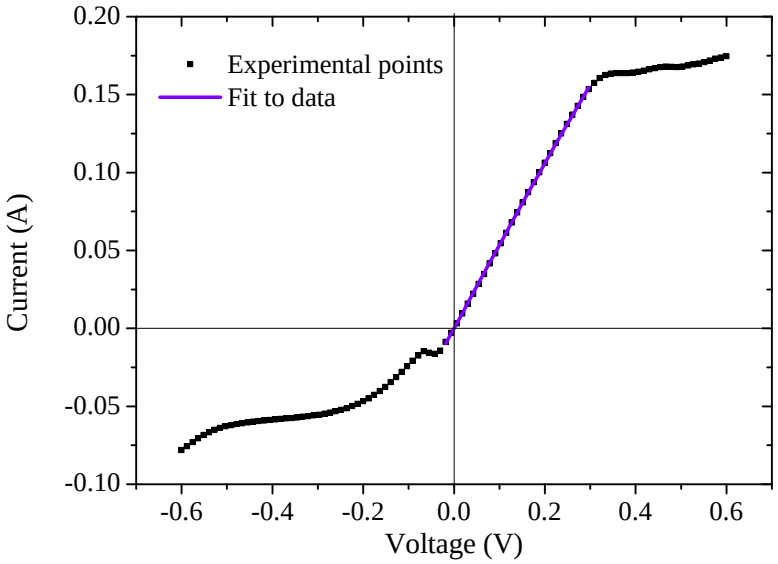

Figure 5.21: *I-V* measurement of sample NU2299, performed at 5 K. A fit to the more linear part of this I-V, using equation 5.2 is also shown.

response. This acoustic response signal is also shown when a positive DC bias is applied to the device mesa. No signal is shown for the application of a negative bias because the sample goes into a domain region at very low biases in that direction. It can be seen that the application of bias to the device causes a small decrease in the magnitude of the signal seen, similar to the case of the plain doped layer, figure 5.19b. This may imply that the acoustic response seen in this sample is also the result of a phonon drag effect. Electrons within the miniband of an SL are known to act in a similar manner to electrons in a band in a semiconductor structure [51,52,63]. Which supports the idea of a similarity between the response to acoustic waves, in a strongly coupled SL and a plain layered sample.

The dependence of the acoustic response on the laser energy of the acoustic pulse train is shown in figure 5.23. This graph was formed by integrating the current response measured on the oscilloscope to find the magnitude of the charge transferred for each energy of the laser pulse train in the same

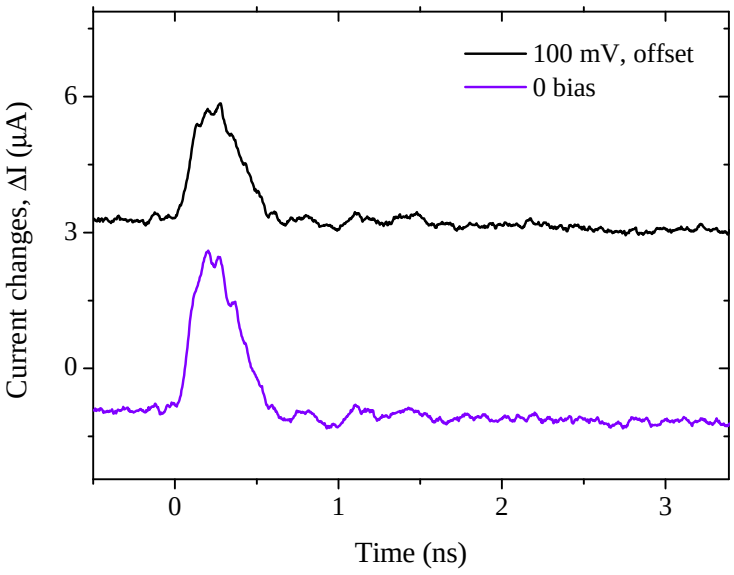

Figure 5.22: Example of acoustic response of sample NU2299, the signal was taken using laser excitation with a total energy of 9 mJ cm^{-2} in a 25 GHz pulse train. A 100 nm aluminium film transducer was used. An offset has been applied to the signal with bias for clarity.

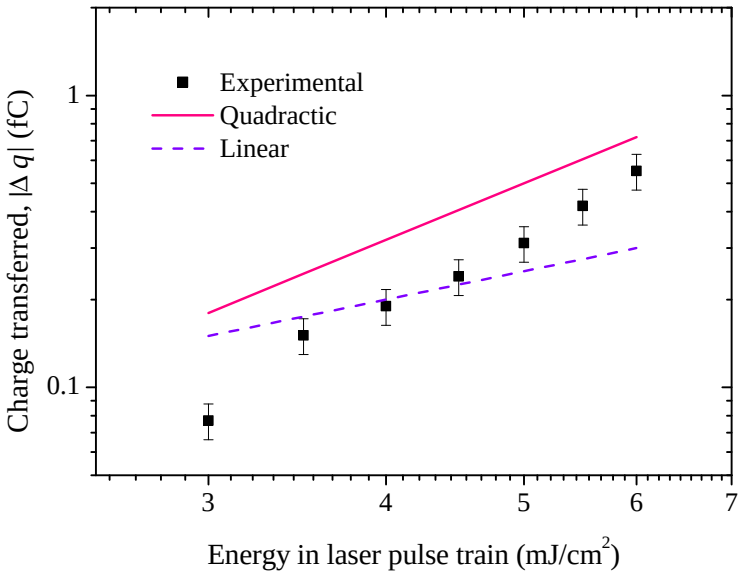

Figure 5.23: Dependence of the charge transferred in sample NU2299 on the energy of a laser pulse train exciting a 100 nm aluminium film transducer opposite the device. The signal was taken using a train frequency of 25 GHz. No bias was applied to the device while the signal was taken.

way as was investigated in samples MN796 and RC04. The acoustic response was investigated using a 25 GHz pulse train to excite a 100 nm film. It can be seen in figure 5.23 that the response variation of the signal with laser excitation power is found to be non-linear, as it was in the weakly coupled SL and the homostructure sample. Here a power law fit was found using the power 2.6 ± 0.2. It seems that this non-linearity in the acoustic response is a common trait to many different forms of semiconductor samples.

This sample does not seem to be well described by the theory detailed in section 2.2.3, with the variation of the acoustic response with bias not following the predicted trend. This is expected due to the difference in transport in a strongly coupled SL compared to a weakly coupled one.

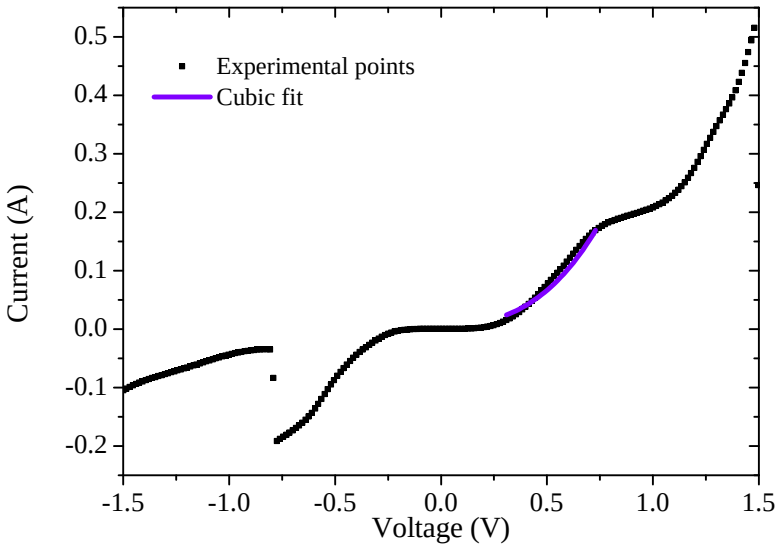

Figure 5.24: (a) *I-V* measurement of sample NU2299, performed at 5 K. A fit to a section of this I-V, using equation 5.2 is also shown.

5.4.3 NU1778

The final sample investigated was NU1778 this featured a SL incorporating the same well and barrier widths as, MN796, the sample which was the main subject of this investigation. This makes it likely this sample can also be considered as a weakly coupled device with transport expected to occur through a series of sequential tunnelling events. This sample differs from MN796, in two ways. Lower levels of doping were included in this SL, with the doping used in the wells being only of the level of $1 \times 10^{16}\,\mathrm{cm}^{-2}$ and the barrier $2 \times 10^{16}\,\mathrm{cm}^{-2}$, while in MN796 these values were of the order of $10^{17}\,\mathrm{cm}^{-2}$. The SL also featured only 10 periods making the total length of the SL only 98 nm, while MN796 was 490 nm in length, featuring 50 periods. The sample was investigated in the same way as the other three samples.

Figure 5.24 shows the *I-V* characteristics of this device, taken at a temperature of 5 K. It can be seen that, despite both having the same SL structure,

there are strong differences between the I-V characteristic of this device and the I-V characteristic of sample MN796 (figure 5.3). Figure 5.24 shows that sample NU1778 does not begin to conduct current until a certain voltage is reached, around 140 mV in the positive direction and −114 mV in the negative. This voltage threshold behaviour, has been seen in previous SL structures with lower doping and is associated with the voltage required to align the emitter contact with the 1^{st} quantum well in the SL [58]. This sample also features an undoped spacer layer between the contacts and the SL which will probably contribute to this threshold. After the threshold is passed the current in the device increases up until 800 mV in the positive direction and −700 mV, in the negative at which point it starts to plateau. The saw-tooth like current structure which was seen within this plateau for MN796 is absent in this device. This is likely due to the lower doping levels which have been shown to prevent the pinning of the domain wall necessary for this saw-tooth structure to be present [74]. It is presumed that the device could be described as featuring sequential tunnelling in the region between the device turn on and this plateau, although there is no sharp edge to the plateau in this device. An attempt to fit this region on the positive side of the I-V with the cubic fit defined in section 2.2.3 was made and can be seen in figure 5.24, using values of $a = 4.491 \times 10^{-5}$ S and $b = 3.52 \times 10^{-4}$ S. The equation used does not produce a good agreement with the experimental data using a least squares fitting approach through the curve fitting toolbox in the technical computing language Matlab. From this fit it does not seem that equation 5.3 is likely to be a good description of the acoustic response.

The acoustic response seen when sample NU1778 is excited by a 30 GHz laser pulse train is shown in figure 5.25. The response seen in this sample is very weak, with nothing distinguishable above the noise level of the trace in the 0 bias case. However, when a DC bias is applied to the device a signal does appear. This large increase in response when bias is applied is similar to the behaviour seen in sample MN796, the other weakly coupled SL sample, however it can be seen that the signal in this case represents an increase in the current when the acoustic pulse is present compared to without, whereas

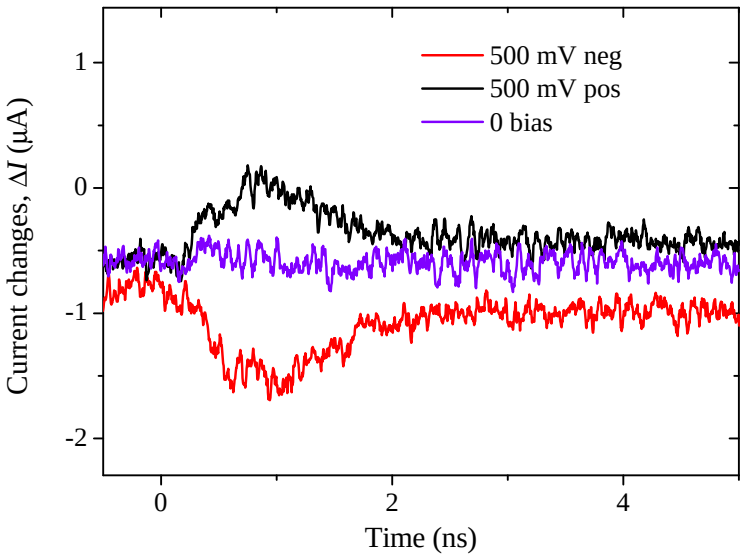

Figure 5.25: Example of acoustic response of sample NU1778, the signal was taken using laser excitation with a total energy of 8 mJ cm^{-2} in a 30 GHz pulse train. A 100 nm aluminium film transducer was used.

in MN796 a decrease was seen. According to the theory presented in section 2.2.3, this difference in sign should be explained by the shape of the *I-V* curve. The fit shown in 5.24 does produce a different sign to the fit of MN796, figure 5.10, however since it makes a poor approximation to the results further investigation would be required to ascertain if the change of acoustic response polarity could be explained by the theory detailed in section 2.2.3.

The low amplitude of the signal compared to that seen in MN796 is not unreasonable considering the shorter SL and the low carrier density. The temporal length of the acoustic response is longer than may be expected due to the short SL in this case. The distance from the lower edge of this SL to the surface of the sample is ≈640 nm, whereas for sample MN796 it was ≈780 nm, which might suggest that if device length where the only factor in determining hypersonic response length this sample should feature a shorter response. The high level of noise and small signal make comparison of the pulse shape difficult. However, in figure 5.26 it can be seen that the pulse-width does vary with frequency in a similar way to seen in MN796. This shows that the response time is related to the time the acoustic pulse train is present in the sample for, however the response features a more significant lengthening compared to the pure time of flight than MN796. This is likely caused by the higher resistance of the device increasing the RC constant of the detection circuit which will broadening the response.

The dependence of the acoustic response seen in the device on the total energy in the acoustic pulse train was measured by integrating the signal in the window where the acoustic response was present and making a comparison between the charge seen in this window and the charge seen in a background window of the same size placed just before the acoustic pulse. No fitting was used as no strong heat pulse response was seen in this device. The variation seen is shown in figure 5.27. A non-linear response is seen, this is similar to the response seen in the other samples, Here a power law with a power of 2.5 ± 0.1 was found. This may be explained by the theory proposed in section 2.2.3, however since it was also present in other samples it may be that this is

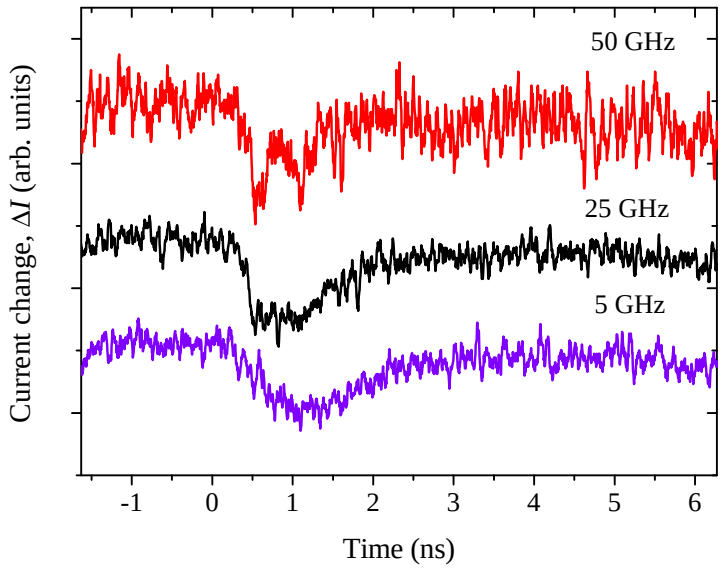

Figure 5.26: Dependence of the temporal shape of current response in sample NU1778 on the frequency of the acoustic pulse train. Signals taken with with a dc bias of −700 mV applied to the device

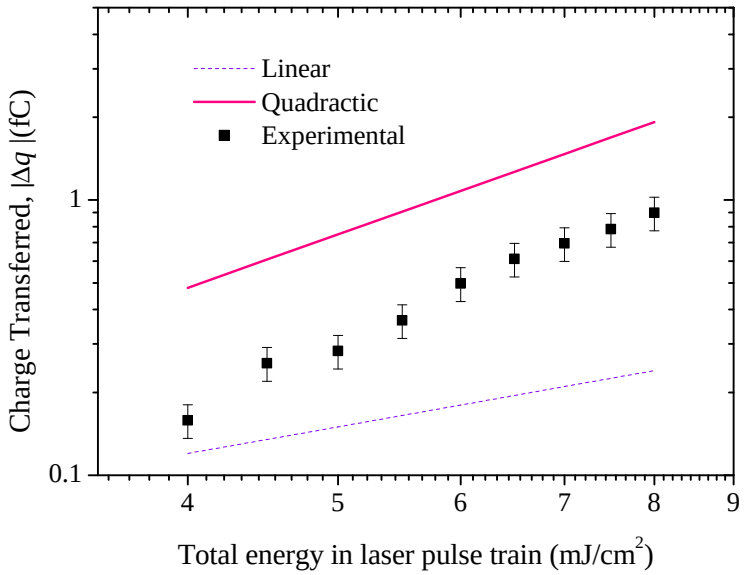

Figure 5.27: Dependence of the charge transferred in sample NU1778 on the total energy in the acoustic pulse train. Signal was taken with −700 mV of bias applied to the device while using a 100 nm transducer film. The frequency of the applied pulse train was 30 GHz

some more general feature of the acoustic response of semiconductor samples to strain pulses.

The response of this weakly coupled SL to the acoustic pulse train seems to feature more similarities to response seen in the weakly coupled SL that the theory was developed for than the plain GaAs sample or the strongly coupled SL. This is as would be expected since the theory was developed for the case of a sample featuring sequential tunnelling events, which is most likely to be true for the weakly coupled SL samples of the devices studied. The I-V of the NU1778 was not well reproduced by the fit used to describe the I-V of sample MN796, a more sophisticated model of this I-V maybe be required to fully explain the results.

Also briefly investigated was MN685, this sample was grown to the same specifications as MN796, only on a thicker substrate. The behaviour of this

sample was not seen to be any different to that in MN796 confirming that the size of the substrate had no effect on the signals seen.

5.5 Conclusions

The acoustic response of a weakly coupled semiconductor superlattice to hypersonic excitation was investigated. An acoustic pulse train was created by the excitation of an aluminium transducer film with the laser output of a Fabry-Pérot cavity. For frequencies in the tens of GHz this enables a, close to monochromatic acoustic excitation of the SL. The temporal length of the acoustic response of the SL was seen to increase with decreasing train frequency confirming that the acoustic response was caused by the train passing though the SL. At frequencies of between, approximately, 30 GHz and 100 GHz the length of the acoustic response was not found to be related to train frequency, suggesting the train length was comparable to device length and the whole train was present in the device at one time.

The device produced a rectifying response with changes in the current of 3% produced by the acoustic wave. The variation of the magnitude of the acoustic response in the SL device as the DC bias applied to the device was varied, and as the total laser power in the exciting train was varied, was studied. The trends in magnitude seen were compared to the prediction of theory developed in section 2.2.3 with good agreement. This theory predicts that the device response should be independent of the exciting train frequency. This prediction was tested by comparing the frequency dependence of the same films when measured in different conditions. No change was found in the frequency dependencies, in agreement with the theoretical prediction. The dependence of the signal seen as a function of frequency was then studied for several different devices and it was found that these dependences could be fitted using a model related purely to the output of the aluminium film. Further confirming the prediction that the device response was not the cause

of any frequency dependence seen.

The response of the weakly coupled SL device to a single pulse excitation was compared to the pulse train excitation results and the rectification effect was found to be weaker in this case, with the current change cause by the hypersonic excitation only being 0.4%. The qualitative behaviour of the device was however found to be similar suggesting that perhaps an extension of the theory developed for the case of excitation with a wave of a single frequency could be used to describe both cases.

The theory in section 2.2.3 was developed using a basis of sequential tunnelling in a weakly coupled SL. Two samples where sequential tunnelling was not expected, a potentially strongly coupled SL and plain doped layer were briefly investigated. These were found to exhibit very different behaviour when the acoustic response was measured with a DC bias applied to the device to that seen in the weakly coupled SL. This suggests that a different model is necessary to describe the behaviour of devices not exhibiting sequential tunnelling as would be expected. Also investigated was a second weakly coupled SL with differing parameters to the one which formed the main subject of this investigation. This device exhibited behaviour more akin with that of the other weakly coupled SL, however the different I-V properties of this device will require a more sophisticated fit than was used in the first sample for a full description.

In conclusion it has been shown that a weakly coupled SL forms an effective acoustic transducer for acoustic pulse trains of tens of GHz. This suggests the possibility of conversion between acoustic and electromagnetic signals in the device. The DC component of the current response was the subject of this investigation. However, in analogue with the electromagnetic excitation that the theoretical description of this work was modelled on, an AC current response should also be present [52]. This may be interesting for device applications and will be further discussed in chapter 6.

Chapter 6

Conclusions and Further Work

This chapter will summarise the experiments which have been detailed in this thesis and the main conclusions which can be drawn from them. Possibilities for future research as a result of these findings will then be discussed.

6.1 Conclusions

The work detailed in chapter 4 has shown the possibility for the active control of a phonon signal through the application of an electrical bias to a semiconductor superlattice structure. An experiment was designed using a phonon chip. This incorporated a transducer SL to generate the coherent phonons, an active SL device where bias could be applied and a coherent phonon detector in the form of a *p-i-n* photodiode [29]. The active SL structure was grown using similar specifications to those of devices which had previously shown evidence of electrical control of the phonon amplitude through an interaction attributed to saser theory [58, 60]. The detection and control structures were grown on opposite sides of a semiconductor substrate, and processed to allow the application of electrical bias using the techniques

detailed in section 3.2. The devices were mounted on a holder allowing an electrical bias to be applied to both sides simultaneously. A *pump-probe* experiment was used to investigate the output of the superlattice structure when it was excited by femtosecond laser pulses. The effect of applying bias to the active SL on the phonon beam passing through it was investigated through the use of a bias modulation experiment.

A small, 0.14%, attenuation of the phonon signal was seen when an electrical bias was applied to the active SL device. Possible causes of this attenuation were discussed. It was found that the behaviour of the device was consistent with the predictions of saser theory for the case of a structure with the doping levels used in these experiments, which were higher than used in previous devices. The possibility that the attenuation was caused by increased electron transitions due to electron heating was not ruled out. One of the aims of this experiment was to find out more about the possibility of phonon interactions in this structure and the suitability of the active SL as a saser gain medium. It was found that the high doping levels used in this device did not function well as a saser device. However the technique was found to be a very sensitive test of potential phonon devices. With the potential for detailed studies of phonon effects in other structures.

The work detailed in chapter 5 has shown the potential for a doped weakly coupled SL to act as an efficient transducer for the conversion of acoustic waves to electrical signals. The effect was investigated by measuring the response of the SL to acoustic strain pulses generated by exciting an aluminium film transducer with pulses from an amplified Ti:Sapphire laser. A Fabry-Pérot cavity was used in the laser beam to create a train of pulses. Details of the acoustic output of an aluminium film transducer when excited using a pulse train created by this cavity are given in section 3.4.3, it was found this can simulate the action of a monochromatic acoustic wave at frequencies between approximately 30 GHz to 100 GHz. The response of the SL device as the pulse train moved through it was measured directly using a digital sampling oscilloscope with an analogue bandwidth of 12.5 GHz.

It was found that the acoustic pulse length in the device was governed by the frequency of the strain pulse train and its time of propagation through the SL. This suggests the possibility of acousto-electrical conversion in the sample enabling the creation of electrical waves at frequencies defined by the pulse train frequency. The action of the acoustic wave on the SL device was compared to the response predicted by a theory of the electron-phonon interaction in a weakly coupled SL developed for this work by Dr. Alexander Balonov. This theory is based on initial work by Tucker [85] which has been adapted to the case of irradiation of weakly coupled SLs by terahertz EM waves by Keay et al. [88] and is detailed in the review of transport in SLs by Wacker [52]. For the investigation detailed in chapter 5 the theory was further adapted to the case of the excitation of a weakly coupled SL with an acoustic wave. The theory correctly predicted the quadratic dependence of the magnitude of the acoustic response measured in the SL on the strain applied to the device and, the linear dependence of the magnitude of the acoustic response seen on bias applied to the device.

The theory also predicted that the response of the SL device to the strain should not be dependent on the frequency of the exciting wave. To test this prediction the frequency dependence of the output of a number of aluminium films was measured. These results were simulated, using a simulation of the output of the aluminium film when excited by the Fabry-Pérot cavity. The thickness of the films, the width of the strain pulse produced by them and the reflection between the film and the substrate interface were used as fitting parameters. Good agreement was found between the simulated and measured results, further validating the approach used in the theory. A brief review of the response of some different semiconductor samples to the acoustic pulse train was made. These samples were not found to exhibit responses which were well described by the theory, as is expected since this theory was developed for the case of a weakly coupled SL so would be expected to produce the response of devices with different transport properties less well.

6.2 Future Research

6.2.1 Investigation of Further Devices with the Coherent Optics Method

The experiments detailed in chapter 4 showed that it is possible to make a coherent optics chip which provides a sensitive measurement of the acoustic output of a device. In these experiments, this chip was used to measure the effect of a single pass through a highly doped active SL. The effects which were seen were smaller than initially expected for reasons attributed to the high doping level in the structure. A test of this hypothesis would be to repeat the experiment using an active SL with lower doping levels.

Another device which may produce an interesting effect on a propagating strain pulse is the double barrier resonant tunnelling diode. As was discussed in chapter 1, previous experiments on this device have shown it to exhibit a strong sensitivity to strain [49]. The sensitivity to strain in the device was attributed to charge transfer through an acoustic pumping effect. The device experiences a resonant peak in current at the bias value which aligns the energy level in the quantum well with the emitter level in the structure. It was possible for the acoustic pulse to allow the flow of charge through the otherwise insulating device at biases close to this resonant peak by shifting the energy levels of the QW bringing the device into resonance. At other biases the strain pulse moves through without the transfer of charge. An interesting experiment may be to measure any differences seen in the strain pulse after propagation through the device at a bias where it is transferring charge compared to at a bias without. Of particular interest may be holding the device at a bias on the edge of the resonant peak and monitoring any amplitude change caused to the strain pulse by the acoustic pumping which occurs at this bias. The work presented before suggested that when the device is biased on the threshold of the resonant peak only one half of a bipolar strain

pulse will be able to induce charge transfer. This would perhaps lead to the possibility of an electrical control of the acoustic pulse shape. The experiment should also improve our understanding of the mechanism of electron-phonon interactions in these tunnelling heterostructures.

Such an experiment could be performed by growing a RTD device on one side of the substrate and a *p-i-n* on the other. A photocurrent *pump-probe* experiment could then be performed as detailed in section 3.10. However, initially instead of using a SL transducer as in the experiments in chapter 4, a metal film transducer could be used to generate a strain pulse which will then travel through the RTD. The metal of the device contacts could be used for this, or the device could be processed in an optical access mesa like in the SL devices and an aluminium film evaporated over this optical access. Then any effects on the strain pulse due to changing the bias on the RTD could be investigated. The effect on the quasi-monochromatic wave from a SL when moving through the device may also be interesting.

6.2.2 Application of Coherent *p-i-n* Photodiode Detection to Transverse Phonons

All the experimental work detailed in this thesis so far has been conducted using (100) GaAs substrates. In this orientation, in experiments such as detailed here with a spot size which is much larger than the penetration depth of the laser, coherent shear waves are not generated [136]. However for samples grown on low symmetry planes of GaAs, such as (311), the opportunity for the generation of coherent transverse phonons exists, due the different symmetry considerations of the crystal in this orientation. Transverse acoustic waves would have advantages for use in picosecond acoustic experiments due to their shorter wavelength compared to longitudinal waves, they may also be applied to the field of tribology [137]. The use of (311) GaAs substrates also has interest from the point of view of fundamental physics since this GaAs is piezoactive in this direction [138] leading to the possibility of new effects

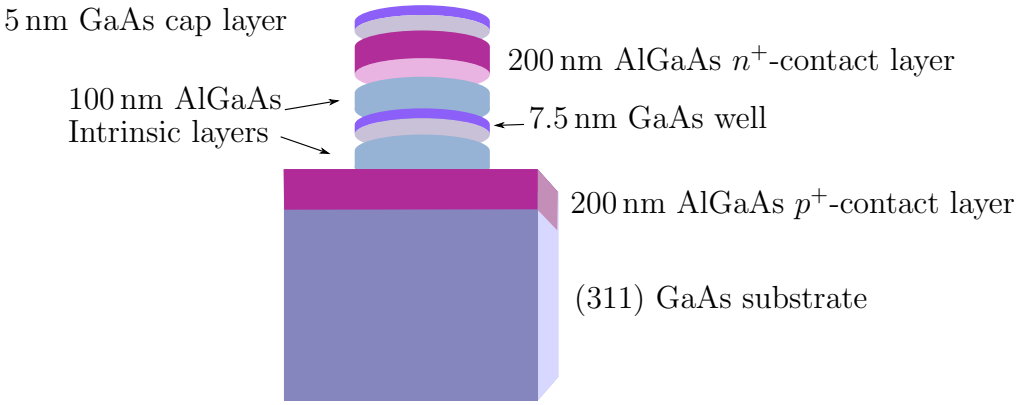

Figure 6.1: Schematic of RC34 layer structure. All AlGaAs layers feature 33% Aluminium.

due to the interactions between electrons and phonons in structures grown on these substrates.

Previous work with (311) GaAs has shown the possibility for the generation and detection of transverse modes in low symmetry directions using *pump-probe* in a superlattice where the pump and probe beam were both aligned on the superlattice device [136]. The problem with detecting and generating in the same SL is the longitudinal and transverse components of the signal are mixed, leading to difficulties in separating the different contributions. A more recent work [12] used detection on the opposite side of the substrate to the generation of the acoustic pulses. The different speeds of transverse phonons compared to acoustic phonons in GaAs substrates cause a separation of the two pulses in this configuration making the separation of the different modes easier.

The development of a *p-i-n* photodiode detector, similar to the one used in chapter 4, which could be used on (311) would enable further investigations of the generation and propagation of transverse acoustic phonons in low symmetry GaAs substrates. An initial investigation of this possibility has been undertaken. It was found that growing a *p-i-n* device which incorporates a QW with the good quality optical resonance, which is necessary for the creation of a sensitive detector of acoustic waves, is challenging on a (311) substrate.

After a series of iterations of device design and testing, in collaboration with Dr. Richard Champion from the University of Nottingham, a device was created which could detect longitudinal acoustic waves on a (311) substrate. This device is shown in figure 6.1. The p layer was grown first in this sample, as opposed to the n layer being grown first in normal samples. This was found to be necessary due to the growth requirements for doped AlGaAs on a (311) substrate. The stepped layer of the surface make it more prone to roughening. Also the nature of the exposed bonds on this surface mean that the doping must be treated differently to doping of (100) grown GaAs. In the structure shown in figure 6.1 p doping is provided by Si and the n doping is provided by Te, the doping in both cases is $10^{18}\,\mathrm{cm}^{-3}$ as is usual for contact layers. This structure was grown on the A face of the (311) substrate where it is possible for Si to act as a p dopant, rather than as the n dopant it normally forms in (100) GaAs. This was necessary because the carbon which is often used as a p dopant was not found to be effective on the (311) orientation of GaAs. The sample was processed into optical access mesas using the "Sheffield" mask shown in figure 3.2a and an Aluminium film transducer was evaporated on the back. The sample fabrication procedures where as described in section 3.2.

An example of the longitudinal acoustic signal detected in this device, after generation in an $\approx$70 nm aluminium film transducer and propagation through the 477 µm (311) substrate, is shown in figure 6.2. This signal was detected using the photocurrent *pump-probe* arrangement described in section 3.10, with the substrate maintained at 10 K through the use of the bath cryostat described in section 3.5.1. The second strain pulse which can be seen in this trace is due to the strain passing through the QW in the detector again after reflecting at the surface. The extension of this work to study the quasi-transverse signal which is predicted to be present [12] has yet to be completed, as the alignment necessary to see the transverse signal is currently unclear. It is expected that the transverse signal will not travel perpendicular to the (311) substrate due to phonon focussing. This is an effect seen in anisotropic crystals where the group velocity and wavevector of a phonon

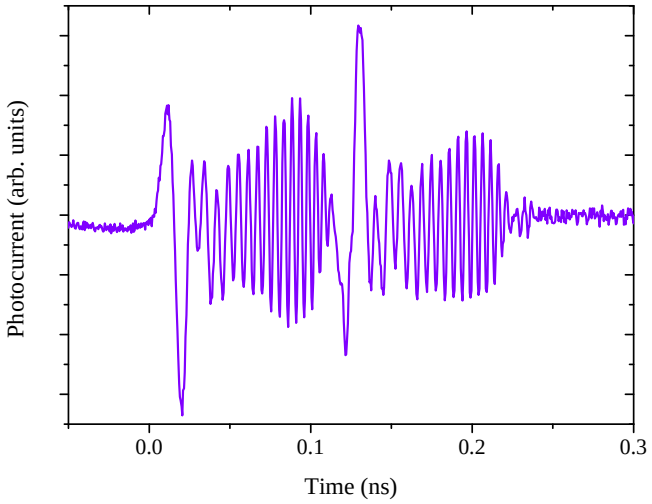

Figure 6.2: Trace showing an example of the phonon signal detected using a *p-i-n* device on a (311) substrate. The signal was detected at the time LA phonons are expected to reach the detector after being excited in an aluminium film transducer and travelling through the substrate. Laser light with a wavelength of 780 nm was used for the experiment.

wave may point in different directions meaning that the energy deposited by the phonons is decreased in some directions and increased in others [139]. It is expected that the energy of the transverse phonons will be decreased in the [311] direction. This means the laser should not be aligned directly opposite the device to obtain a clear signal. Theoretical studies of the likely phonon focussing effect in this study are currently being undertaken.

6.2.3 Further Investigation of the Electrical Response of a Weakly Coupled Semiconductor Superlattice

The results of chapter 5 were described by a theory based on a previous work developed by Tucker to describe quantum detection at mm wavelengths in a super-Schottky diode [85]. The theory used to describe the signal seen in these experiments should be extended to include a more realistic description

of the contact regions and also the effect of multiple frequencies in the exciting acoustic wave. This is likely to provide a more complete description of the experimental results. An extension of the investigation of different samples could aid in our understanding of the range of validity of the theory and the optimum sample design for this effect to be seen.

The theory predicts that, as well as the rectified DC response to the acoustic wave which was measured in chapter 5, the current in the device should also feature a dissipative response in phase with the exciting wave. This response can be described as shown in equation 6.1.

$$I_q = \sum_{n=-\infty}^{+\infty} J_n(\alpha)\left[J_{n+1}(\alpha) + J_{n-1}(\alpha)\right] I_{DC}\left(V_{DC} + \frac{n\hbar q}{e}\right) \tag{6.1}$$

In equation 6.1, the symbols are as described in section 2.2.3, these will be briefly reiterated here for clarity. Here, $J_{n\pm1}$ are bessel functions, I_{DC} is the DC current and V_{DC} is the DC voltage, α is as shown in 6.2.

$$\alpha = \frac{\epsilon D d_L}{\hbar q d_{SL}}. \tag{6.2}$$

Where in equation 6.2, D is the deformation potential, d_L is the length of the superlattice, q is the frequency of the acoustic wave, d_{SL} is the period of the SL and ϵ is the magnitude of the strain. When the AC field is small the bessel functions can be expanded in a similar way to detailed in section 2.2.3, leading to equation 6.3.

$$I_q = \frac{\epsilon D d_L}{e d_{SL}}\left[\frac{I_{DC}(V_{DC} + \hbar q/e) - I_{DC}(V_{DC} - \hbar q/e)}{2(\hbar q/e)}\right]. \tag{6.3}$$

The term in the square brackets in equation 6.3 may be reduced to the first derivative if the variation of the conductance is slow on the voltage scale of $\hbar q/e$. Suggesting that the size of the AC response of the device is linked to the first derivative of its I-V characteristic.

A potentially exciting consequence of this AC current is the possibility for

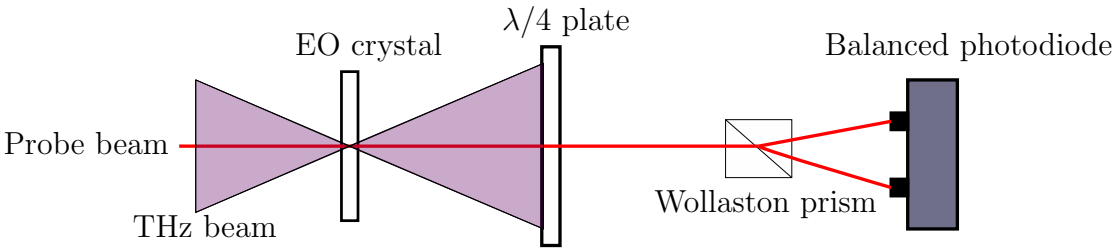

Figure 6.3: Schematic of electro-optic detection scheme

the emission of terahertz radiation from the device. A direct consequence of Maxwell's equations is that accelerating charge can produce an electromagnetic wave. This would have the advantage of being at frequencies determined by the acoustic wave frequency. The use of a SL as a terahertz source in combination with the Fabry-Pérot technique used in chapter 5 could lead to a frequency tunable source of terahertz radiation. To generate higher frequencies than were possible using the cavity technique a SL could be used as a transducer in the same way as was used in chapter 4.

A further investigation of the possibility of terahertz emission from the SL could be achieved using electro-optical sampling. Electro-optical sampling is a technique which makes use of the Pockels effect, where an electric field gives rise to birefringence in an optical material. The effect occurs in noncentrosymetric crystals and is linearly proportional to the strength of the electric field [140]. The presence of terahertz radiation can be measured using an Electro-optic crystal in the experimental arrangement shown in figure 6.3 [140].

In figure 6.3 a linearly polarised probe beam is passed through the electro-optic (EO) crystal and then the $\lambda/4$ plate. After this a Wollaston prism is used, this works as a polarising beam splitter sending light of different polarisations down different paths [141]. In the absence of terahertz radiation the probe beam will pass through the electro-optic crystal without any change of polarisation and then become circularly polarised at the $\lambda/4$ plate. The Wollaston prism will then deflect two beams of equal size, which can be measured by a balanced photodiode giving zero signal. The presence of a

terahertz field in the electro-optic crystal will induce birefringence which leads to the probe beam becoming elliptically polarised. This causes a change in intensity between the two beams deflected by the Wollaston crystal, and a signal on the balanced photodiode. To increase the magnitude of this effect the terahertz beam is focused into the EO crystal as shown in figure 6.3. For samples where it is possible to use a pump laser to excite the terahertz field the detection scheme shown in figure 6.3 can be incorporated into a *pump-probe* scheme similar to the ones described in chapter 3, allowing a coherent measurement of the terahertz radiation.

A final potential interesting avenue of research is the investigation of the origins of the acoustic response seen when the SL samples are biased at levels where they move into the region of negative differential conductivity and domain formation. Strong acoustic responses were seen in this region in both the weakly and strongly coupled SL samples. The acoustic response was also seen to change polarity in this region compared to its polarity at biases below this region. There is also a high possibility of acoustically-seeded terahertz emission due to charge oscillations at biases in this region.

Bibliography

[1] M. Maldovan. Sound and heat revolutions in phononics. *Nature*, 503(7475):209–217, 2013.

[2] M. Schubert, M. Grossmann, C. He, D. Brick, P. Scheel, O. Ristow, V. Gusev, and T. Dekorsy. Generation and detection of gigahertz acoustic oscillations in thin membranes. *Ultrasonics*, 56:109–115, 2015.

[3] H. T. Grahn, H. J. Maris, and J. Tauc. Picosecond Ultrasonics. *IEEE. Journal of quantum electronics*, 25:2562–2568, 1989.

[4] C. Mechri, P. Ruello, and V. Gusev. Confined coherent acoustic modes in a tubular nanoporous alumina film probed by picosecond acoustics methods. *New Journal of Physics*, 14(2):023048, 2012.

[5] C. Rossignol, B. Perrin, B. Bonello, P. Djemia, P. Moch, and H. Hurdequint. Elastic properties of ultrathin permalloy/alumina multilayer films using picosecond ultrasonics and Brillouin light scattering. *Physical Review B*, 70(9):094102, 2004.

[6] D. Schneider, F. Liaqat, O. El Abouti, W. Tremel, H-J. Butt, B. Djafari-Rouhani, G. Fytas, et al. Defect-controlled hypersound propagation in hybrid superlattices. *Physical Review Letters*, 111(16):164301, 2013.

[7] K-H. Lin, C-T. Yu, S-Z. Sun, H-P. Chen, C-C. Pan, J-I. Chyi, S-W. Huang, P-C. Li, and C-K. Sun. Two-dimensional nanoultrasonic imaging by using acoustic nanowaves. *Applied Physics Letters*, 89(4):–, 2006.

[8] T. Dehoux, O. B. Wright, R. L. Voti, and V. E. Gusev. Nanoscale mechanical contacts probed with ultrashort acoustic and thermal waves. *Physical Review B*, 80(23):235409, 2009.

[9] M. Hettich, K. Jacob, O. Ristow, C. He, J. Mayer, M. Schubert, V. Gusev, A. Bruchhausen, and T. Dekorsy. Imaging of a patterned and buried molecular layer by coherent acoustic phonon spectroscopy. *Applied Physics Letters*, 101(19):191606, 2012.

[10] C. Thomsen, H. T. Grahn, H. J. Maris, and J. Tauc. Surface generation and detection of phonons by picosecond light pulses. *Physical Review B*, 34:4129 – 4138, 1986.

[11] H-N. Lin, R. J. Stoner, H. J. Maris, and J. Tauc. Phonon attenuation and velocity measurements in transparent materials by picosecond acoustic interferometry. *Journal of Applied Physics*, 69(7):3816–3822, 1991.

[12] A. V. Scherbakov, M. Bombeck, J. V. Jäger, A. S. Salasyuk, T. L. Linnik, V. E. Gusev, D. R. Yakovlev, A. V. Akimov, and M. Bayer. Picosecond opto-acoustic interferometry and polarimetry in high-index GaAs. *Optics Express*, 21(14):16473–16485, 2013.

[13] T. Dehoux, M. A. Ghanem, O. F. Zouani, M. Ducousso, N. Chigarev, C. Rossignol, N. Tsapis, M-C. Durrieu, and B. Audoin. Probing single-cell mechanics with picosecond ultrasonics. *Ultrasonics*, 56:160–171, 2015.

[14] S. Che, P. R. Guduru, A. V. Nurmikko, and H. J. Maris. A scanning acoustic microscope based on picosecond ultrasonics. *Ultrasonics*, 56:153–159, 2015.

[15] O. Matsuda and O. B. Wright. Reflection and transmission of light in multilayers perturbed by picosecond strain pulse propagation. *Journal of the Optical Society of America B*, 19(12):3028–3041, 2002.

[16] W. Chen, Y. Lu, H. J. Maris, and G. Xiao. Picosecond ultrasonic study of localized phonon surface modes in Al/Ag superlattices. *Physical Review B*, 50(19):14506, 1994.

[17] P. M. Walker, J. S. Sharp, A. V. Akimov, and A. J. Kent. Coherent elastic waves in a one-dimensional polymer hypersonic crystal. *Applied Physics Letters*, 97(7):073106, 2010.

[18] A. Yamamoto, T. Mishinia, Y. Yamamoto, and M. Nakayama. Coherent oscillations of Zone-Folded modes in GaAs-AlAs superlattices. *Physical Review Letters*, 73:740–743, 1994.

[19] M. F. Pascual Winter, A. Fainstein, B. Jusserand, B. Perrin, and A. Lemaître. Optimized optical generation and detection of superlattice acoustic phonons. *Applied Physics Letters*, 94(10):103103, 2009.

[20] P. Hawker, A. J. Kent, L. J. Challis, A. Bartels, T. Dekorsy, H. Kurz, and K. Köhler. Observation of coherent zone-folded acoustic phonons generated by Raman scattering in a superlattice. *Applied Physics Letters*, 77(20):3209–3211, 2000.

[21] A. J. Kent, N. M. Stanton, L. J. Challis, and M. Henini. Generation and propagation of monochromatic acoustic phonons in gallium arsenide. *Applied Physics Letters*, 81(18):3497–3499, 2002.

[22] A. Huynh, B. Perrin, and A. Lemaître. Semiconductor superlattices: A tool for terahertz acoustics. *Ultrasonics*, 56:66–79, 2015.

[23] B. Jusserand B. Perrin A. Lemaître M. F. Pascual-Winter, A. FA. Fainstein. Spectral reponses of phonon optical generation and detection in superlattices. *Physical Review B*, 85:235443, 2012.

[24] N. D. Lanzillotti-Kimura, A. Fainstein, A. Huynh, B. Perrin, B. Jusserand, A. Miard, and A. Lemaître. Coherent generation of acoustic phonons in an optical microcavity. *Physical Review Letters*, 99(21):217405, 2007.

[25] N. D. Lanzillotti-Kimura, A. Fainstein, B. Perrin, B. Jusserand, L. Largeau, O. Mauguin, and A. Lemaître. Enhanced optical generation and detection of acoustic nanowaves in microcavities. *Physical Review B*, 83(20):201103, 2011.

[26] N. D. Lanzillotti-Kimura, A. Fainstein, B. Perrin, and B. Jusserand. Theory of coherent generation and detection of THz acoustic phonons using optical microcavities. *Physical Review.*, 84:064307, Aug 2011.

[27] D. C. Heinecke, O. Kliebisch, J. Flock, A. Bruchhausen, K. Köhler, and T. Dekorsy. Selective excitation of zone-folded phonon modes within one triplet in a semiconductor superlattice. *Physical Review B*, 87(7):075307, 2013.

[28] P. Ruello and V. E. Gusev. Physical mechanisms of coherent acoustic phonons generation by ultrafast laser action. *Ultrasonics*, 56:21–35, 2015.

[29] D. Moss, A. V. Akimov, R. P. Champion, C. T. Foxon, M. Henini, L. Eaves, A. J. Kent, and B. A. Glavin. Picosecond strain pulses probed by the photocurrent in semiconductor devices with quantum wells. *Physical Review B*, 83:245303, 2011.

[30] P. Y. Yu and M. Cardona. *Fundamentals of Semiconductors - Physics and material properties*. Springer, second edition, 1999.

[31] J. Bardeen and W. Shockley. Deformation potentials and mobilities in non-polar crystals. *Physical Review*, 80(1):72, 1950.

[32] I. Vurgaftman, J. R. Meyer, and L. R. Ram-Mohan. Band parameters for III–V compound semiconductors and their alloys. *Journal of Applied Physics*, 89(11):5815–5875, 2001.

[33] C. G. Van de Walle. Band lineups and deformation potentials in the model-solid theory. *Physical Review B*, 39:1871–1883, Jan 1989.

[34] L. Challis, editor. *Electron - Phonon Interactions in Low-Dimensional Structures*. Oxford University Press, 2003.

[35] S. I. Pekar. Electron-phonon interaction proportional to external applied field and sound amplification in semiconductors. *Journal of Experimental and Theoretical Physics*, 22:431, 1966.

[36] B. A. Glavin, V. A. Kochelap, T. L. Linnik, and K. W. Kim. Electron-phonon interaction via the Pekar mechanism in nanostructures. *Physical Review B*, 71(8):081305, 2005.

[37] P. A. Knipp and T. L. Reinecke. Coupling between electrons and acoustic phonons in semiconductor nanostructures. *Physical Review B.*, 52:5923–5928, Aug 1995.

[38] J. H. Davis. *The Physics of Low - Dimensional Semiconductors*. Cambridge University Press, 1998.

[39] Vadim Siklitsky. http://www.ioffe.ru/SVA/NSM/, 2001.

[40] V. I. Pipa, V. V. Mitin, and M. Stroscio. Substantial contribution of effective mass variation to electron-acoustic phonon interaction via deformation potential in semiconductor nanostructures. *Applied Physics Letters*, 74(11):1585–1587, 1999.

[41] A. V. Akimov, A. V. Scherbakov, D. R. Yakovlev, C. T. Foxon, and M. Bayer. Ultrafast band-gap shift induced by a strain pulse in semiconductor heterostructures. *Physical Review Letters*, 97(3):037401, 2006.

[42] E. S. K. Young, A. V. Akimov, R. P. Campion, A. J. Kent, and V. Gusev. Picosecond strain pulses generated by a supersonically expanding electron-hole plasma in GaAs. *Physical Review B*, 86(15):155207, 2012.

[43] M. Cardona. In *Modulation spectroscopy of semiconductors*, volume 11 of *Advances in Solid State Physics*. Academic Press, New York, London, 1969.

[44] J. F. Creemer, F. Fruett, G. Meijer, and P. J. French. The piezojunction effect in silicon sensors and circuits and its relation to piezoresistance. *IEEE sensors journal*, 1(2):98–108, 2001.

[45] S. M. Sze. *Semicondctor Devices Physics and Technology*. John Wiley & Sons, Inc, second edition, 2002.

[46] B. G. Streetman. *Solid State Electronic Devices*. Prentice-Hall, Inc, fourth edition, 1995.

[47] D. M. Moss, A. V. Akimov, R. P. Campion, and A. J. Kent. Ultrafast Strain-Induced Electronic Transport in a GaAs pn Junction Diode. *Chinese Journal of Physics*, 49(1):499–505, 2011.

[48] D. M. Moss, A. V. Akimov, B. A. Glavin, M. Henini, and A. J. Kent. Ultrafast strain-induced current in a GaAs Schottky diode. *Physical Review Letters*, 106(6):066602, 2011.

[49] E. S. K. Young, A. V. Akimov, M. Henini, L. Eaves, and A. J. Kent. Subterahertz Acoustical Pumping of Electronic Charge in a Resonant Tunneling Device. *Physical Review Letters*, 108(22):226601, 2012.

[50] D. Moss, A. V. Akimov, O. Makarovsky, R. P. Champion, C. T. Foxon, L. Eaves, A. J. Kent, and B. A. Glavin. Ultrafast acoustical gating of the photocurrent in a p-i-n tunneling diode incorporating a quantum well. *Physical Review B*, 80:113306, 2009.

[51] L. L. Bonilla and H. T. Grahn. Non-linear dynamics of semiconductor superlattices. *Reports on Progress in Physics*, 68(3):577, 2005.

[52] A. Wacker. Semiconductor Superlattices: A model system for nonlinear transport. *Physics Reports*, 357:1–111, 2002.

[53] J. Faist, F. Capasso, D. L. Sivco, C. Sirtori, A. L. Hutchinson, and A. Y. Cho. Quantum cascade laser. *Science*, 264(5158):553–556, 1994.

[54] K. F. Renk, B. I. Stahl, A. Rogl, T. Janzen, D. G. Pavelev, Yu. I. Koshurinov, V. Ustinov, and A. Zhukov. Subterahertz superlattice parametric oscillator. *Physical Review Letters*, 95(12):126801, 2005.

[55] M. T. Greenaway, A. G. Balanov, D. Fowler, A. J. Kent, and T. M. Fromhold. Using acoustic waves to induce high-frequency current oscillations in superlattices. *Physical Review B*, 81(23):235313, 2010.

[56] B. A. Glavin, V. A. Kochelap, and T. L. Linnik. Generation of high-frequency coherent acoustic phonons in a weakly coupled superlattice. *Applied Physics Letters*, 74:3525–3527, 1999.

[57] A. J. Kent, R. N Kini, N. M. Stanton, M. Henini, B. A. Glavin, V. A. Kochelap, and T. L. Linnik. Acoustic Phonon Emission from a Weakly Coupled Superlattice under Vertical Electron Transport: Observation of Phonon Resonance. *Physical Review Letters*, 96:215504–1 – 215504–4, 2006.

[58] R. P. Beardsley, R. P. Campion, B. A. Glavin, and A. J. Kent. A GaAs/AlAs superlattice as an electrically pumped THz acoustic phonon amplifier. *New Journal of Physics*, 13:073007, 2011.

[59] R. P. Beardsley, A. V. Akimov, M. Henini, and A. J. Kent. Coherent Terahertz Sound Amplification and Spectral Line Narrowing in a Stark Ladder Superlattice. *Physical Review Letters*, 104:085501–1 – 085501–4, 2010.

[60] W. Maryam, A. V. Akimov, R. P. Campion, and A. J. Kent. Dynamics of a vertical cavity quantum cascade phonon laser structure. *Nature Communications*, 4, 2013.

[61] L. Esaki and R. Tsu. Superlattice and negative diferential conductivity in semiconductors. *IBM J. Res. Develop*, 14:61–65, 1970.

[62] R. Tsu and G. Döhler. Hopping conduction in a "superlattice". *Physical Review B*, 12:680–686, 1975.

[63] H. T. Grahn, editor. *Semiconductor Superlattices: Growth and Electronic properties*. World Scientific, 1995.

[64] C. Kittel. *Introduction to Solid State Physics*. John Wiley & Sons, 6th edition, 1986.

[65] G. Bastard. Wave mechanics applied to semiconductors. *Les editions de Physique (CNRS, Paris, 1988)*, 1988.

[66] E. E. Mendez and G. Bastard. Wannier-Stark Ladders and Bloch Oscillations in Superlattices. *Physics Today*, 34:34–41, 1993.

[67] R. Tsu and L. Esaki. Stark quantisation in superlattices. *Physical Review B*, 43:5204–5206, 1991.

[68] R. Tsu and L. Esaki. Erratum: Stark quantization in superlattices [Phys. Rev. B 43, 5204 (1991)]. *Physical Review B*, 44:3495, 1991.

[69] E. Schöll, editor. *Theory of Transport properties of Semiconductor Nanostructures*. Chapman and Hall, 1998.

[70] G. H. Wannier. Wavefunction and effective Hamiltonian for Bloch electrons in an electric field. *Physical Review*, 117:432–439, 1960.

[71] J. Kastrup, R. Klann, H. T. Grahn, K. Ploog, L. L. Bonilla, J. Galan, M. Kindelan, M. Moscoso, and R. Merlin. Self-oscillations of domains in doped GaAs-AlAs superlattices. *Physical Review B*, 19:13761 – 1374, 1995.

[72] L. Esaki and L. L. Chang. New Transport Phenomenon in a Semiconductor "Superlattice". *Physical Review Letters*, 33:495–498, 1974.

[73] J. Kastrup, R. Hey, K. H. Ploog, H. T. Grahn, L. L. Bonilla, M. Kindelan, M. Moscoso, A. Wacker, and J. Galán. Electrically tunable GHz oscillations in doped GaAs-AlAs superlattices. *Physical Review B*, 55:2476–2488, Jan 1997.

[74] G. Platero and R. Aguado. Photon-assisted transport in semiconductor nanostructures. *Physics Reports*, 395(1):1–157, 2004.

[75] D. Sánchez, M. Moscoso, L. L. Bonilla, G. Platero, and R. Aguado. Current self-oscillations, spikes, and crossover between charge monopole and dipole waves in semiconductor superlattices. *Physical Review B*, 60:4489–4492, Aug 1999.

[76] J. Batey and S. L. Wright. Energy band alignment in GaAs:(Al, Ga) As heterostructures: The dependence on alloy composition. *Journal of Applied Physics*, 59(1):200–209, 1986.

[77] M. B. Zivanov and L. D. Zivanov. Determination of electron mobility in heavily doped n-type GaAs using kp-model. In *Microelectronics, 1995. Proceedings., 1995 20th International Conference on*, volume 1, pages 95–100. IEEE, 1995.

[78] S. Tamura, D. C. Hurley, and J. P. Wolfe. Acoustc Phonon propagation in superlattices. *Physical Review B*, 38:1427–1449, 1988.

[79] S. M. Rytov. Acoustical Properties of a thinly laminated medium. *Soviet Physics Acoustic*, 2:68–80, 1956.

[80] M. Trigo, A. Fainstein, B. Jusserand, and V. Thierry-Mieg. Finite-size effects on acoustic phonons in GaAs/AlAs superlattices. *Physical Review B*, 66:125311–1 –125311–7, 2002.

[81] M. W. C. Dharma-wardana, P. X. Zhang, and D. J. Lockwood. Finite-size effects on superlattice acoustic phonons. *Physical Review B*, 48:11960 – 11964, 1993.

[82] A. Bartels, T. Dekorsy, and H. Kurz. Coherent Zone-Folded Longitudinal Acoustic Phonons in Semiconductor Superlattices: Excitation and Detection. *Physical Review Letters*, 82:1044–1047, 1999.

[83] O. B. Wright, B. Perrin, O. Matsuda, and V. E. Gusev. Ultrafast carrier diffusion in gallium arsenide probed with picosecond acoustic pulses. *Physical Review B*, 64:081202, Aug 2001.

[84] A. Huynh, B. Perrin, N. D. Lanzillotti-Kimura, B. Jusserand, and A. Lemaître Fainstein, A. and. Subterahertz monochromatic acoustic wave propagation using semiconductor superlattices as transducers. *Physical Review B*, 78:233302, Dec 2008.

[85] J. R. Tucker. Quantum limited detection in tunnel junction mixers. *Quantum Electronics, IEEE Journal of*, 15(11):1234–1258, 1979.

[86] J. R Tucker and M. J Feldman. Quantum detection at millimeter wavelengths. *Reviews of Modern Physics*, 57(4):1055, 1985.

[87] P. K. Tien and J. P. Gordon. Multiphoton process observed in the interaction of microwave fields with the tunneling between superconductor films. *Physical Review*, 129(2):647, 1963.

[88] B. J. Keay, S. Zeuner, S. J. Allen Jr, K. D. Maranowski, A. C. Gossard, U. Bhattacharya, and M. J. W. Rodwell. Dynamic localization, absolute negative conductance, and stimulated, multiphoton emission in sequential resonant tunneling semiconductor superlattices. *Physical Review Letters*, 75(22):4102, 1995.

[89] A. Wacker and A.-P. Jauho. Transport in a Weakly-Coupled Superlattice: A Quantitative Approach for Photon-Assisted Tunneling. *Physica Status Solidi (b)*, 204(1):73–76, 1997.

[90] B. A. Glavin, V. A. Kochelap, T. L. Linnik, K. W. Kim, and M. A. Stroscio. Generation of high-frequency coherent acoustic phonos in superlattices under hopping transport. I. Linear theory of phonon instability. *Physical Review B*, 65:085303–1 – 085303–11, 2002.

[91] B. A. Glavin, V. A. Kochelap, T. L. Linnik, K. W. Kim, and M. A. Stroscio. Generation of high-frequency coherent acoustic phonos in superlattices under hopping transport. II. Steady-state phonon population and electric current in generation regime. *Physical Review B*, 65:085304 – 085304, 2002.

[92] G. Tas and H. J. Maris. Electron diffusion in metals studied by picosecond ultrasonics. *Physical Review B*, 49:15046–15054, Jun 1994.

[93] T. Saito, O. Matsuda, and O. B. Wright. Picosecond acoustic phonon pulse generation in nickel and chromium. *Physical Review B*, 67:205421, May 2003.

[94] W. M. Haynes. *CRC Handbook of Chemistry and Physics*. Taylor & Francis, 94^{th} edition, 2013.

[95] G. W. C. Kaye and T. H. Laby. *Tables of physical and chemical constants*. Longmane, 1995.

[96] A. D. Raki. Algorithm for the determination of intrinsic optical constants of metal films: application to aluminum. *Applied Optics*, 34:4755–4767, 1995.

[97] G. Tas, J. J. Loomis, H. J. Maris, A. A. Bailes, and L. E. Seiberling. Picosecond ultrasonics study of the modification of interfacial bonding by ion implantation. *Applied Physics Letters*, 72(18):2235–2237, 1998.

[98] L. McGhee, S. G. McMeekin, I. Nicol, M. I. Robertson, and J. M. Winfield. Chemomechanical polishing of gallium arsenide and cadmium telluride to subnanometre surface finish. Evaluation of the action and effectiveness of hydrogen peroxide, sodium hypochlorite and dibromine as reagents. *Journal of Materials Chemistry*, 4(1):29–34, 1994.

[99] A. G. Baca and C. I. H. Ashby, editors. *Fabrication of GaAs Devices*. Institution of electrical engineers, London, 2005.

[100] J. Angilello, R. M. Potemski, and G. R. Woolhouse. Etch pits and dislocations in {100} GaAs wafers. *Journal of Applied Physics*, 46(5):2315–2316, 1975.

[101] S. M. Sze. *Physics of Semiconductor Devices*. John Wiley & Sons, Inc., 2nd edition, 1981.

[102] Wan Maryam Wan Ahmad Kamil. *The study of THz vertical cavity SASER Devices*. PhD thesis, University of Nottingham, 2013.

[103] J. Hawkes and I. Latimer. *Lasers Theory and Practise*. Prentice Hall Europe, 1995.

[104] J. D. Choi, T. Feurer, M. Yamaguchi, B. Paxton, and K. A. Nelson. Generation of ultrahigh-frequency tunable acoustic waves. *Applied Physics Letters*, 87(8):081907, 2005.

[105] J-C. Diels and W. Rudolph. *Ultrashort laser pulse phenomena*. Academic press, 2006.

[106] E. Riis M. Wilkinson G.L Oppo, S. M. Barnett, editor. *Quantum Dynamics of Simple Systems*. Institutie of Physics publishing, 1997.

[107] N. D. Lanzillotti-Kimura, A. Fainstein, A. Lemaître, B. Jusserand, and B. Perrin. Coherent control of sub-terahertz confined acoustic nanowaves: Theory and experiments. *Physical Review B*, 84(11):115453, 2011.

[108] N. Li, J. Ren, L. Wang, G. Zhang, P. Hänggi, and B. Li. Colloquium: Phononics: Manipulating heat flow with electronic analogs and beyond. *Reviews of Modern Physics*, 84(3):1045, 2012.

[109] A. Gadalla, T. Dehoux, and B. Audoin. Transverse mechanical properties of cell walls of single living plant cells probed by laser-generated acoustic waves. *Planta*, 239(5):1129–1137, 2014.

[110] T. Dehoux and B. Audoin. Non-invasive optoacoustic probing of the density and stiffness of single biological cells. *Journal of Applied Physics*, 112(12):124702, 2012.

[111] L. V. Wang and S. Hu. Photoacoustic tomography: in vivo imaging from organelles to organs. *Science*, 335(6075):1458–1462, 2012.

[112] S. Schmitt-Rink, D. S. Chemla, and D. A. B. Miller. Linear and nonlinear optical Properties of Semicondctor quantum wells. *Advances in Physics*, 38:89–188, 1989.

[113] G. L. Oppo, E. Riis, M. Wilkinson, and S. M. Barnett, editors. *Quantum Dynamics of Simple Systems: Proceedings of the Forty Fourth Scottish Universities Summer School in Physics, Stirling, August 1994*. Taylor & Francis, 1997.

[114] H. Le Person, C. Minot, L. Boni, J. F. Palmier, and F. Mollot. Gunn oscillations up to 20 GHz optically induced in GaAs/AlAs superlattice. *Applied Physics Letters*, 60(19):2397–2399, 1992.

[115] W. Chen, H. J. Maris, Z. R. Wasilewski, and S-I Tamura. Attenuation and velocity of 56 GHz longitudinal phonons in gallium arsenide from 50 to 300 K. *Philosophical Magazine B*, 70(3):687–698, 1994.

[116] R. I. Cottam and G. A. Saunders. The elastic constants of GaAs from 2 K to 320 K. *Journal of Physics C: Solid State Physics*, 6(13):2105, 1973.

[117] S. Adachi. *Handbook on physical properties of semiconductors*, volume 1. Springer, 2004.

[118] F. Hofmann, J. Garg, A. A. Maznev, A. Jandl, M. Bulsara, E. A. Fitzgerald, G. Chen, and K. A. Nelson. Intrinsic to extrinsic phonon lifetime transition in a GaAs–AlAs superlattice. *Journal of Physics: Condensed Matter*, 25(29):295401, 2013.

[119] T-M Liu, S-Z Sun, C-F. Chang, C-C Pan, G-T Chen, J-I Chyi, V. Gusev, and C-K Sun. Anharmonic decay of subterahertz coherent acoustic phonons in GaN. *Applied Physics Letters*, 90(4):041902–041902, 2007.

[120] B. C. Daly, K. Kang, Y. Wang, and D. G. Cahill. Picosecond ultrasonic measurements of attenuation of longitudinal acoustic phonons in silicon. *Physical Review B*, 80(17):174112, 2009.

[121] A. A. Maznev, F. Hofmann, A. Jandl, K. Esfarjani, M. T. Bulsara, E. A. Fitzgerald, G. Chen, and K. A. Nelson. Lifetime of sub-THz coherent acoustic phonons in a GaAs-AlAs superlattice. *Applied Physics Letters*, 102(4):041901, 2013.

[122] L. Landau and G. Rumer. Absorption of sound in solids. *Phys. Z. Sowjetunion*, 11(18), 1937.

[123] A. Akhieser. On the absorption of sound in solids. *J. Phys.(USSR)*, 1:277–287, 1939.

[124] W. P. Mason and R. N. Thurston, editors. *Physical Acoustics*, volume 8. Academic Press, 1971.

[125] S-I Tamura. Spontaneous decay rates of LA phonons in quasi-isotropic solids. *Physical Review B*, 31(4):2574, 1985.

[126] C. Herring. Role of low-energy phonons in thermal conduction. *Physical Review*, 95(4):954, 1954.

[127] S. Simons. The absorption of very high frequency sound in dielectric solids. In *Mathematical Proceedings of the Cambridge Philosophical Society*, volume 53, pages 702–716. Cambridge Univ Press, 1957.

[128] Gregory Snider. 1D Poisson, http://www3.nd.edu/ gsnider/. *University of Notre Dame*.

[129] D. R. Fowler, A. V. Akimov, A. G. Balanov, M. T. Greenaway, M. Henini, T. M Fromhold, and A. J. Kent. Semiconductor charge transport driven by a picosecond strain pulse. *Applied Physics Letters*, 92(23):232104, 2008.

[130] E. Péronne and B. Perrin. Generation and detection of acoustic solitons in crystalline slabs by laser ultrasonics. *Ultrasonics*, 44:e1203–e1207, 2006.

[131] H-Y Hao and H. J. Maris. Experiments with acoustic solitons in crystalline solids. *Physical Review B*, 64(6):064302, 2001.

[132] A. V. Scherbakov, P. J. S. Van Capel, A. V. Akimov, J. I. Dijkhuis, D. R. Yakovlev, T. Berstermann, and M. Bayer. Chirping of an optical transition by an ultrafast acoustic soliton train in a semiconductor quantum well. *Physical Review Letters*, 99(5):057402, 2007.

[133] W. F. Chow. *Principles of tunnel diode circuits*. Wiley, New York, London, 1964.

[134] B. M. Clemens and G. L. Eesley. Relationship between Interfacial Strain and the Elastic Response of Multilayer Metal Films. *Physical Review Letters*, 61:2356–2359, Nov 1988.

[135] D. R. Fowler. *Non-linear electron dynamics in semiconductor superlattices and dilute nitride alloys*. PhD thesis, University of Nottingham, 2005.

[136] P. Walker, R. P. Campion, A. J. Kent, D. Lehmann, and Cz. Jasiukiewicz. Excitation and detection of high-frequency coherent acoustic phonons in low-symmetry superlattices. *Physical Review B*, 78(23):233307, 2008.

[137] T. Pezeril, P. Ruello, S. Gougeon, N. Chigarev, D. Mounier, J-M. Breteau, P. Picart, and V. Gusev. Generation and detection of plane coherent shear picosecond acoustic pulses by lasers: Experiment and theory. *Physical Review B*, 75(17):174307, 2007.

[138] G. Rozas, M. F. Pascual Winter, A. Fainstein, B. Jusserand, P. O. Vaccaro, S. Saravanan, and N. Saito. Piezoelectric semiconductor acoustic cavities. *Physical Review B*, 72(3):035331, 2005.

[139] B. Taylor, H. J. Maris, and C. Elbaum. Phonon focusing in solids. *Physical Review Letters*, 23(8):416, 1969.

[140] Mira Naftaly. *Terahertz Metrology*. Artech House, Boston, London, 2015.

[141] E. Hecht. *Optics*. Addison-Wesley, second edition, 1974.